# Experimental evaluation of a low temperature and low pressure turbine

by
Brian Ssebabi

*Thesis presented for the degree of Master of Engineering in the Faculty of Engineering at Stellenbosch University*

Supervisor: Mr Robert Thomas Dobson
Co-supervisor: Prof Adoniya Ben Sebitosi

April 2014

# Declaration

By submitting this thesis electronically, I declare that the entirety of the work contained therein is my own, original work, that I am the sole author thereof (save to the extent explicitly otherwise stated), that reproduction and publication thereof by Stellenbosch University will not infringe any third party rights and that I have not previously in its entirety or in part submitted it for obtaining any qualification.

Date: .....

# Abstract


## Experimental evaluation of a low temperature and low pressure turbine

B. Ssebabi

*Department of Mechanical and Mechatronic Engineering,*
*University of Stellenbosch,*
*Private Bag X1, Matieland 7602, South Africa.*

Thesis: MEng (Mech)

April 2014

The potential benefits from saving energy have driven most industrial processing facilities to pay more attention to reducing energy wastage. Because the industrial sector is the largest user of electricity in South Africa (37.7% of the generated electricity capacity), the application of waste heat recovery and utilisation (WHR&U) systems in this sector could lead to significant energy savings, a reduction in production costs and an increase in the efficiency of industrial processes. Turbines are critical components of WHR&U systems, and the choice of an efficient and low cost turbine is crucial for their successful implementation. The aim of this thesis project is therefore to validate the use of a turbine for application in a low grade energy WHR&U system. An experimental turbine kit (Infinity Turbine ITmini) was acquired, assembled and tested in a specially designed and built air test bench. The test data was used to characterise the turbine for low temperature (less than 120 Celsius) and pressure (less than 10 bar) conditions. A radial inflow turbine rotor was designed, manufactured and then tested with the same test bench, and its performance characteristics determined. In comparison with the ITmini rotor, the as-designed and manufactured rotor achieved a marginally better performance for the same test pressure ratio range. The as-designed turbine rotor performance characteristics for air were then used to scale the turbine for a refrigerant-123 application. Future work should entail integrating the turbine with a WHR&U system, and experimentally determining the system's performance characteristics.


Key words: radial inflow turbine, low grade energy waste heat recovery and utilisation systems, turbine performance characterisation and prediction

# Uittreksel

## Eksperimentele evaluasie van 'n lae temperatuur en -druk turbine

*(" Experimental evaluation of a low temperature and low pressure turbine")*

B. Ssebabi

*Departement Meganiese en Megatroniese Ingenieurswese,*
*Universiteit van Stellenbosch,*
*Privaatsak X1, Matieland 7602, Suid Afrika.*

Tesis: MIng (Meg)

April 2014

Die potensiële voordele wat gepaard gaan met energiebesparing het die fokus van industrie laat val op die bekamping van energievermorsing. Die industriële sektor is die grootse verbruiker van elektrisiteit in Suid-Afrika (37.7% van die totale gegenereerde kapasiteit). Energiebesparing in die sektor deur die toepassing van afval-energie-herwinning en benutting (AEH&B) sisteme kan lei tot drastiese vermindering van energievermorsing, 'n afname in produksie koste en 'n toename in die doeltreffendheid van industriële prosesse. Turbines is kritiese komponente in AEH&B sisteme en die keuse van 'n doeltreffende lae koste turbine is noodsaaklik in die suksesvolle implementering van dié sisteme. Die doelwit van hierdie tesisprojek is dus om die toepassing van 'n turbine in 'n lae graad energie AEH&B sisteem op die proef te stel. 'n Eksperimentele turbine stel ("Infinity Turbine ITmini") is aangeskaf, aanmekaargesit en getoets op 'n pasgemaakte lugtoetsbank. Die toetsdata is gebruik om die turbine te karakteriseer by lae temperatuur (minder as 120 Celsius) en druk (minder as 10 bar) kondisies. 'n Radiaalinvloeiturbinerotor is ook ontwerp, vervaardig en getoets op die lugtoetsbank om die rotor se karakteristieke te bepaal. In vergelyking met die ITmini-rotor het die radiaalinvloeiturbinerotor effens beter werkverrigting gelewer by diselfde toetsdruk verhoudings. Die werksverrigtingkarakteristieke met lug as vloeimedium van die radiaalinvloeiturbinerotor is gebruik om die rotor te skaleer vir 'n R123 verkoelmiddel toepassing. Toekomstige werk sluit in om die turbine met 'n AEH&B sisteem te integreer en die sisteem se werksverrigtingkarakteristieke te bepaal.

Sleutel woorde: radiaalinvloeiturbine, afval-energie-herwinning en benutting (AEH&B) sisteme, turbine prestasie karakterisering en voorspelling

# Acknowledgements

First and foremost, I would like to thank the Almighty God, whose Grace has seen me through this journey. Then, I would like to thank my supervisor, Mr. R.T. Dobson, for taking a chance on me, and allowing me work with him. It has been a fulfilling and enriching experience, and I am forever grateful. In the same breath, I would like to thank my co-supervisor, Prof. AB Sebitosi, for his technical guidance throughout this project. I also acknowledge, Dr S.J. van der Spuy, for his helpful advice on turbomachinery aspects, Prof. T.W. von Backström, for providing the excellent text on turbine scaling, my colleague Robert Craig, for introducing me to the world of latex and Autodesk, Mr. P. Trinchero, for his very helpful advice on the turbine rotor CAD drawings and lastly, the Department of Mechanical Engineering workshop staff, especially Mr. Cobus Zietzman and Mr. Ferdi Zietzman, for manufacturing my experimental apparatus.

# Dedications

*To my uncle David and my late aunt Flo ...am forever grateful!*

# Contents

# List of Figures

# List of Tables

# Nomenclature

| | |
|---|---|
| $A$ | Area, $m^2$, number of parallel paths |
| $b$ | Rotor blade tip height, m |
| $c_p$ | Specific heat at constant pressure, J/kg·K |
| $c_v$ | Specific heat at constant volume, J/kg·K |
| $C$ | Speed of sound, m/s |
| $d$ | Diameter, m |
| $E$ | Energy, J, internal induced voltage, V |
| $g$ | Standard acceleration of gravity, $m/s^2$ |
| $h$ | Enthalpy, J/kg, hub control point |
| $I$ | Current, A |
| $k$ | Loss coefficient |
| $l$ | Torque arm length, m |
| $L$ | Axial length, m |
| $m$ | Meridional direction, mass, kg |
| $\dot{m}$ | Mass flow rate, kg/s |
| $M_u$ | Non-dimensional rotor blade tip speed |
| $N$ | Rotation speed, rpm |
| $p$ | Vector location of a point on a Bezier curve |
| $P$ | Pressure, Pa or bar, number of magnetic poles, bezier function control point, power, W |
| $P_R$ | Pressure ratio |
| $\dot{Q}$ | Thermal energy transfer rate, W |
| $r$ | Radius, m, radial coordinate, m |
| $R$ | Gas constant, J/kg, Resistance, Ω |
| $s$ | Specific entropy, J/kg·K, shroud control point |
| $S_w$ | Power ratio |
| $t$ | Time, s, blade thickness, m, clearance gap, m, tangential direction |
| $T$ | Temperature, °C or K, torque, N·m |
| $u$ | Specific internal energy, J/kg |

| | |
|---|---|
| $u_m$ | Non-dimensionalised meridional length |
| $U$ | Rotor blade velocity, m/s |
| $V$ | Absolute flow velocity, m/s, voltage, V |
| $V_0$ | Spouting velocity, m/s |
| $\dot{V}$ | Volumetric flow rate, $m^3/s$ |
| $W$ | Relative velocity, m/s |
| $\dot{W}$ | Mechanical work transfer rate, W |
| $x$ | Vertical displacement |
| $z$ | Height, m, z-coordinate, m, |
| $Z$ | Number of armature conductors |
| $Z_B$ | Number of rotor blades |

**Greek letters**

| | |
|---|---|
| $\alpha$ | Absolute flow angle, ° |
| $\beta$ | Relative flow/blade angle, ° |
| $\gamma$ | Specific heat ratio |
| $\eta$ | Efficiency, % |
| $\theta$ | Non-dimensional mass flow rate |
| $\lambda$ | Incidence factor |
| $\mu$ | Dynamic viscosity, kg/m·s |
| $\rho$ | Density, $kg/m^3$ |
| $\phi$ | Magnetic flux per pole, Wb |
| $\omega$ | Angular rotation speed, rad/s |

**Subscripts**

| | |
|---|---|
| 0 | Stagnation condition, quantity at the origin |
| 1 | Turbine inlet |
| 2 | Turbine rotor inlet, turbine rotor blade tip |
| 3 | Turbine outlet/exit |
| $a$ | Armature |
| $abs$ | Absolute |
| $air$ | Air |
| $atm$ | Atmospheric |
| $A$ | Working fluid |
| $B$ | Working fluid, Bezier |
| $calc$ | Calculated |
| $corr$ | Corrected |

| | |
|---|---|
| $elec$ | Electric |
| $g$ | Gauge, generator |
| $h$ | Hub |
| $i$ | Any positive integer, iterated |
| $in$ | Inlet |
| $meas$ | Measured |
| $n$ | Normal component, any positive integer value |
| $N$ | Nozzle |
| $out$ | Outlet/exit |
| $pred$ | Predicted |
| $ref$ | Reference |
| $R123$ | Refrigerant-123 |
| $s$ | Shroud, isentropic |
| $ss$ | Stage isentropic |
| $stand.conds$ | Standard conditions |
| $t$ | Tangential component, terminal |
| $t-s$ | Total to static |
| $x$ | Cross-sectional |

**Abbreviations**

| | |
|---|---|
| BSP | British standard pipe |
| CAD | Computer aided design |
| CBORE | Counter bore |
| CE | Conformité Européenne (conformity marking within the European Economic Area) |
| CNC | Computer numerical control |
| DC | Direct current |
| FS | Full scale |
| ID | Inner diameter |
| LCD | Liquid-crystal display |
| LE | Leading edge |
| NPT | National pipe thread |
| OD | Outer diameter |
| TE | Trailing edge |
| USA | United States of America |
| WHR&U | Waste heat recovery and utilisation |

# Chapter 1

# Introduction

## 1.1 Introduction

As global demand for energy increases, supplies of fossil fuel energy resources continue to diminish. This tentatively puts the world at a potential risk of untenable energy resource prices in the future. It is clear that there is need to switch to more efficient ways of utilization of the available fossil fuel energy resources and an immediate exploitation of the available renewable/alternative energy resources.

The positive impact that energy efficiency could have on the growing energy demands of South Africa has already been considered. A scenario modelling in the Revised Balance Scenario (RBS) of the IRP 2010 (2011) showed that an increase in Energy Efficiency and Demand Side Management (EEDSM) led to a decrease in the need for additional electricity generating capacity and a subsequent decrease in carbon emissions (IRP 2010, 2011).

With the industrial sector being the largest end user of electricity in South Africa (accounts for 37.7% or just over a third of the country's generated electricity capacity, according to the Electricity Pricing Policy (EPP) of the South African Electricity Supply Industry (2008)), improvement in energy efficiency in this sector could lead to significant energy savings and reduce the pressure on the electricity supply industry. In the equally energy intensive industrial sector of the United States of America (accounts for a third of the country's energy consumption), approximately 20 to 50% of the energy consumed is ultimately released as waste heat, with 60% of it at temperatures below 230 °C and considered low grade. Many industrial facilities attempt to reduce these losses by improving the efficiency of their equipment and/or installing waste heat recovery technologies, with the brief of the latter being to capture and reuse the waste heat in the industrial processes for purposes like heating and generating of mechanical or electrical work (Waste Heat Recovery: Technology and Opportunities in U.S. Industry, 2008).

Waste heat provides an attractive opportunity for emission-free and less

costly energy resources, but even with the potential energy savings and environmental benefits resulting from it, industrial facilities will only invest in a waste heat recovery system, if it results in savings that result in a reasonable payback period (Waste Heat Recovery: Technology and Opportunities in U.S. Industry, 2008). Therefore, minimizing the cost of waste heat recovery technologies is essential, and for electricity generating waste heat recovery technologies, the choice of an efficient and low cost expander is a must.

## 1.2 Thesis objective

The aim of this project was to validate the use of a turbine for application in a low grade waste heat recovery and utilisation system. This entailed characterising the turbine for low temperature (less than 120 °C) and low pressure (less than 10 bar) conditions, using air as the working fluid, and then using the determined turbine performance characteristics to scale the turbine for refrigerant-123 applications, thus predicting its performance for integration into an organic Rankine cycle waste heat recovery and utilisation system.

## 1.3 Thesis layout

Chapter 2 briefly discusses energy saving/efficiency in the South African context and introduces the dual function absorption cycle and the organic Rankine cycle as appropriate low grade waste heat recovery technologies. The mode of operation of these two technologies is discussed, and examples of their application in available literature are also given. In addition, the expanders applicable to the two low grade waste heat technologies are discussed, including examples of their application in available literature. The mode of operation of the expanders is also described, in turn. As the expander chosen for this project, the theory on the performance analysis of a radial inflow turbine is also given.

The project experimental and design work is discussed in Chapter 3. Details of the air test bench set-up, including the different instrumentation used in the set-up are given. The experimental and safety procedures are also discussed, in addition to the analysis of the measurement uncertainty associated with the measured turbine test data. As part of the project design work, a radial inflow turbine rotor was designed and manufactured. The rotor design procedure, design code description and flow chart, formation of the CAD 3-dimensional model and material selection for the manufacture of the designed rotor are all discussed in this chapter.

Chapter 4 includes the turbine performance maps, which were plotted from the turbine performance characteristics, which were in turn calculated from the measured turbine test data. In addition, the estimation of the measurement uncertainty bounds for the calculated turbine performance characteristics and

the scaling of the turbine for refrigerant-123 application is added in this chapter. The discussion, conclusion and recommendations for future work are given in Chapter 5.

The calibration procedures for the Festo pressure sensors, T-type thermocouples and spring loaded scale are described in Appendix A, while the tabulated experimental raw data and calculated turbine performance characteristics, as well as a sample calculation of the turbine performance characteristics for one turbine test point are added in Appendix B. The rotor design code is added in Appendix C, while CAD drawings of the designed radial inflow rotor and the assembly plans of the acquired ITmini experimental turbine kit are added in Appendix D.

# Chapter 2

# Literature Survey and Theory

A healthy growth period for the South African economy has led to a consistent rise in the national energy demand. This has placed considerable pressure on country's electricity supply industry, as reflected in the sharp fall to 8% of the generated capacity reserve margin (Electricity Pricing Policy (EPP) of the South African Electricity Supply Industry, 2008). To mitigate this, it was planned that new generation capacity be added to the the system in order to restore the reserve margin and also meet new demand. But, with the current planned increase in generation capacity not expected to meet the country's demand requirements cost effectively and within the required time frame, Eskom, the country's main electricity supplier, has embarked on a comprehensive strategy to address demand, using both supply and demand solutions. This has led to the implementation of comprehensive energy efficiency and demand side management programs, including, *inter alia*, encouragement of solar water heating, mass roll-out of compact fluorescent lamps to replace the energy inefficient incandescent lamps and a push for industrial process optimisation, with an added incentive of a standard offer to pay for measured and verified energy savings at a predetermined rate. All this was aimed at reducing Eskom's peak demand supply requirement by approximately 3 GW by March, 2013 and a further 5 GW by March, 2026 (Energy Efficiency and Demand Side Management Program Evaluation, 2011).

The current installed generating capacity of South Africa is approximately 40 GW, and the largest consumer of this generated capacity is the industrial sector, which consumes 37.7% of the generated capacity. For Eskom to meet the required peak demand supply reduction, there has to be a concerted effort to improve energy efficiency in the industrial sector. Efforts to improve energy efficiency in industrial facilities normally focus on reducing the energy consumption of the manufacturing equipment, but an alternative approach to improve overall energy efficiency is to capture and reuse the released industrial waste heat, which is an inherent feature to all industrial manufacturing processes. Implementation of waste heat recovery technologies improves energy efficiency of industrial processes by as much as 50% (Waste Heat Recovery:

Technology and Opportunities in U.S. Industry, 2008). The choice of a heat recovery method depends on key factors such as temperature, phase and chemical composition of the exhaust stream, as well as the nature of the desired end use for the recovered heat. With about 60% of the industrial waste heat at temperatures below 230 °C, and considered low grade, two appropriate low grade waste heat recovery technologies have been identified from available literature; a dual function absorption cycle and an organic Rankine cycle. These two technologies are described, in turn, as follows.

## 2.1 Dual function absorption cycle

An absorption cycle is a heat-activated thermal cycle that exchanges thermal energy with its surroundings. This cycle has traditionally been used in applications where exchanges of heat with the surroundings are desired, such as, refrigeration and air conditioning (American Society of Heating, Refrigeration and Air-conditioning Engineers, Inc., 2009). In the USA, petroleum refineries are some of the largest sources of useful waste heat – consume 32 trillion Btu/year to provide process heat and electricity but with approximately 7 trillion Btu/year released in the 130 to 500 °C temperature range which is upgradable to a useful product. This released waste heat is widely utilised for waste heat-powered refrigeration, normally applied in petroleum refineries for purposes of recovering volatile products from waste process streams, debottlenecking process units and separation efficiency improvement (Erickson *et al.*, 1998). However, the low grade waste heat released from the petroleum refining processes is in excess of that required to meet refinery refrigeration needs, which meant that the power generation option had to be considered as an alternative end use for the recovered waste heat (Erickson *et al.*, 2004).

An absorption cycle that integrates generating power or refrigeration, as influenced by the demands of the surroundings, but with the possibility of providing both concurrently is referred to as a dual function absorption cycle (DFAC). Goswami and Xu (1999) proposed a dual function absorption cycle that uses an ammonia/water mixture as the working fluid, with a primary goal of generating power, while Jeggels and Dobson (2011), because of concern about the complications and hazards associated with the use of ammonia, proposed a dual function absorption cycle that uses a mixture of water/lithium-bromide as the working fluid, with a primary goal of providing refrigeration, but with a future option of integrating a low temperature turbine for power generation. Senda (2012) identified the dual function absorption cycle as an appropriate waste heat recovery technology for low grade waste heat at temperatures between 60 to 100 °C, and for his master's thesis, he designed and built a waste heat recovery and utilisation system that simulated an ammonia/water dual function absorption cycle waste heat recovery and utilisation system. This waste heat recovery system was to recover and utilise low grade

waste heat from a used fuel tank of a pebble bed modular reactor (PBMR).

The working fluid of a dual function absorption cycle is a mixture or solution of two substances; a refrigerant and an absorbent, with the function of the latter being to absorb the former and allow it to be boiled off at a lower temperature than it would be possible if it were a pure substance. According to Srikhirin *et al.* (2001), ammonia/water and water/lithium-bromide are the commonest refrigerant/absorbent combinations and the performance of an absorption system is critically dependent on the chemical and thermodynamic properties of the refrigerant/absorbent pairs. Some of the desired properties include a degree of miscibility in liquid phase within the operating temperature range of the cycle, chemical stability, non-toxicity, a large difference in boiling point between the pure refrigerant and the mixture at the same pressure and the refrigerant should have a high latent heat so as to minimise its circulation rate and that of the absorbent between the generator and the absorber. In addition, the mixture should be non-corrosive, non-explosive, environmental friendly, low cost and its transport properties, like viscosity, thermal conductivity and diffusion coefficient should favour heat and mass transfer.

According to Jeggels and Dobson (2011), the ammonia/water and water lithium-bromide cycles can be represented with very similar schematic diagrams, though their actual physical characteristics differ vastly – an ammonia/water system operates at pressures well above atmospheric thus requiring large pressure vessels and the use of ammonia as the refrigerant allows very low temperature applications, as the freezing point of ammonia is -77 °C. On the other hand, the use of water as the refrigerant in the water/lithium-bromide cycle limits the low temperature application to that above 0 °C and the system must also be operated under vacuum conditions. In addition, the volatility of both ammonia and water implies that the ammonia/water cycle requires a rectifier to strip away water that normally evaporates with ammonia, while the relative non-volatility of lithium-bromide means there is no need for a rectifier in the water/lithium-bromide cycle.

Figure 2.1 shows a schematic layout of a typical dual function absorption cycle. The cycle consists of a vapour generator, super heater, expander coupled to an electric generator, evaporator, absorber, throttling valve, solution pump and a heat exchanger. Heat transfer from the low grade waste heat source to the super-heater and the vapour generator is by means of a closed flow loop containing a heat transfer fluid. In the power mode, a 'weak' solution – low in absorbent concentration – is pumped using the solution pump to the vapour generator, where the refrigerant is vaporised off by the heat supplied from the waste heat source. This vapour passes through the super-heater where it is super heated and it then enters the expander where it is expanded to a low pressure, consequently driving the expander and generating electric power through the coupled generator. The resulting 'strong' solution – as it contains a strong concentration of the absorbent – in the vapour generator is throttled back to the absorber, via the heat exchanger. The purpose of the

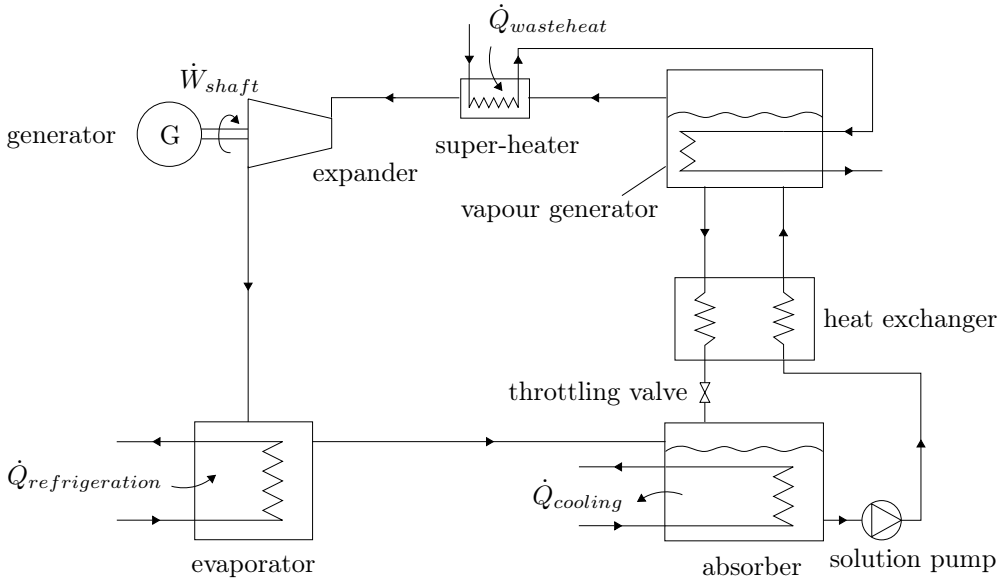


**Figure 2.1:** Dual function absorption cycle

heat exchanger is to allow heat transfer between the hot solution returning to the absorber, from the vapour generator and the cooler solution being pumped from the absorber to the vapour generator, so as to improve the coefficient of performance of the system. In the refrigeration mode, the expanded refrigerant vapour leaves the expander and passes through the evaporator where it extracts heat from an external stream, thereby evaporating and consequently cooling the external stream. The low pressure vapour from the evaporator then flows to the absorber to complete the cycle.

## 2.2 Organic Rankine cycle

An organic Rankine cycle (ORC) operates in a similar way to the more conventional steam Rankine cycle, but uses an organic working fluid rather than steam/water. The organic fluids normally used include common refrigerants such as refrigerant-123 (2,2-Dichloro-1,1,1-trifluoroethane), refrigerant-245fa (1,1,1,3,3-Pentafluoropropane) and refrigerant-134a (1,1,1,2-Tetrafluoroethane), or light hydrocarbons such as Isobutane, n-butane, isopentane, n-pentane, n-hexane and cyclo-hexane. These fluids have a lower boiling point and higher vapour pressure than water, which allows the organic Rankine cycle to operate with significantly lower waste heat temperatures, sometimes as low as 66 °C (Waste Heat Recovery: Technology and Opportunities in U.S. Industry, 2008). According to Hettiarachchi *et al.* (2007), the organic Rankine cycle has become a popular energy production cycle because it allows the recovery and utilisation of low grade waste heat in the temperature range of 100 to 200 °C. Organic Rankine cycle-based power generation is also widely applied

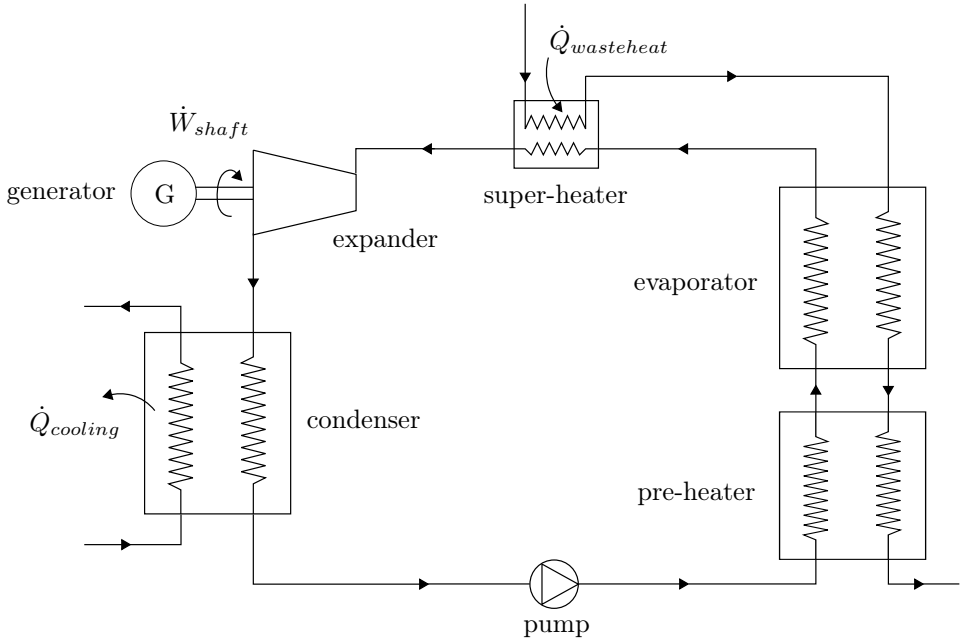


**Figure 2.2:** Organic Rankine cycle

to power generation from low temperature heat sources such as geothermal, solar thermal and biomass, with sizes as small as a fraction of 1 kW (Pei *et al.*, 2011).

Figure 2.2 shows a schematic layout of a typical organic Rankine cycle. The cycle consists of a pump, pre-heater, evaporator, super-heater, expander coupled to an electric generator and a condenser. Heat transfer from the low grade waste heat source to the super-heater, evaporator and pre-heater is by means of a closed flow loop containing a heat transfer fluid. The organic working fluid is circulated through the cycle in one closed flow loop, never coming into contact with the closed flow loop of the heat transfer fluid. During operation, the working fluid is pumped through the pre-heater, where it is preheated. The preheated working fluid is then evaporated in the evaporator, super heated in the super-heater and then expanded in the expander, consequently driving it and generating electricity through the coupled generator. On leaving the expander, the low pressure working fluid vapour enters the condenser where it is cooled at a constant pressure, using an external stream, thereafter becoming a saturated liquid. This liquid then re-enters the pump and the cycle is repeated.

In comparison with steam, the organic fluids used in an organic Rankine cycle have a higher molecular mass, enabling simpler and more compact designs, higher mass flow, and higher turbine efficiencies at lower heat source temperatures. Yamamoto *et al.* (2001) proposed a low grade heat recovery organic Rankine cycle that uses HCFC-123, also known as refrigerant-123, as the organic working fluid. This was after they obtained better cycle performance

with the organic fluid for a low temperature heat source, in a numerical and experimental study that compared HCFC-123 and water as working fluids of a Rankine cycle.

However, since the organic Rankine cycle is applied to low temperature heat sources, the overall Carnot cycle efficiencies are low (upper limits range from 10 to 20%), and these efficiencies are influenced by the temperatures of the condenser and evaporator (Waste Heat Recovery: Technology and Opportunities in U.S. Industry, 2008).

For this project, an organic Rankine cycle using refrigerant-123 as the working fluid, and with low temperature (less than 120 °C) and low pressure (less than 10 bar) operating conditions, was chosen as the low grade waste heat recovery and utilisation system.

## 2.3 Expanders for low grade waste heat recovery

In order to convert the recovered waste heat to electricity, in both the dual function absorption cycle and the organic Rankine cycle waste heat recovery and utilisation systems, an energy conversion device known as an expander is fitted into the system (see Figures 2.1 and 2.2). The purpose of the expander is to extract energy from the flowing working fluid and convert it to mechanical work. This mechanical work is further converted to electrical work by a coupled electric generator.

According to Qiu *et al.* (2011) and Lemort *et al.* (2009), an expander is critical to an organic Rankine cycle's efficiency and its selection is based on the expected operating conditions and magnitude of power output. Qiu *et al.* and Lemort *et al.* further identified the two main types of expanders as the dynamic (Turbine) type and the displacement (volume) type, with the former constituting of radial and axial inflow turbines while the latter constitutes of screw, scroll and vane-type expanders. Lemort *et al.* further argued that displacement type expanders are more appropriate to micro-scale (<10 kW) organic Rankine cycle electricity generation for low temperature and low pressure heat sources, as they are characterised by lower flow rates, much lower rotation speeds and higher pressure ratios than the dynamic type expanders. In addition, displacement machines can tolerate two-phase flow, which may appear at the end of the expansion process under some operating conditions. Wang *et al.* (2009), while noting the advantages of applying displacement expanders in lower power ranges, argue that this type of expander is affected by issues like problematic sealing, increased negative impact of friction on the expander power output, especially at sizes characterised by power output below 1 kW and the requirement of lubricant to mitigate the sealing and friction problems encountered – with the lubricant expected to be compatible with

both the working fluid used and the temperatures within the cycle – all in contrast to turbine expanders, which employ dynamic, non-contact sealing.

Qiu *et al.* carried out market research on the commercial availability of expanders applicable to micro-scale organic Rankine cycle electricity generation systems and found a scarcity of these micro-scale expanders, with the only available ones being very expensive and still at the prototype stage. Enquiries to Eneftech, Switzerland, about their 010GRE-01 model combined heat and power unit, with a rated 5 kW or 10 kW power output, returned a quote of British pounds 55000. Whilst, during the process of sourcing for a low temperature (less than 120 °C) and low pressure (less than 10 bar) turbine for this project, Infinity Turbine LLC quoted a price of US dollars 3000 for their fully assembled ITmini model organic Rankine cycle turbine, with a rated maximum electric power output of 3 kW – when coupled to a 0.6 to 3 kW, 24 to 80 V DC direct drive generator – and an operating pressure range upper limit of 20 bar. In addition, a price of US dollars 1500 was quoted for the experimental turbine kit that was eventually purchased from Infinity Turbine LLC, USA. Both the quoted for ITmini model turbine and the experimental turbine kit are not CE Certified and the manufacturer (Infinity Turbine LLC) classified them as 'Experimental' (Giese, 2012).

Qiu *et al.* further noted that the scarcity of commercially available micro-scale expanders has forced most researchers into using in-house modified or designed and manufactured expanders for their micro-scale organic Rankine cycle applications. Subsections 2.3.1 to 2.3.4 discuss the mode of operation of the different micro-scale expanders applicable to organic Rankine cycle electricity generation for low temperature and low pressure heat sources, and some examples of in-house modified or designed and manufactured expanders found in available literature are also given for each type of expander.

### 2.3.1 Scroll expander

A scroll expander is a scroll compressor operating in reverse, and is used to generate mechanical work from the expansion of a fluid. This mechanical work is further converted to electrical work, using a coupled electric generator. The scroll expander uses two interleaving scrolls – one fixed to the expander body and the other orbiting in a path defined by the fixed scroll – to expand the working fluid. The orbiting scroll is coupled to a crankshaft and the orbiting motion creates a series of pockets of fluid travelling between the two scrolls. In the center portion of the scrolls, the pockets draw in fluid, then move it to the outer portion of the scrolls, where it is discharged (see Figure 2.3). As the fluid moves in the increasingly widening pockets, it expands and the temperature and pressure of the fluid drops, consequently generating work.

Among positive displacement machines, the scroll machine is considered a good candidate for organic Rankine cycle applications, owing to its reduced number of moving parts, reliability, wide output power range and broad avail-

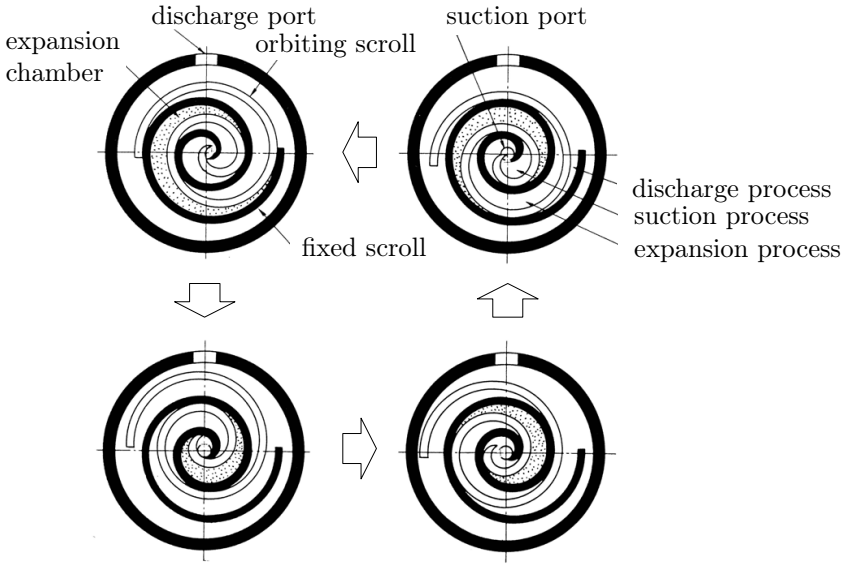


**Figure 2.3:** Operating principle of a scroll expander (Saitoh *et al.*, 2007)

ability, given its extensive use in the refrigeration and air conditioning industry (Zanelli and Favrat, 1994). However, according to Lemort *et al.* (2009), the use of scroll machines as expanders has largely remained limited to experimental work and various scroll expander prototypes have been tested for different working fluids.

Lemort *et al.* experimentally investigated an open-drive oil-free scroll expander, integrated into an organic Rankine cycle system using refrigerant-123 as the working fluid. The expander was originally an open-drive oil-free air scroll compressor, with the only modifications to it being the removal of the cooling fan and addition of insulation. For a hot air heat source within a temperature range of 101.7 to 165.2 °C and a pressure range of 5.45 to 11.12 bar, the expander, which was indirectly coupled to a 11 kW rated asynchronous machine through two belt-and-pulley couplings, generated shaft power ranging from 382 to 1820 W, at a maximum isentropic efficiency of 68%, and for exit expander pressure and temperature ranges of 1.38 to 2.66 bar and 66.4 to 128.0 °C. Similarly, Zanelli and Favrat (1994) experimentally investigated a hermetic scroll expander-generator modified from a standard hermetic compressor. The expander, which was coupled to a 3.75 kW 3 phase asynchronous 2 pole motor, was integrated with an organic Rankine cycle using refrigerant-134a as the working fluid. For a hot water heat source at a maximum temperature of 80 °C and an operating pressure ratio range of 2.4 to 4.0, the expander generated power ranging from 1.0 to 3.5 kW, at peak isentropic efficiencies in the range of 63 to 65%.

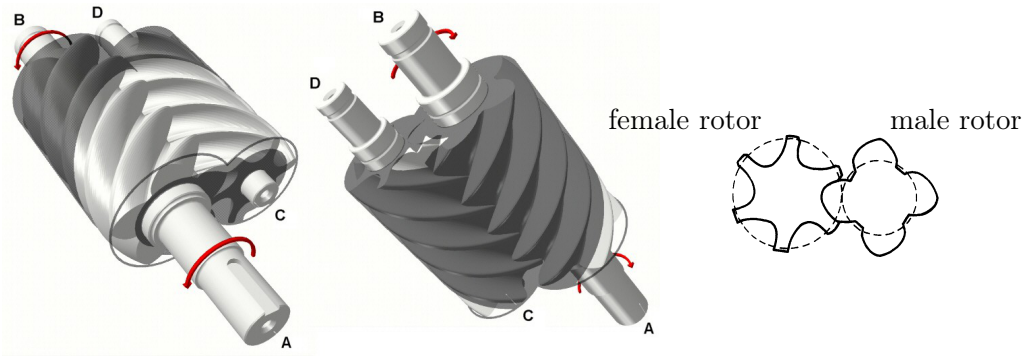


(a) (b) (c)

**Figure 2.4:** Meshing helical rotors of a screw expander; rear and top view (a), front and bottom view (b), cross-sectional view (c) (Smith *et al.*, 2005; Ng *et al.*, 1990)

### 2.3.2 Screw expander

A screw expander is a rotary positive displacement screw compressor operating in reverse, and whose key element is a pair of meshing helical rotors (see Figure 2.4) – a male and a female rotor, with the former typically having four lobes, while the latter typically has six lobes – contained in a casing which surrounds them with clearances of the order of 50 $\mu$m (Smith *et al.*, 2005; Qiu *et al.*, 2011). As the rotors rotate, the expansion volume for the working fluid is formed between the lobes and the casing wall. If fluid is admitted into this space at one end of the rotors, via an inlet port, its volume will increase until it is finally expelled from the opposite end of the rotors, via a discharge port. Rotation causes the expanding fluid to move from one end of the rotors to the other. Power is transferred between the fluid and the rotor shafts by pressure on the rotors, which changes with the fluid volume. Consequently, the fluid velocities within screw expanders are very low, thus, only a small fraction of the power transferred is due to dynamic effects inherent to fluid motion. Fluid erosion effects on the rotors are therefore eliminated and the presence of two-phase flow in the expander therefore has no effect on its mode of operation or efficiency (Smith *et al.*, 2005).

The effectiveness of the screw mechanism is dependent on high precision clearances between the helical rotors, and between the rotors and the casing wall. A good seal, both between the two rotors, and between the rotors and the casing wall ensures minimal internal leakage. In addition, Smith *et al.* outline the other requirements for efficient operation of a screw expander as correct selection of tip speed, correct choice of built in volume ratio of expansion and maximum flow area in the space formed between the lobes and the casing.

According to Qiu *et al.* (2011) and Lemort *et al.* (2013), there is little evidence of screw expanders applied with a power output lower than 10 kW (micro-scale) in available literature. Qiu *et al.* put this down to the difficulty in sealing the organic working fluid in these systems, while Lemort *et al.* put

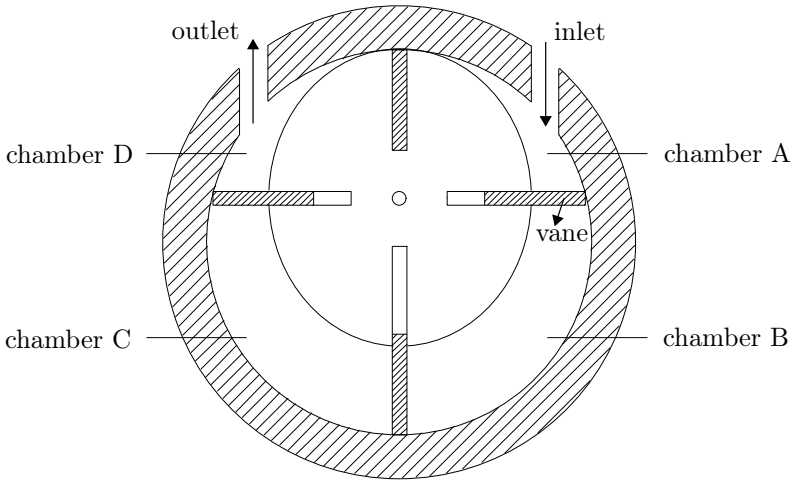


**Figure 2.5:** Operating principle of a vane-type expander; Rotor's top edge touches the housing's internal wall in the operating mode (Qiu *et al.*, 2012)

this down to the low volumetric performance of such machines. Qiu *et al.* add that most commercially available screw expanders are in the power generation range of 20 to 50 kW, with manufacturers like ORMAT and ElectraTherm only manufacturing screw expanders suitable for organic Rankine cycle power generation systems with at least 50 kW power output. Screw expanders have also found a wide application in power recovery from geothermal energy sources due to their ability to admit wet steam, as the presence of liquid together with gas has no effect on the mode of operation or efficiency of these machines.

### 2.3.3 Vane-type expanders

A vane-type expander is a vane-type air compressor operating in reverse. Its rotating element is a rotor with typically four longitudinal slots. The rotor is mounted on a shaft, and each of its slots is fitted with a freely sliding rectangular vane. During rotation, the vanes tend to move outwards against the housing wall due to the action of centrifugal forces. Expansion takes place when the chamber spaces between the sliding vanes and the housing increase as the rotor turns clockwise within the housing. During operation of the expander, the highly compressed organic working fluid vapour jets through the inlet port to form chamber A (see Figure 2.5), consequently turning the rotor. The trapped vapour is expanded as the volume of the chamber increases, until the leading vane of the chamber passes the outlet port. The pressure difference across the chambers provides the torque required to move the rotor, and this pressure difference is as a result of the vapour volume expansion (Qiu *et al.*, 2012). Hence, a higher flow rate and a larger pressure difference will provide a larger torque on the rotor, and hence a higher rotational speed, and subsequently, higher power output.

According to Yang *et al.* (2009) and Qiu *et al.* (2011), the rotary vane-type expander is of simpler construction, lower cost, higher reliability and higher compactness as compared to other expander concepts. However, Qiu *et al.* (2011) add that since vane-type expanders are originally designed for air applications, the use of organic working fluids leads to inevitable internal leaking of the working fluid, if the expanders are used without proper modification. Therefore, for their 1 kW biomass-fired organic Rankine cycle using HFE-7000 as the organic working fluid, Qiu *et al.* (2011) retrofitted a vane-type air compressor with proper sealing plates and used it as the system's expander, without any operating problems. For a hot water heat source of 127 °C, and with an expander inlet temperature and pressure of 113 °C and 5.38 bar and pressure ratio of 2.0, the expander generated 792 W of electric power, via an indirectly coupled 140 A, 14 V rated Bosch automotive alternator. Similarly, with an intention to develop an economically efficient organic Rankine cycle system with a turbine power output of less than 1 kW, b. Mohd. Tahir *et al.* (2010) developed an experimental organic Rankine cycle electricity generating system using a rotary vane-type expander, and refrigerant-245fa as the organic working fluid. For hot and cold water sources within temperature ranges of 60 to 100 °C and 10 to 30 °C, the system was tested at maintained temperature differences between the hot and cold sources of 60 °C, 70 °C and 80 °C, and obtained maximum expander power of 32 W, at a maximum expander efficiency of 48%, for the 80 °C temperature difference. They concluded that this implied that, for this type of expander, maximum torque and power can be obtained at maximum pressure difference, and a working fluid that maximises the pressure difference for a particular temperature difference should be selected.

### 2.3.4 Turbine expanders

A turbine expander is of the dynamic or velocity type as a high velocity vapour stream (working fluid) is required to drive the turbine. By expanding the vapour stream flowing through its rotor blades, the turbine rotor extracts and converts the vapour stream's kinetic energy into mechanical energy.

Turbine expanders are classified as either radial inflow or axial inflow, depending on the mode of intake of the working fluid into the machine, that is, normal to the axis of rotation, for the former and, parallel to the axis of rotation, for the latter. According to Whitfield and Baines (1990), radial inflow turbines historically preceded axial inflow turbines, and they are capable of higher specific work transfer as compared to axial flow turbines of the same speed and mass flow rate, owing to the change in radius across the rotor as the fluid flows through the rotor. However, the sudden turning of the fluid flow in radial inflow turbines results in higher energy losses due to friction, leading to a reduction in specific work.

According to Aungier (2006), radial inflow turbines are very attractive for small single stage turbine units, such as turbochargers and micro-turbines, owing to their low sensitivity to blade profile tolerance issues and thus require less blades per blade row, as compared to axial inflow turbines which require maintaining of the blade profile accuracy level required for high efficiency. This makes their design less complex and cheaper, as compared to that of axial inflow machines. Pei *et al.* (2010) outline the other radial inflow turbine advantages as compact structure with good manufacturability, lightweight construction, high efficiency and a single stage expansion rate that indicates a big enthalpy drop. Pei *et al.* further added that the aforementioned advantages have boosted the wide application of radial inflow turbines in low flow and low power systems, such as air conditioning systems in aeroplanes, cryogenic devices and small gas turbines.

According to Pei *et al.* (2011), there is very little information on the practical usage of turbine expanders in organic Rankine cycles, with most previously investigated expanders being commercial devices designed for purposes other than organic Rankine cycle application. These converted devices are unable to achieve the desired high efficiencies in the organic Rankine cycle. Pei *et al.* (2010, 2011) therefore designed and manufactured a radial inflow turbine to be applied to 3.75 kW organic Rankine cycle system using refrigerant-123 as the working fluid. Preliminary tests of the manufactured turbine involved using compressed air as the working fluid. The air simulated the organic fluid, and its choice was based on its ability to maintain its gaseous state – thus prevent formation of liquid droplets that would erode the turbine blades – and the need to determine the turbine performance using compressed air, to determine its practical significance in the recovery of released residual pressure energy in industrial processes, such as those of cement factories, chemical plants, metallurgical industries, among others. For the air test, the turbine generated 620 W of electric power, via an indirectly coupled generator, while for the organic Rankine cycle test, a turbine shaft power of 1 kW, at turbine isentropic and cycle efficiencies of 65% and 6.8% was obtained. Kang (2012) designed and manufactured a 12 blade radial inflow turbine that was experimentally tested in a 30 kW organic Rankine cycle electricity generating system using refrigerant-245fa as the working fluid. For a turbine inlet pressure and pressure ratio of 7.32 bar and 4.11, condenser pressure of 1.78 bar and an average evaporator temperature of 82.3 °C, the turbine generated a maximum average electric power output of 31.2 kW, via a directly coupled high-speed brushless synchronous generator, at maximum average cycle and turbine efficiencies of 5.22% and 78.7%.

Despite the advantages of using positive displacement machines as expanders in the recovery of low grade waste heat using the organic Rankine cycle, a radial inflow turbine expander was chosen for this project. The choice of expander was influenced by its geometrically simpler structure, as compared to positive displacement machines which have complex shapes of their moving

parts, with closely engineered tolerances, making their manufacturing costlier. The intention was also to use a device purposefully built for organic Rankine cycle applications. From available literature, it is seen that most of the expanders applied in the organic Rankine cycle for the recovery of low grade waste heat are commercial devices designed for purposes other than organic Rankine cycle application. These converted devices are based on existing compressor mechanisms, and are unable to achieve desired efficiencies when operated in expander mode. Therefore, an experimental radial inflow turbine kit was sourced from Infinity Turbine LLC. This turbine kit was assembled and the turbine tested with compressed air, in order to characterise it for low temperature and low pressure conditions. In addition, a new radial inflow turbine rotor was also designed and manufactured, and similarly tested with compressed air, in order to characterise it for low temperature and low pressure conditions. Using the determined turbine performance characteristics, the designed radial inflow rotor was then theoretically scaled for refrigerant-123 application, in order to predict its performance for integration in an organic Rankine cycle waste heat recovery and utilisation system.

The mode of operation of a radial inflow turbine, as well as its performance analysis is discussed in the proceeding section.

## 2.4 Radial inflow turbines

During the operation of a radial inflow turbine, the working fluid enters the turbine rotor in a radially inward direction, that is, normal to the axis of rotation, with an absolute velocity vector $V_2$ and a velocity vector relative to the blade $W_2$. The impinging of the fluid onto the blade causes it to rotate at a tip speed $U_2$ (see Figure 2.6a). The rotor blades have a gradual radial to axial turn in the meridional plane, and this turns the fluid flowing through the blade passage into the axial direction. The fluid then leaves the rotor with an absolute velocity vector $V_3$ and a velocity vector relative to the blade $W_3$, with $U_3$ being the average blade speed at the rotor exit (see Figure 2.6b)

### 2.4.1 Analysis

Fluid flow through a turbine blade row is complex, as a result of being unsteady, three-dimensional, viscous, compressible and often transonic or supersonic. This is further compounded by leakage flows between the blade tip and casing (shroud) (Whitfield and Baines, 1990).

According to Aungier (2006), one-dimensional analysis or mean line method is the most effective method for radial inflow turbine performance analysis. Whitfield and Baines (1990) add that in the preliminary design and analysis of turbomachines, it is common to assume one-dimensional fluid flow, with a streamlined fluid path that follows the blade geometry, with possible excep-

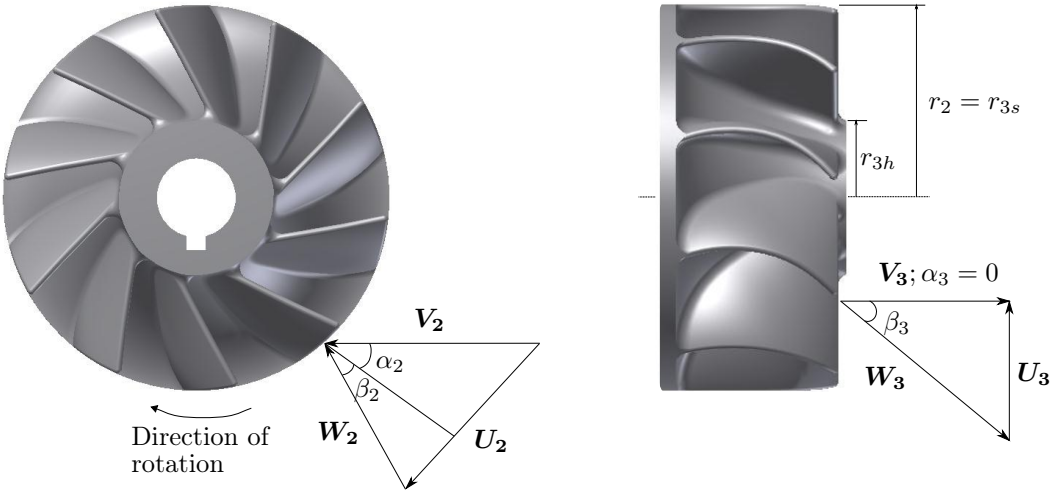


(a) Inlet (b) Exit

**Figure 2.6:** Radial inflow turbine rotor velocity triangles

tion of incidence at the leading edge and deviation at the trailing edge of the blade. Whitfield and Baines further add that this flow can be characterised by parameters like pressure, temperature, velocity and flow angle and can be modelled based on four equations; the three conservation equations and the second law of thermodynamics.

For this project, the flow is modelled as steady, one-dimensional, adiabatic, compressible flow and the performance analysis of the turbine is based on the three conservation laws; conservation of mass, conservation of momentum and conservation of energy.

### *Conservation of mass*

Consider a fluid system defined by the turbine as a single horizontally oriented control volume, with two control stations – the inlet and outlet, as shown in Figure 2.7.

Applying the general statement of the conservation of mass

$$\frac{\triangle m}{\triangle t} = \sum \dot{m}_{in} - \sum \dot{m}_{out}$$

to the control volume shown in Figure 2.7, for steady flow $\frac{\triangle m}{\triangle t} = 0$ yields

$$\dot{m}_{in} = \dot{m}_{out} = (\rho V A_x)_{in} = (\rho V A_x)_{out} \tag{2.1}$$

Where $\dot{m}$ is the mass flow rate of the working fluid through the cross sectional area $A_x$, $\rho$ is the fluid density and $V$ is the fluid velocity, in the flow direction, at each of the two control stations.

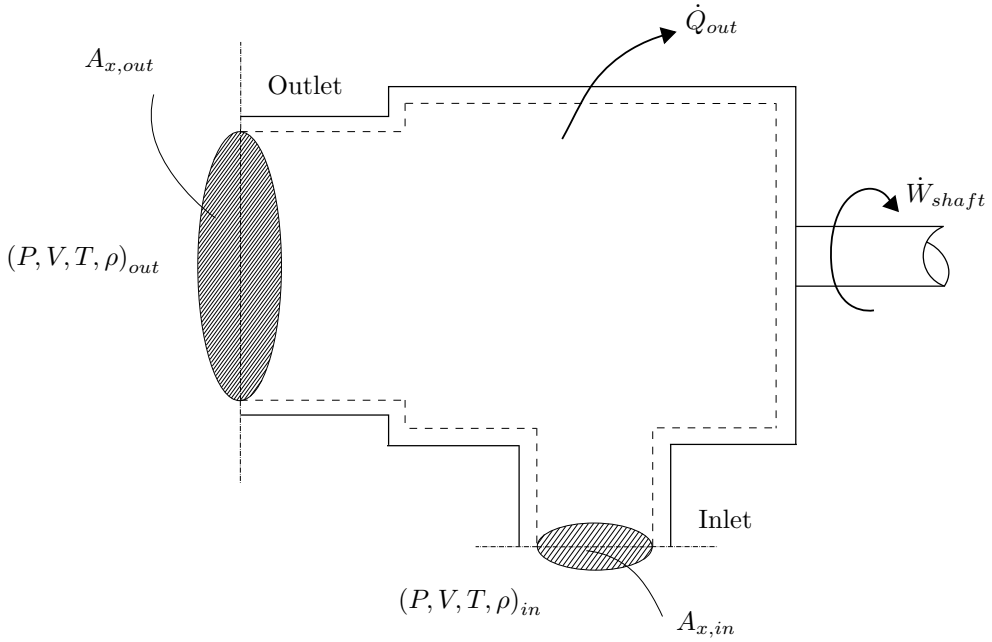


**Figure 2.7:** Turbine as a single control volume

### *Conservation of momentum*

According to Cengel and Cimbala (2010), radial flow machines are best analysed using the angular momentum equation, based on the principle of conservation of momentum, owing to the large changes in the angular momentum of the fluid flowing through them.

Daugherty *et al.* (1985) notes that, owing to the change in radius of the blade passage as fluid flows through a rotor, torque, rather than force, is computed. The resultant torque is then given by the summation of the torques produced by all the forces, also equivalent to that torque produced by two single forces acting at the inlet and exit of a blade row.

Assuming very thin blades, with all their elements parallel to the axis of rotation, application of the angular momentum equation

$$\sum T = \sum_{in} r\dot{m}V - \sum_{out} r\dot{m}V$$

to the control volume previously defined, while also noting that only the tangential velocity components contribute to the torque, yields

$$T = \dot{m}\left(r_2 V_{2,t} - r_3 V_{3,t}\right)$$

For fluid flow through the blade passage of a radial inflow turbine, Figure 2.8a shows that, at the blade inlet, the absolute flow velocity has both a tangential and a normal component, while at the blade exit, for no swirl conditions at the

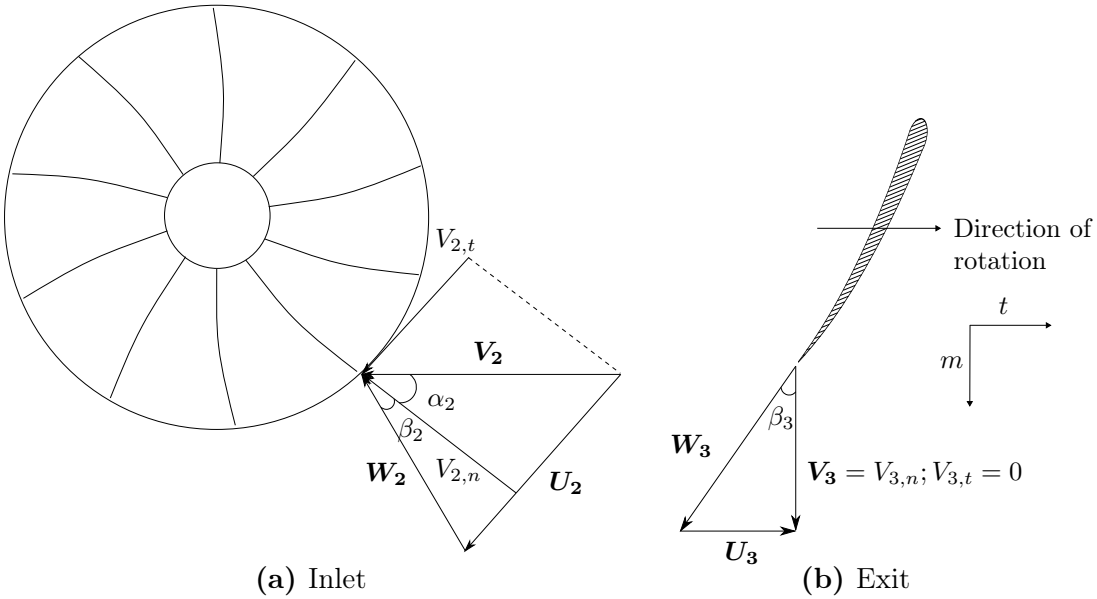


**(a)** Inlet **(b)** Exit

**Figure 2.8:** Velocities entering and leaving a turbine blade row (for $\alpha_3 = 0$)

design point operating condition ($\alpha_3 = 0$), Figure 2.8b shows that the absolute flow velocity has only a normal component. The equation for torque therefore reduces to

$$\begin{aligned} T &= \dot{m} r_2 V_{2,t} \\ &= \dot{m} r_2 V_2 \sin \alpha_2 \end{aligned}$$

If the rotor rotates at an angular velocity $\omega$, then the shaft power output of the turbine is given by

$$\dot{W}_{shaft} = \omega T = \dot{m} \omega r_2 V_2 \sin \alpha_2 \tag{2.2}$$

Equation (2.2) is the Euler turbo machinery equation for no swirl conditions at the blade exit, at the design point operating condition (absolute flow velocity at the rotor exit designed to be fully axial), and relates the turbine shaft power output to the turbine flow geometry.

### *Conservation of energy*

A turbine is a work transfer device and it extracts energy from a flowing fluid and transfers it to an output shaft.

Applying the principle of conservation of energy to the control volume previously defined, while noting that energy transfer to or from a system can be by the form of heat, work and mass transfer, yields

$$\frac{\triangle E}{\triangle t} = \left[\dot{m}\left(\frac{P}{\rho} + u + gz + \frac{V^2}{2}\right)\right]_{in} - \left[\dot{m}\left(\frac{P}{\rho} + u + gz + \frac{V^2}{2}\right) + \dot{Q} + \dot{W}\right]_{out}$$

Where $\frac{P}{\rho}$ is the flow work per unit mass, $u$ is the fluid internal energy per unit mass, $gz$ is the fluid potential energy per unit mass, $\frac{V^2}{2}$ is the fluid kinetic energy per unit mass, $\dot{Q}$ is thermal energy out and $\dot{W}$ is work energy out.

Noting that for steady flow, $\frac{\triangle E}{\triangle t} = 0$, and for one dimensional flow, $V = \frac{\dot{m}}{\rho A_x}$, rearranging yields

$$0 = \dot{m}\left[\left(\frac{P}{\rho}\right)_{in} - \left(\frac{P}{\rho}\right)_{out}\right] + \dot{m}\left[gz_{in} - gz_{out}\right] + \dot{m}\left[u_{in} - u_{out}\right] + \dot{m}\left[\left(\frac{\dot{m}^2}{2\rho^2 {A_x}^2}\right)_{in} - \left(\frac{\dot{m}^2}{2\rho^2 {A_x}^2}\right)_{out}\right] - \dot{W}_{out} - \dot{Q}_{out}$$

Rearranging and noting that for a horizontal inlet and outlet $z_{in} = z_{out}$ and for an adiabatic turbine $\dot{Q}_{out} = 0$ and further noting that increase in internal energy $- \triangle u = (u_{in} - u_{out})$, due to the irreversible conversion of mechanical energy to thermal energy as a result of friction maybe defined as an energy loss $\dot{E}_{loss} = \sum_{i}^{N} k\frac{V^2}{2}$, where $k$ is a loss coefficient at a point $i$ through the flow passage, and $\dot{W}_{out} = \dot{W}_{shaft}$ yields

$$0 = \dot{m}\left[\left(\frac{P}{\rho}\right)_{in} - \left(\frac{P}{\rho}\right)_{out}\right] + \frac{\dot{m}^3}{2}\left[\left(\frac{1}{\rho^2 {A_x}^2}\right)_{in} - \left(\frac{1}{\rho^2 {A_x}^2}\right)_{out}\right] - \dot{W}_{shaft} - \frac{\dot{m}^3}{2}\left[\sum_{i=1}^{N} k_i \frac{1}{{\rho_i}^2 {A_{x,i}}^2}\right] \tag{2.3}$$

The turbine shaft power output $\dot{W}_{shaft}$ can be obtained from Equation (2.3), given the working fluid thermodynamic properties at the inlet and exit of the machine and information on the loss coefficients throughout the flow passage of the turbine.

### 2.4.2 Performance characteristics

According to Whitfield and Baines (1990), the overall performance characteristics of a turbomachine can be described by ten basic parameters, expressed in functional form as

$$f\left(d_2, N, \dot{m}, P_{01}, P_{03}, T_{01}, T_{03}, R, \gamma, \mu\right) = 0$$

Where subscripts 1 and 3 represent the inlet and exit stations of the machine, subscript 2 represents the turbine rotor inlet (see Figure 2.9), $d_2$ is a characteristic linear dimension – considered to be the rotor blade tip diameter for radial inflow turbines, $N$ is the turbine rotor rotation speed, $R$ is the specific gas constant, $\gamma$ is the specific heat ratio and $\mu$ is the dynamic viscosity.

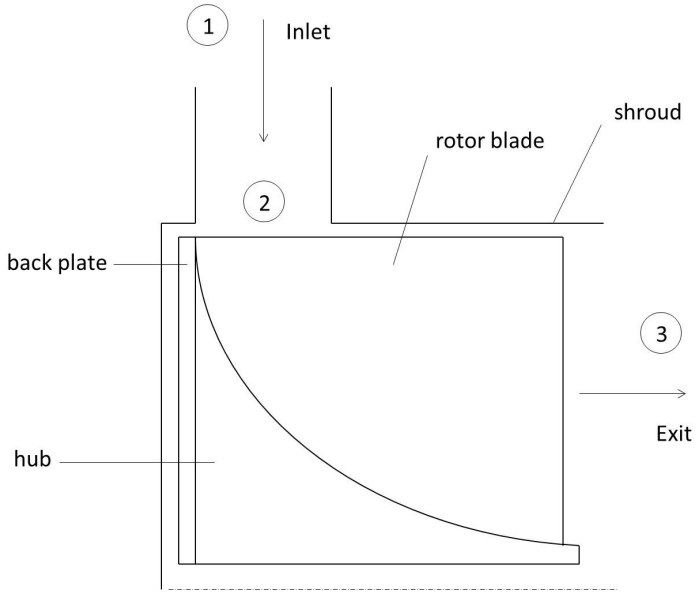


**Figure 2.9:** Typical radial inflow turbine notation (adapted from Whitfield and Baines, 1990)

For a single working fluid application, and neglecting effects such as viscosity(Reynolds number) – on account of sufficiently high flow Reynolds numbers in turbomachines, such that modest changes in magnitude have minimal effect on performance, Whitfield and Baines (1990) further suggest that these ten basic parameters can be reduced, depending on the number of fundamental dimensions (mass, length, time and temperature) involved, to four non-dimensional groups, expressed in functional form as

$$f\left(P_R, \eta, \theta, M_u\right) = 0 \tag{2.4}$$

Where $P_R$ is the inlet total to exit static turbine pressure ratio, and is given by

$$P_R = \frac{P_{01}}{P_3} \tag{2.5}$$

The pressure ratio is the non-dimensional representation of the pressure drop across the turbine, and exit static pressure conditions are considered because the exhaust kinetic energy for a single stage turbine is not recovered.

The second term $\eta$ is the turbine efficiency, defined as the ratio of the actual enthalpy change (actual work output) to that which would occur for an isentropic flow process, indicated by enthalpy change between state points 1 to 3 and 1 to 3ss on the mollier chart in Figure 2.10. For an adiabatic expansion process through a single stage turbine, this efficiency is more appropriately specified as total to static efficiency, and is given by

$$\eta_{t-s} = \frac{h_{01} - h_{03}}{h_{01} - h_{3ss}}$$

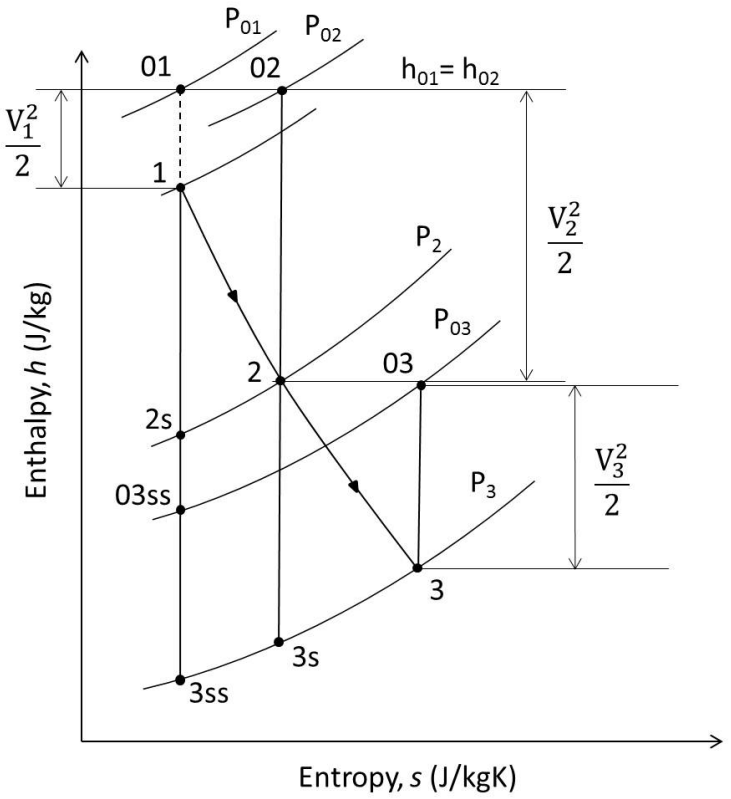


**Figure 2.10:** Mollier chart for a radial inflow turbine (adapted from Dixon, 1998)

And noting that, for an ideal gas, $h = c_p T$ yields

$$\eta_{t-s} = \frac{T_{01} - T_{03}}{T_{01} - T_{3ss}}$$

Since the pressure at state point $3ss$ is $P_3$ (see Figure 2.10), then using the isentropic relation between temperature and pressure ratios for an ideal gas $(T/T_0) = (P/P_0)^{(\gamma-1)/\gamma}$, the total to static efficiency is now given by

$$\eta_{t-s} = \frac{1 - (T_{03}/T_{01})}{1 - (P_3/P_{01})^{(\gamma-1)/\gamma}} \tag{2.6}$$

The third term $\theta$ is the non-dimensional mass flow rate, obtained from the ratio of the actual mass flow rate to that through an orifice of diameter $d_2$ and flowing with a velocity equal to the inlet stagnation speed of sound $C_{01} = \sqrt{\gamma R T_{01}}$. It is given by

$$\begin{aligned} \theta &= \frac{\dot{m}}{\rho_{01} C_{01} \pi d_2^2/4} \\ &= \frac{\dot{m}\sqrt{(RT_{01}/\gamma)}}{P_{01}\pi d_2^2/4} \end{aligned} \tag{2.7}$$

The fourth term $M_u$ is the non-dimensional rotor blade tip speed, obtained from the ratio of the rotor blade tip speed to the inlet stagnation speed of sound. It is given by

$$\begin{aligned} M_u &= \frac{U_2}{C_{01}} \\ &= \frac{N d_2 \pi}{\sqrt{(RT_{01})} 60 \sqrt{\gamma}} \end{aligned} \tag{2.8}$$

Whitfield and Baines (1990) give some typical performance maps for radial inflow turbines operating over a range of pressure ratios (see Figure 2.11) and also note the weak dependence of these turbine performance maps on the non-dimensional rotor blade tip speed $M_u$.

The shaft power developed by the turbine is another important turbine performance parameter not directly defined by the four non-dimensional performance groups of Equation (2.4) (Whitfield and Baines, 1990). This power can be determined from the application of the principle of conservation of energy to the operation of a radial inflow turbine, as given by Equation (2.3). Whitfield and Baines further define a non-dimensional specific power coefficient or power ratio $S_w$, given as a function of the turbine shaft power output $\dot{W}_{shaft}$ by the expression

$$S_w = \frac{\dot{W}_{shaft}}{\dot{m} h_{01}} \tag{2.9}$$

Neglecting frictional, recirculation and mechanical loses, the power developed by the turbine can be expressed in terms of stagnation enthalpy change, that is, $\dot{W}_{shaft} = \dot{m}(h_{01} - h_{03})$, thus yielding

$$\begin{aligned} S_w &= 1 - \frac{h_{03}}{h_{01}} \\ &= 1 - \frac{T_{03}}{T_{01}} \end{aligned} \tag{2.10}$$

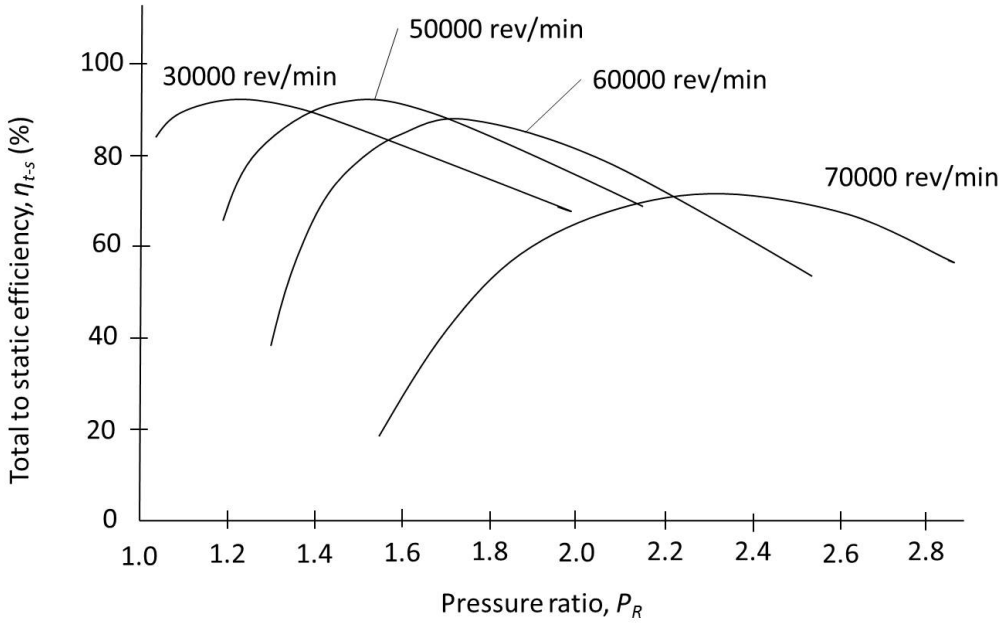


**(a)** Total to static efficiency vs pressure ratio

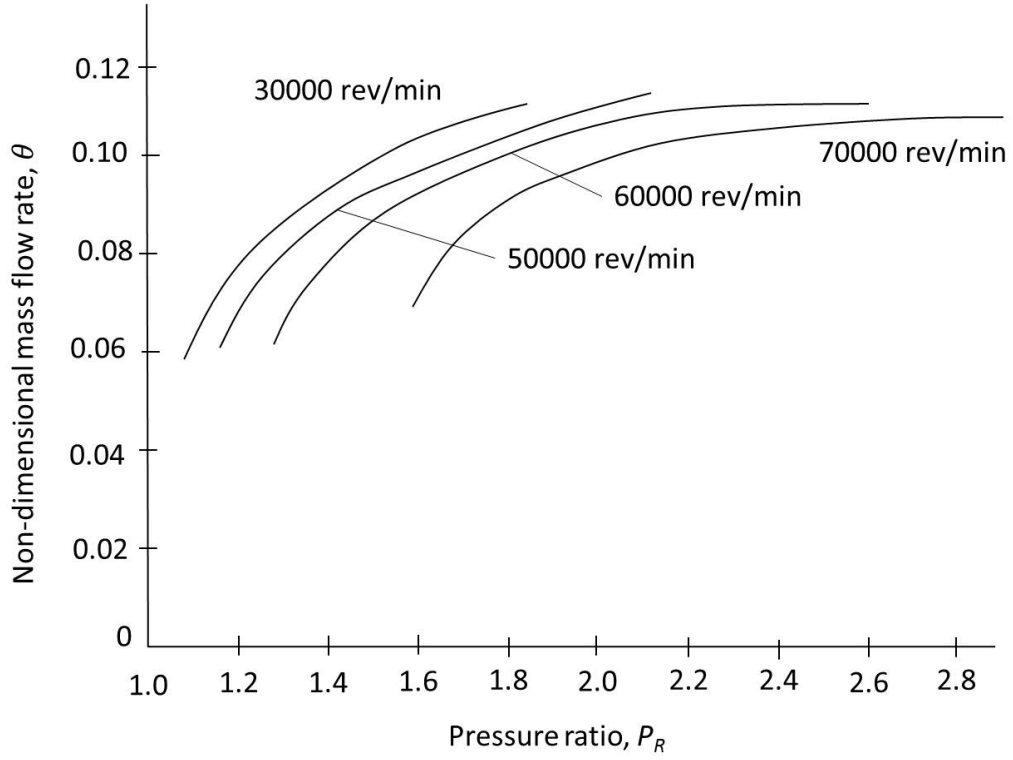


**(b)** Non-dimensional mass flow rate vs pressure ratio

**Figure 2.11:** Typical radial inflow turbine performance maps (Whitfield and Baines, 1990)

# Chapter 3

# Experimental and Design Work

The purpose of the experimental work was to characterise a turbine and validate its use for low temperature (less than 120 °C) and low pressure (less than 10 bar absolute) conditions, in order to determine its suitability for application in a proposed in-house organic Rankine cycle low grade waste heat recovery and utilisation system. This was achieved through performing an air test, using compressed air as the working fluid, similar to Pei *et al.* (2010, 2011), but with the choice of compressed air being influenced by firstly, its ability to maintain its ideal gas state, enabling the use of simplifying ideal gas relations in the analysis of the turbine performance and secondly, by it being readily available in the laboratory set-up. According to Aungier (2006), its often convenient to test a turbine stage in one working fluid, for example air, but then apply it to a different working fluid, such as steam.

The air test involved designing and building a test bench and then using it to test, analyse and characterise an acquired and assembled experimental waste heat turbine kit for low temperature and low pressure conditions. This turbine's performance had as yet not been determined for low temperature and low pressure conditions. Also, due care was taken to experimentally calibrate all the temperature and pressure sensors, in addition to the spring loaded scale, in order to eliminate the bias error in their measurements.

As part of the project design work, a new radial inflow turbine rotor was designed and manufactured. This was done for two purposes: firstly, to provide flow geometry, such as blade inlet and exit velocity triangles and blade and flow angles, necessary for the analysis of the operation of a radial inflow turbine. This was necessary, as there was no flow geometry availed for the acquired waste heat turbine rotor. Secondly, to improve on the flow passage through the turbine, in order to improve the overall turbine efficiency. The designed rotor was also tested and analysed with air, in order to determine the new turbine performance characteristics.

Through the experimental work, the influence of performance parameters, such as the working fluid properties at the turbine inlet and outlet, the mass flow rate through the turbine and the turbine shaft rotation speed, on the

turbine performance was determined and presented in the form of turbine performance maps.

## 3.1 Turbine and generator

A commercially available low grade waste heat experimental turbine kit was acquired, assembled, tested and characterised for low temperature and low pressure conditions. The turbine kit was an ITmini waste heat turbine experimental kit, sourced from Infinity Turbine LLC, USA. This kit consisted of an aluminium alloy AL 6082 adaptor block, with $1^1/_2$ -11.5 NPT female thread, an aluminium alloy AL 6082 hexagonal front bearing block, an aluminium alloy AL 6082 hexagonal turbine and bearing (mid) block, with a welded piece of pipe of $^3/_8$-18 NPT female thread, one plastic and one aluminium alloy AL 6082 hexagonal back block, two face 'disc' type magnetic couplers; one with 10 mm bore and the other with a 12.7 mm bore, a 10 mm diameter 304 stainless steel shaft, a 304 stainless steel turbine rotor consisting of seven fin-like bladed plates of 3 mm thickness and 49.86 mm diameter and one back plate of the same dimensions, three 034 silicone, 70A Durometer red O-ring seals, six ANSI B18.3-10-32 UNF-1.75 hexagon socket head cap screws, six ANSI B18.3-10-32 UNF-1.25 hexagon socket head cap screws, four McMaster Carr 91482A260 internal Circlips, four McMaster Carr 91650A340 spring retainer rings and finally, two $10 \times 19 \times 5$ mm sealed deep groove ball bearings. The experimental turbine kit was assembled according to the assembly plans/drawings provided with the kit. These plans are added in Appendix D. A sectioned front view of the assembled turbine unit (with the ITmini waste heat turbine rotor replaced by the designed rotor, for purpose of clarity) can also be seen in Figure 3.3.

In order to determine the turbine performance parameters such as the mass flow rate, inlet and outlet pressure and temperature and shaft rotation speed, the turbine had to be mechanically loaded. This was achieved through coupling it to a DC motor, with an electric load connected across the motor terminals, as illustrated by Figure 3.1. Electrically loading the DC motor, subsequently mechanically loaded the turbine that was coupled to it. A commercially available AmpFlow E30-150 brushed DC motor (hereinafter called generator) was sourced from Powerhouse Engineering Inc, USA, for this purpose. For a DC voltage output of 24 V, the generator shaft had a rated no-load speed and maximum power output of 5600 rpm and 745.7 W, respectively.

The electric load consisted of twelve 10 W, 12 V DC rated capsule type G4 halogen lamps, connected two in series, making a total of six parallel columns. The choice of low wattage rated lamps allowed the turbine to be loaded in small increments, thus increasing its test points. Each of these lamps was held in a 10 A, 50 V rated GU5-3 Spring clip halogen lamp holder and each column of lamps was provided with a 1P green C5503PLLAB LED on-off smooth rocker

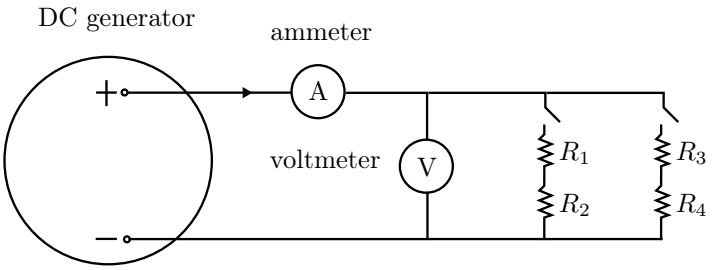


**Figure 3.1:** Electric load circuit

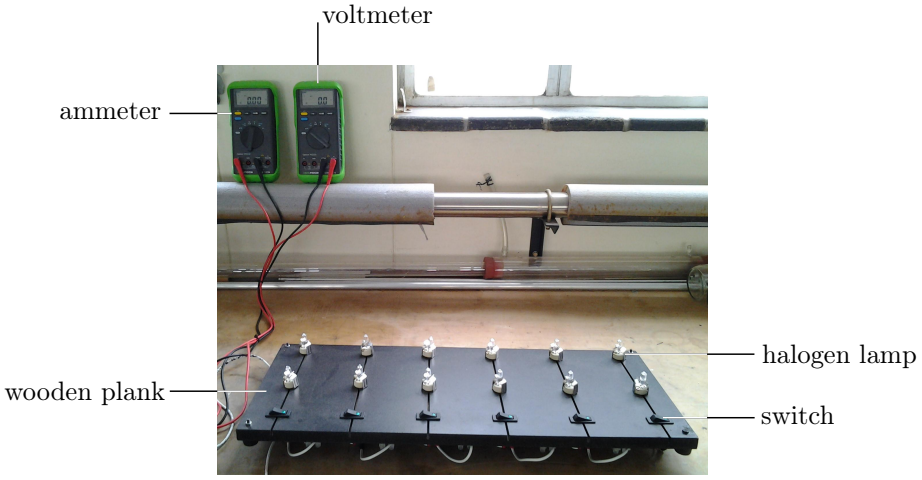


**Figure 3.2:** Electric load

switch. The connections for the electric load were done using 1.5 mm$^2$ single core white equipment wire, 12 mm$^2$, 15 A rated plastic terminal block screw wire connectors and 0.5 to 1.5 mm$^2$ red shrouded receptacle crimp terminals. The lamp holders and terminal block wire connectors were screwed onto a 580.0 × 235.5 × 20.0 mm wooden plank, while the switches were fitted into $30 \times 11 \times 20$ mm slots cut through the wooden plank, as shown in Figure 3.2.

The generator and the turbine were magnetically coupled, using the two magnetic couplers provided with the turbine kit; the 10 mm bore coupler fastened onto the 10 mm diameter turbine shaft using two M5 × 8 hexagon socket grub screws, and the 12.7 mm bore coupler fastened onto the 12.7 mm diameter generator shaft, using two M5 × 8 hexagon socket grub screws and a feather key. An air gap of 1 mm on either side of the plastic back block covering the turbine shaft coupler was left between the couplers. According to Waring *et al.* (1996), eight or ten poles is the maximum feasible number of poles on a small coupling and for a test air gap of 5 mm, the eight-pole coupling has maximum torque capacity of 0.8 N·m, while the ten-pole coupling has a maximum torque capacity of 0.6 N·m. The magnetic coupling allowed synchronous rotation between the two concentric axes of the turbine and generator shafts and transmission of torque without any physical contact. This eliminated the need for a lip seal and the possibility of leaking issues arising, as is common with

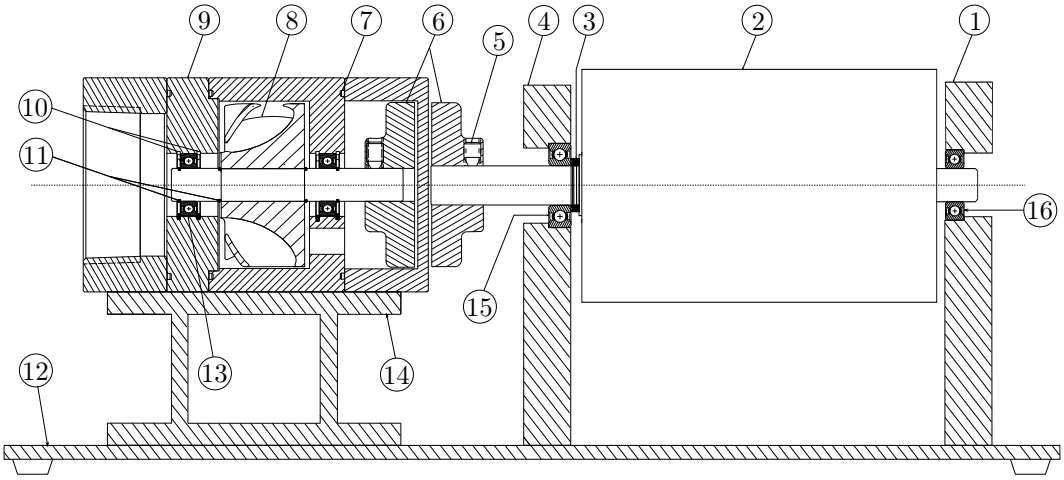


**Figure 3.3:** Sectioned front view of the turbine-generator mounting; 1. Generator mounting back bracket, 2. Generator, 3. Three piece needle roller thrust bearing of overall dimensions 12.7 × 23.8 × 4.3 mm, 4. Generator mounting front bracket, 5. M5 × 8 hexagon socket grub screw, 6. Face type disc magnetic couplers, 7. O-ring seal, 8. Turbine rotor, 9. Turbine casing, 10. Internal circlips, 11. Spring retainer rings, 12. Mounting platform, 13. 10 × 19 × 5 mm sealed deep groove ball bearing, 14. Turbine mounting bracket, 15. 12.7 × 28.0 × 8.0 mm shielded deep groove ball bearing and 16. 9.5 × 22.0 × 7.0 mm shielded deep groove ball bearing

the use of more traditional contact type couplers (Waring *et al.*, 1996). The magnetic coupling also allowed easier alignment and balancing of the shafts onto which the couplers were fastened.

The coupled turbine and generator were then mounted as shown in Figure 3.3. The mode of mounting is explained, in turn, as follows: A mounting platform for the turbine-generator coupling was first provided. This platform consisted of a 350 × 212 × 6 mm mild steel base plate, with four 20 mm diameter rubber door stops bolted at its bottom, 12 mm away from each of its four corners.

The mode of mounting of the generator was such that, it was free to rotate about its shaft axis. This was necessary for the proper operation of the purposely built dynamometer, set-up for the determination of the torque exerted by the turbine shaft onto the coupled generator shaft. Two 80 × 16 × 130 mm mild steel flat bars were provided as generator mounting brackets; one for the front of the generator and the other for its back. The front mounting bracket had a 20 mm diameter bore, drilled 106 mm from the datum of the bracket, and with a 28 mm diameter counter bore, of depth 8 mm. A 12.7 × 28.0 × 8.0 mm shielded deep groove ball bearing was press fit into this bracket, with the counter bore providing shoulder support for the bearing. The back bracket had a 15 mm diameter bore, also drilled 106 mm from the datum of the bracket, with a 22 mm diameter counter bore of depth 7 mm. A 9.5 × 22.0 × 7.0 mm shielded deep groove ball bearing was press fit into this bracket, with the

counter bore providing shoulder support for the ball bearing as well.

The choice of different size ball bearings was influenced by the different generator shaft diameters at both ends of the generator; 12.7 mm at the front and 9.5 mm at the back, while the choice of metal shielded bearings, rather than rubber sealed bearings, was mainly influenced by the expected contact between the bearings' outer rings and the shoulders in the brackets, once press fit into the brackets. The ball bearings in the generator mounting set-up took up the radial load from the torque exerted by the turbine shaft onto the coupled generator shaft, while a three piece needle roller thrust bearing was also provided in the generator mounting set-up, to take up the axial/thrust load developed from the axial attractive forces between the magnetic couplers. The raceway washer of the thrust bearing was in contact with the rotating inner ring of the ball bearing in the front bracket while the thrust washer was in contact with the motor face, to take up the thrust from the motor face pressing onto it. The needle roller was positioned between these two washers. The expected contact between the raceway washer and the ball bearing also influenced the choice of a metal shielded ball bearing for the front bracket.

The mode of mounting of the turbine required that the turbine shaft axis be concentric with that of the mounted generator, and that the turbine mounting bracket be able to move horizontally forward and backwards, so as to be able to vary the air gap between the plastic back block and the generator magnetic coupler. The concentricity between the shaft axes was achieved through providing a mounting bracket that raised the turbine shaft axis to a height of 106 mm from the mounting base plate – same height from the datum as the shaft of the mounted generator. Also, four $10 \times 6$ mm slots were cut through the mounting base plate, for the mounting of the turbine mounting bracket. These slots allowed horizontal linear movement of the turbine mounting bracket. The turbine was bolted onto its mounting bracket using four $M5 \times 20$ steel hexagon socket head cap screws and four M5 steel nuts and washers. And finally, the generator and turbine mounting brackets were all bolted to the mounting base plate using $M5 \times 20$ steel hexagon socket head cap screws and M5 steel nuts and washers.

## 3.2 Air test

In order to characterise the turbine for low temperature and low pressure conditions, an air test was performed, using a specially designed and built test bench. The test apparatus used in the test bench had to be able to measure, vary and control the primary turbine performance parameters, such as the air pressure and temperature at the turbine inlet and outlet, the air mass flow rate through the turbine and the turbine shaft rotation speed, in order to determine their influence on the turbine performance.

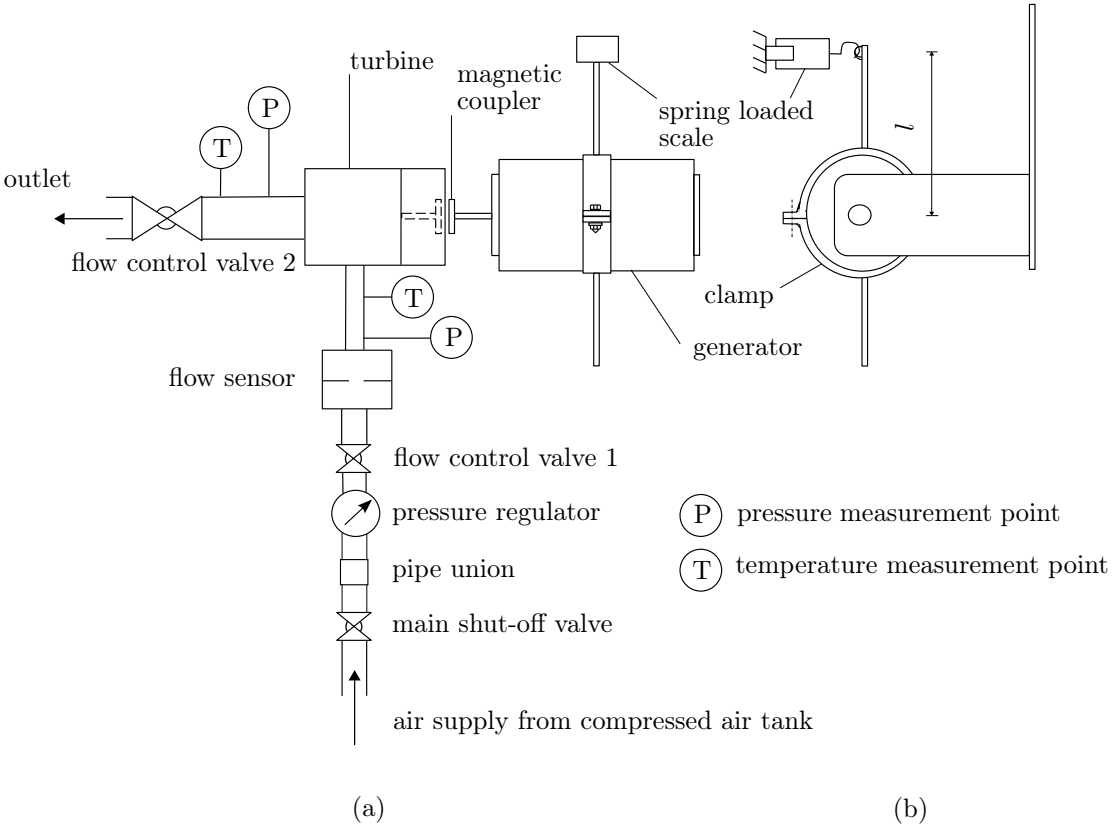


**Figure 3.4:** Schematic layout of experimental air test bench; plan view (a), partial side view, illustrating the dynamometer set-up (b)

### 3.2.1 Experimental air test bench

The test bench was based on an open-cycle arrangement, with the air supply to the turbine coming from a compressed air tank, while the air discharge from the turbine was exhausted to the atmosphere – the latter condition allowing for maximum pressure drop across the turbine stage, by keeping the gauge pressure at the turbine outlet as close as possible to zero. The test bench was purposely built for air, using apparatus suited for air applications, and Figure 3.4 shows its schematic layout. The instrumentation used on the test bench is discussed, in turn, as follows:

#### *Pressure regulator*

The pressure of the air supplied from the compressed air tank is set at 10 bar. A Festo LFR-1 series filter regulator, with a measuring range of 0.5 to 12 bar, was used to manually control and vary the pressure of the air supplied to the test bench. This was done by turning the knob on the pressure regulator, until the desired air pressure was displayed on the gauge fitted onto the regulator. The regulator also had an added function of smoothing out pressure fluctuations

from the supply line, which if left, would affect the proper functioning of the flow sensor installed downstream of it. The regulator is also fitted with a filter, to trap dust particles in the supply line.

### *Flow sensor*

A Festo SFAM-90 series flow sensor, factory calibrated at standard conditions (0 °C and 1.01325 bar absolute), and with a measuring range of 100 to 10000 L/min, was used to measure and display the air volumetric flow rate at the turbine inlet. The mass flow rate through the turbine was then calculated from the product of the measured volumetric flow rate and the air density, calculated at the standard conditions (Festo, 2012*b*).

The mode of measurement of the flow sensor is by means of a thermal procedure, where the volumetric flow rate through the sensor is determined from the amount of heat drawn from the heated inner wall surface of the sensor, by the medium flowing through its bore.

The flow sensor requires an input DC voltage of 24 V, which is supplied by a Metronix 545B [serial number 273476] regulated DC power supply. The flow sensor also has an *onboard* LCD display that indicates the volumetric flow rate in real time, therefore no data logger is required for this purpose.

### *Pressure sensors*

Two Festo SDE3 pressure sensors [serial numbers P8XMV8 and P8XXTF], with a measuring range of 0 to 10 bar, were used to measure the gauge pressure at the turbine inlet (sensor P8XMV8) and outlet (sensor P8XXTF). The pressure sensors have an *onboard* LCD display that indicates the gauge pressure in real time and they also require an input DC voltage of 24 V, which is supplied by the Metronix 545B regulated DC power supply. They were statically calibrated against a 2500 kPa Wika pressure gauge [serial number 720223 and calibrated on 06/06/2011] and the calibration procedure is added in Appendix A.

The atmospheric pressure was measured using a Thies Clima [model number 3.1150.17.000 and serial number 0793010] mercury station barometer, with a measuring range of 800 – 1100 hPa and a rated accuracy of ± 0.3 hPa. The mercury barometer is not part of the test bench, as it is one of the measuring instruments installed in the Heat Transfer laboratory, Department of Mechanical and Mechatronic Engineering, Stellenbosch University. It was therefore read from its position – a floor lower than that on which the air test bench was set up.

### *Temperature sensors*

The temperature and the turbine inlet and outlet was not controlled, but simply measured, using T-type thermocouples. This type of thermocouples consist

of a positive copper wire and a negative constantan wire and are ideal for low temperature applications, with an applicable measuring range of 0 to 400 °C (Beckwith *et al.*, 1993). Logging of the thermocouple data was done using an Hewlett-Packard 34970A [serial number US37008090] data acquisition system, with the thermocouples occupying 5 channels of the 20 channels available on the Agilent 34901A [serial number MY41114237] 20 channel multiplexer located in the first slot of the data logger. The data logger was connected to a Lenovo B560 laptop using a USB connection cable and it was configured, and the thermocouple data recorded using Agilent Benchlink Data Logger 3 software installed on the laptop.

The thermocouples were calibrated against an Isotech platinum resistance thermometer [model number 935-14-72, serial number 191069 and calibrated on 4/02/2013], using a Fluke 9142 Field Metrology Well thermocouple calibrator [serial number B29291]. The calibration procedure is added in Appendix A.

### *Tachometer*

An Ono Sokki HT 341 contact-type digital hand tachometer, with a measuring range of 15 to 20000 rpm and an accuracy of ± 1 rpm, for a measuring range of 15 to 14999 rpm and ± 2 rpm, for speeds greater than that, was used to measure the generator shaft rotation speed, also equal to that of the magnetically coupled turbine shaft. This type of tachometer uses a pickup tip in contact with the rotating member being measured and requires an input voltage of 4.5 V, supplied by three 1.5 V AA size batteries. It also has an *onboard* LCD display that indicates the rpm in real time.

### *Multimeters*

Two Iso-tech IDM 103N digital multimeters were provided in the set-up; one connected in line with the electric load, to measure the current being drawn from the generator by the electric load, and the other connected across the terminals of the DC generator, to measure the terminal voltage output from the DC generator. These multimeters each requires an input voltage of 3 V, supplied by two 1.5 V alkaline batteries and also have an *onboard* LCD display that indicates the parameter (current or voltage) being measured in real time. The multimeters have a rated accuracy of ±(0.25% + 2 number of digits) for the DC voltage measurement and ±(1.2% + 3 number of digits) for the DC current measurement (Iso-tech, 2012).

### *Spring loaded scale*

A spring loaded scale, with a vertical analog readout graduated from 0 to 2.25, at a resolution of 0.05, was fitted in the test bench, as part of the dynamometer set-up. Its scale was calibrated against brass metric weights of

known weight and a correlation between the weight exerted onto the scale by the added weights and the resulting vertical displacement of the spring was obtained (Equation (A.3)). In the dynamometer set-up, the spring loaded scale was hooked to a torque arm, which was in turn clamped to the generator. The scale was used to measure the vertical displacement of the spring, for each subsequent loading of the turbine. Using Equation (A.3), the measured displacement was then converted to the weight exerted by the torque arm onto the scale. The torque exerted by the turbine shaft onto the coupled generator shaft was calculated from the product of the calculated weight and the torque arm length $l$ (see Figure 3.4b). The calibration procedure for the spring loaded scale is added in Appendix A.

The rest of the apparatus used in the test bench included: Pipe plumbing fittings, such as two 1-BSP female thread ball valves; one fitted as the main shut-off valve for the air supply line and another fitted as flow control valve 1, just downstream of the pressure regulator. Also, a $1^1/_2$-BSP female thread ball valve was fitted as flow control valve 2, downstream of the turbine outlet and a 1-BSP female thread brass pipe union was fitted just downstream of the main shut-off valve, to allow easy connection or disconnection of the whole set-up from the main air supply line, in times of component replacement. The test bench set-up also included four 1-BSP male thread nipples; the first nipple connected the inlet end of the main shut-off valve to an elbow on the air supply line, the second nipple connected the outlet end of the main shut-off valve to the inlet end of the union, the third nipple connected the outlet end of the union to the inlet of the pressure regulator and the final nipple connected the outlet of the pressure regulator to the inlet end of flow control valve 1.

The flow sensor was installed downstream of flow control valve 1, with its G$1^1/_2$ female thread inlet port connected to the 1-BSP female thread outlet end of flow control valve 1, using an aluminium alloy AL 6082 flow stabilising pipe of 25.0 mm ID, 47.8 mm OD and length 250.0 mm. This pipe had 1-BSP male thread on one end and G$1^1/_2$ male thread on the other, with the former screwed to the outlet end of flow control valve 1, while the latter was screwed to the inlet port of the flow sensor. The choice of pipe ID was influenced by the flow sensor pneumatic installation requirements, that restricted the flow sensor supply ID to a minimum of 20 mm (Festo, 2012*b*), while the length of the pipe was made ten times the pipe ID, in order to allow for fully developed flow, for more accurate flow measurements.

The turbine was installed downstream of the flow sensor in the test bench, with the turbine's $^3/_8$-18 NPT female thread inlet connected to the flow sensor's G$1^1/_2$ female thread outlet. The connection between the two was achieved through, first reducing the flow sensor's G$1^1/_2$ female thread outlet to $^1/_2$-BSP female thread, using $1^1/_2 \times$ 1-BSP and $1 \times {}^1/_2$-BSP thread galvanised steel reducing bushes, and then using two Festo QS connectors – a QS-$^1/_2$-16 push-in fitting screwed to the reduced flow sensor outlet and a QS-$^3/_8$-16 push-in fitting screwed to the turbine inlet – and Festo PUN-16$\times$2.5-BL flexible plastic tubing

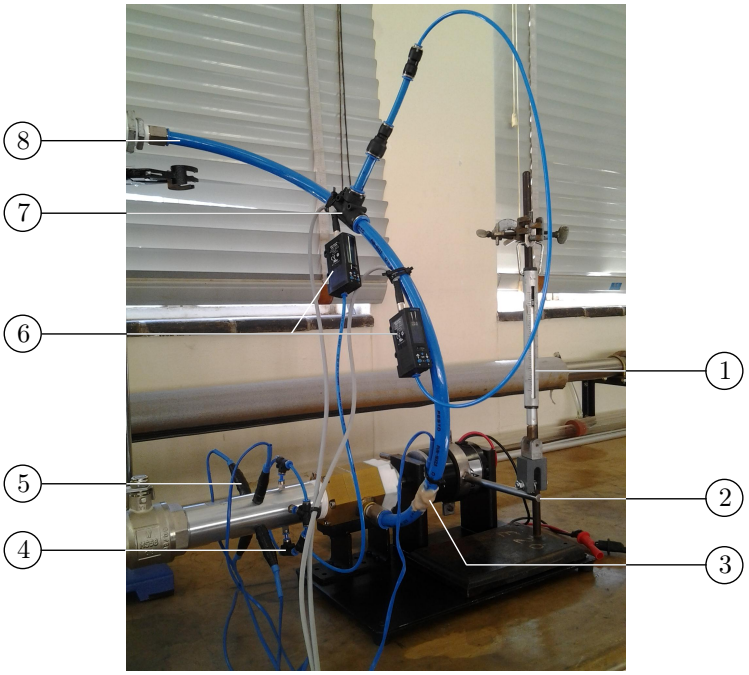


**Figure 3.5:** Location of pressure and temperature measurement points at the turbine inlet and outlet and the dynamometer set-up; 1. Spring loaded scale, 2. Torque arm, 3. Temperature measurement point at the turbine inlet, 4. Pressure measurement point at the turbine outlet, 5. Temperature measurement point at the turbine outlet, 6. Festo SDE3 pressure sensors, 7. Pressure measurement point at the turbine inlet, 8. Festo flexible plastic tubing

of 16 mm OD and 11 mm ID. The use of flexible tubing prevented transmission of vibration from the rotating turbine shaft to the fixed piping and also made the coupling and mounting of the turbine-generator much easier. The turbine inlet static pressure measurement point and temperature measurement point were provided for on the flexible plastic tubing (see Figure 3.5), with the latter downstream of the former, and with both measurement points located in close proximity of the turbine inlet – to ensure a more accurate representation of the turbine inlet conditions was obtained – as suggested by Brun and Nored (2006), and consistent with the recommendations of ASME PTC 10 (1997). This same standard also recommends the use of at least four pressure taps and four temperature taps at pressure and temperature measurement points, but due to the small size of tubing (16 mm OD and 11 mm ID) used, this was not feasible. The static pressure tap was created using Festo QST-16-12, QS-12-8 and QS-8-4 reducing push-in connectors and Festo PUN-12 $\times$ 2-BL, PUN-8 $\times$ 1.5-BL and PUN-4 $\times$ 0.75-BL Festo flexible plastic tubing. The reduction from 16 to 4 mm OD plastic tubing was influenced by the 4 mm OD pneumatic connection of the Festo SDE3 pressure sensor. The temperature measurement point was created by piecing a hole into the plastic tubing and horizontally pushing the T-type thermocouple probe through it, orienting it parallel to and

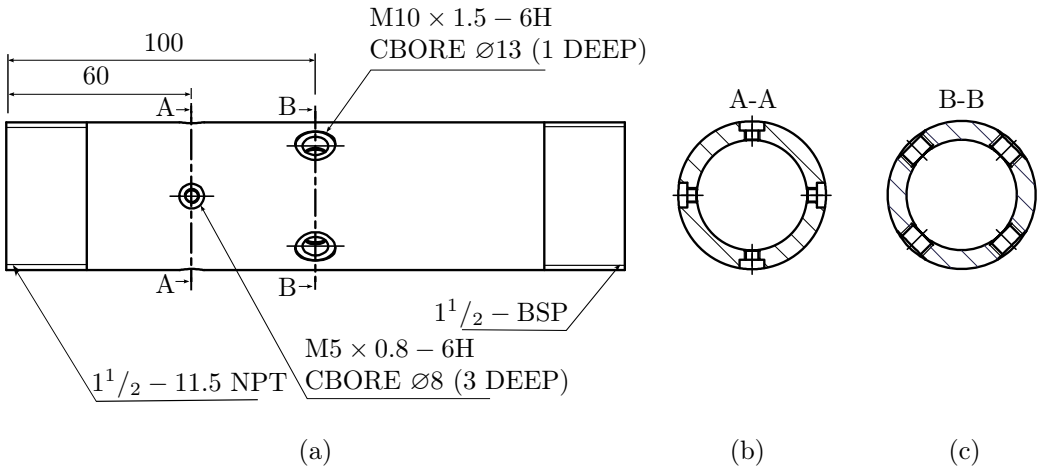


**Figure 3.6:** Location of pressure and temperature measurement points on the turbine outlet pipe; Turbine outlet pipe front view (a), circumferential position of pressure measurement points at section A-A (b), circumferential position of temperature measurement points at section B-B (c)

in the direction of the air flow, so as to measure static temperature. The hole was sealed off and the thermocouple glued in place using epoxy resin adhesive.

For the turbine outlet pipe, an aluminium alloy AL 6082 pipe of 35.8 mm ID, 47.8 mm OD and length 250.0 mm was used. This pipe had $1^1/_2$-11.5 NPT male thread on one end and $1^1/_2$-BSP male thread on the other, to allow screwing onto the turbine outlet and flow control valve 2, respectively. Four static pressure measurement points and four temperature measurement points were provided for on this turbine outlet pipe, with the latter downstream of the former, and with all measurement points located in close proximity of the turbine outlet and in a different line of sight, as recommended by the ASME PTC 10 standard. The measurement points were located circumferentially around the pipe, with each of the four points spaced 90 ° apart. To achieve the different line of sight, the temperature measurement points were placed 45 ° from the static pressure measurement points, as shown in Figure 3.6. For the static pressure taps, four M5×0.8 holes, with 8 mm diameter counter bores of depth 3 mm, were machined into the turbine outlet pipe. The four static pressure taps were then created using four Festo QSK-M5-4 push-in threaded fittings with sealing rings, five Festo QST-4 push-in T connectors and PUN-4 × 0.75-BL flexible plastic tubing of 4 mm OD. The counter bores on the holes were to allow the push-in threaded fittings flush and be exactly perpendicular with the pipe inner wall surface, on being screwed into the holes, as recommended by the ASME PTC 10 standard, for accurate static pressure measurement. The turbine outlet pressure was then determined by taking the average reading of the four static pressure taps, using the Festo SDE3 pressure sensor. For the temperature measurement taps, four M10 × 1.5 holes, with 13 mm diameter counter bores of depth 1 mm, were machined into the turbine

outlet pipe. The four temperature taps were then created by screwing four M10×1.5, 1.6 mm sheath diameter SUPER LOK BRA SCA brass compression fittings into the holes, with the tips of the fittings flushing with the pipe inner wall surface. The four thermocouple probes was then vertically pushed through the four temperature taps, and then bent parallel to and in the direction of the air flow. The portion of the thermocouples and their fittings that were left exposed to the atmosphere were then insulated using black insulation tape. The turbine outlet temperature was then determined by taking the arithmetic mean of the four temperature readings from the thermocouples.

The last apparatus in the test bench set-up was the purposely built dynamometer (see Figures 3.4b and 3.5), set-up to determine the torque exerted by the turbine shaft onto the coupled generator shaft. The turbine shaft power output was then determined from the product of this determined torque and the turbine angular rotation speed. The dynamometer consisted of a vertically held spring loaded scale that was hooked to a 140 mm long stainless steel torque arm. The torque arm was welded onto a clamp and the clamp bolted around the circumference of the generator. The clamp was made of two stainless steel flat plates of 2 mm thickness, 20 mm width and bent to a diameter of 76.2 mm. The clamp was bolted to the generator using two M5 × 15 steel hexagon socket head cap screws, M5 steel nuts and washers.

The as-built experimental air test bench is shown in Figure 3.7.

### 3.2.2 Measured and calculated parameters

In order to determine the turbine performance characteristics discussed in Subsection 2.4.2, some primary measurements of the turbine performance parameters were done, and the turbine performance characteristics were then calculated from these measurements.

To obtain the turbine total to static pressure ratio $P_R$, as defined by Equation (2.5), the turbine inlet and outlet gauge pressures and temperatures were measured. The measured gauge pressures at the turbine inlet and outlet were then corrected using Equations (A.1) and (A.2), while the measured turbine inlet and outlet temperatures were corrected using Equations (A.4) and (A.6) to (A.9), with the corrected temperature at the turbine inlet given by Equation (A.5), while that at the turbine outlet was given by Equation (A.10). The correction equations were obtained from the calibration of the pressure and temperature sensors (see Appendix A). The temperatures and pressures referred to hereinafter, are therefore the corrected temperatures and pressures.

The turbine inlet and outlet gauge pressures were then converted to absolute pressures using

$$P_{abs} = P_g + P_{atm} \tag{3.1}$$

Where $P_{abs}$ was the absolute pressure, $P_g$ was the gauge pressure and $P_{atm}$ was the measured atmospheric pressure. The stagnation pressure at the turbine

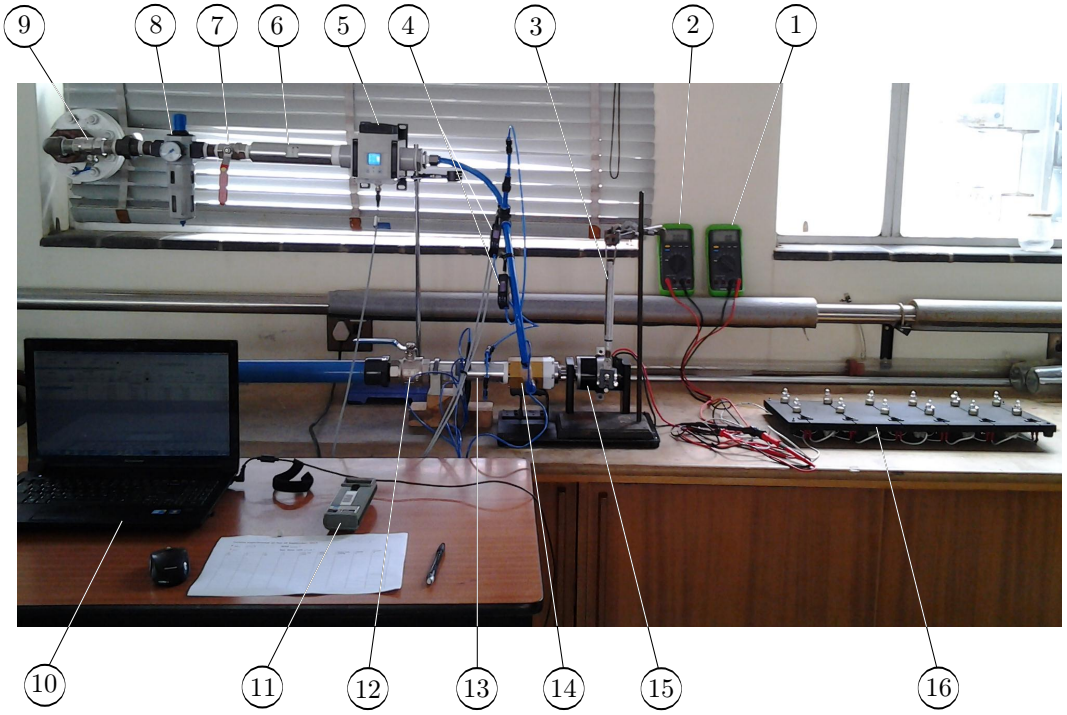


**Figure 3.7:** Experimental air test bench; 1. Voltmeter, 2. Ammeter, 3. Spring loaded scale, 4. Pressure sensors, 5. Flow sensor, 6. Flow stabilising pipe, 7. Flow control valve 1, 8. Pressure regulator, 9. Main shut-off valve, 10. Data logging system, 11. Tachometer, 12. Flow control valve 2, 13. Turbine outlet pipe, 14. Turbine, 15. Generator, 16. Electric load

inlet $P_{01}$ was then calculated using the isentropic relation between pressure and temperature ratios for an ideal gas, as given by

$$P_{01} = P_{1,abs}\left(\frac{T_{01}}{T_1}\right)^{\gamma/(\gamma-1)} \tag{3.2}$$

Where $P_{1,abs}$ was the calculated turbine inlet absolute air pressure and $T_1$ was the turbine inlet temperature. $T_{01}$ was the turbine inlet stagnation temperature, and was given by

$$T_{01} = T_1 + \frac{{V_1}^2}{2c_p} \tag{3.3}$$

Where $V_1$ was the air velocity at the turbine inlet, calculated from the one-dimensional, steady flow mass balance expression (Equation (2.1))

$$V_1 = \frac{\dot{m}}{\rho_1 \pi {d_1}^2/4} \tag{3.4}$$

Where $d_1$ was the ID of the flexible plastic tubing connected between the flow sensor outlet and the turbine inlet, $\dot{m}$ was the mass flow rate through the

turbine, calculated from the product of the measured air volumetric flow rate $\dot{V}$ and the calculated air density at standard conditions $\rho_{stand.conds}$, as given by

$$\dot{m} = \dot{V}\rho_{stand.conds} \tag{3.5}$$

with $\rho_{stand.conds}$ calculated from the ideal gas equation of state, at standard absolute pressure and temperature conditions

$$\rho_{stand.conds} = \frac{P_{stand.conds}}{RT_{stand.conds}} \tag{3.6}$$

The air density at the turbine inlet $\rho_1$ in Equation 3.4 was similarly calculated from the ideal gas equation of state, at the turbine inlet absolute pressure and temperature conditions

$$\rho_1 = \frac{P_{1,abs}}{RT_1} \tag{3.7}$$

The turbine total to static efficiency $\eta_{t-s}$, as defined by Equation (2.6), was calculated from temperature and pressure ratios, which were in turn calculated from the measured temperatures and pressures at the turbine inlet and outlet. The turbine outlet stagnation temperature term $T_{03}$ in Equation (2.6) was calculated from

$$T_{03} = T_3 + \frac{{V_3}^2}{2c_p} \tag{3.8}$$

Where $T_3$ was the turbine outlet temperature and $V_3$ was the air velocity at the turbine outlet, calculated from the one-dimensional, steady flow mass balance expression (Equation (2.1))

$$V_3 = \frac{\dot{m}}{\rho_3 \pi {d_3}^2/4} \tag{3.9}$$

Where $d_3$ was the ID of the turbine outlet pipe and $\rho_3$ was the air density at the turbine outlet, calculated from the ideal gas equation of state, at the turbine outlet absolute pressure and temperature conditions

$$\rho_3 = \frac{P_{3,abs}}{RT_3} \tag{3.10}$$

The non-dimensional mass flow rate $\theta$, as defined by Equation (2.7), was calculated from: the mass flow rate through the turbine – calculated from the measured volumetric flow rate using Equation (3.5), the turbine inlet stagnation temperature – calculated from the measured turbine inlet temperature using Equation (3.3) and the turbine inlet stagnation pressure – calculated from the measured turbine inlet gauge pressure and temperature using Equation (3.2).

The final turbine performance characteristic was the shaft power developed by the turbine. This was primarily determined from the measured generator

shaft rotation speed $N$ (also equal to that of the magnetically coupled and synchronously rotating turbine shaft) and the measured displacement on the spring loaded scale $x$. This shaft power was calculated from

$$\dot{W}_{shaft} = \omega T \tag{3.11}$$

Where $\omega$ was the turbine shaft angular rotation speed, determined from the measured rotation speed of the turbine shaft, and given by

$$\omega = \frac{2\pi(N)}{60} \tag{3.12}$$

and $T$ was the torque exerted by the turbine shaft onto the coupled generator shaft and was calculated from the product of the weight determined from the measured vertical displacement on the spring loaded scale (using Equation (A.3)) and the length of the torque arm $l$ (see Figure 3.4b), as given by the expression

$$T = Weight \times l \tag{3.13}$$

### 3.2.3 Safety procedure

The air test bench was set-up in the Heat Transfer Laboratory, room 264, Department of Mechanical and Mechatronic Engineering, Stellenbosch University. The set-up and experimental work therefore followed laboratory safety procedures outlined by the Department of Mechanical and Mechatronic Engineering, Stellenbosch University (2012).

The potential risks associated with the test bench set-up and the experimental work, relating to the health and safety of the experimenter, the people in close proximity of the set-up and the equipment in the set-up itself were identified and steps that could minimise or eliminate these risks were taken.

The risks involved and the mitigation steps taken included:

- Electric shock as a result of the experimenter coming into contact with live wires on the electric load. This was addressed through using proper and secure wire connectors like terminal block screw wire connectors and receptacle crimp terminals. Additional insulation was provided by using black insulation tape whenever necessary.

- Injuries to the experimenter and the people in close proximity of the set-up, as a result of slipping off of rotating parts in the set-up, in particular the rotating magnetic couplers. This risk was addressed through ensuring that the couplers were tightly fastened to the turbine and generator shafts using hexagon socket grub screws. In addition, the turbine coupler was fully enclosed by a plastic back block. Safety goggles were also worn by the experimenter at all times during the experiments, to protect against eye injuries.

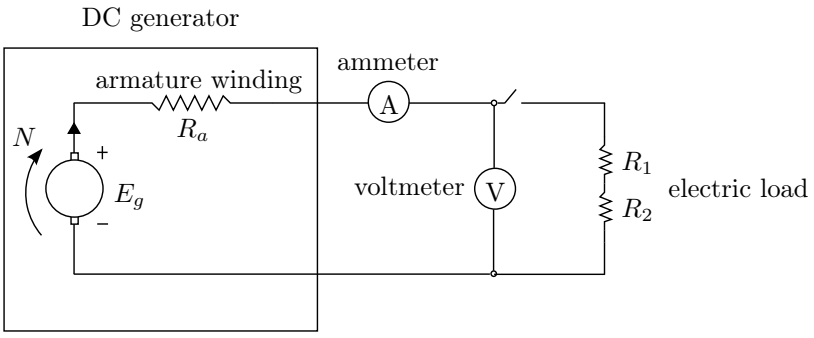


**Figure 3.8:** DC generator model

- Failure of test bench apparatus like the plastic tubing and fittings/connectors, as a result of the relatively high pressure (up to 10 bar) of the compressed air supplied to the test bench. This was addressed by installing both a main shut-off valve and a pressure regulator in the pressure line – to isolate the whole set-up from the main air supply, for the former and to regulate the pressure of the supplied air, for the latter. The apparatus fitted in the test bench is also specifically suited for air applications at that pressure.

- Hearing loss as a result of over exposure to the ear-piercing high pitched sound of the turbine, when in operation. This was addressed by firstly, putting a notice at the main entrance of the laboratory, warning of the nature of the experiment to be carried out, secondly, by screening off the laboratory during experiments and lastly, by using ear muffs and ear plugs during experiments and providing the same to the people working in close proximity of the set-up.

### 3.2.4 Experimental procedure

The turbine internal and external losses, including: skin friction losses, blade loading losses, blade tip leakage losses, disk friction losses and bearing friction losses, all increase as the squares of the velocities involved. As these losses could not be determined experimentally, it was important that they remained constant throughout the experiments, in order to obtain an accurate representation of the turbine performance. This, therefore required that the turbine be operated at a constant rotation speed, consequently implying a constant speed of rotation for the coupled generator; the choice of speed being that at which the generator would generate a constant induced voltage of 24 V DC, in order to meet the electric load connected across its terminals.

Figure 3.8 is a schematic illustration of a DC generator model, with the generator physical boundaries represented by the square. The generator is connected to an external circuit consisting of an ammeter connected in-line and both a voltmeter and an electric load connected across the generator ter-

minals. The voltage induced in the armature of the generator $E_g$ is directly proportional to the speed of relative motion between the armature and the generator's magnetic field, as can be deduced from Faraday's Electromagnetic induction expression (Equation (3.14)), for voltage induced in an armature rotating in and cutting a magnetic field

$$E_g = PZ\phi N/(60A) \tag{3.14}$$

Where $P$ is the number of poles, $Z$ is the number of armature conductors arranged in $A$ number of parallel paths, $\phi$ is the magnetic flux per pole and $N$ is the rotation speed of the armature. Of all the five independent terms in Equation (3.14), only $N$ can be experimentally varied. The other four terms remain constants, owing to the fact that they form part of or are a result of the physical make up of the generator. Therefore, keeping the rotation speed of the generator constant implies a constant induced voltage in the generator's armature. Furthermore, at no load, the voltage drop across the armature winding is zero, and the induced voltage in the armature is equal to the measured terminal voltage, as can be seen from

$$V_t = E_g - IR_a \tag{3.15}$$

Where $V_t$ is the measured terminal voltage, $E_g$ is the induced voltage in the armature, $I$ is the load and $R_a$ is the armature winding resistance. The no-load condition of the generator can therefore be used to determine the rotation speed at which a generator generates a certain induced voltage. Keeping the no-load speed of the generator constant also ensures that both the induced voltage and the mechanical losses of the generator, for example, the bearing friction losses, remain constant. To determine the turbine rotation speed, it was therefore necessary to determine/verify the rated generator no-load speed, for a measured terminal voltage of 24 V DC. The turbine was then operated at the determined generator no-load speed, and the power dissipated in the electric load $P_{elec}$, on loading the turbine, was calculated from the product of the measured current $I$ and the constant internal induced voltage $E_g$, as given by

$$P_{elec} = IE_g \tag{3.16}$$

The power calculated using Equation (3.16) was used for indicative purposes during the determination of the shaft power developed by the turbine, as the power dissipated in the electric load will be less than the mechanical work done by the turbine coupled to the generator, owing to the losses in the generator.

Before performing a test run, some initial checks had to be done. These checks included:

- Check that all pressure piping, tubing, fittings and connections are firmly connected and secure.

- Check that all electrical connections are proper and secure, and that all live wires are fully insulated.
- Check that all rotating parts are tightly fastened and enclosed by casings, where applicable.
- Check that the main shut-off valve, pressure regulator knob and flow control valve 1 (see Figures 3.4 and 3.7) are in a 'closed' position and that flow control valve 2 is in an 'open' position.
- Check that all switches in the electric load are in an 'off' position.
- Check that all instrumentation in the test bench is properly functioning and that they all indicate zero readings.
- Check that all personal protection equipment required for the experiment is being worn.

On satisfactory completion of the checks, three test runs were then performed for each turbine rotor, with all the three test runs for each rotor being performed in succession, and on the same day, to minimise variation in the turbine test conditions. This was important for consistency in the turbine test conditions and also would allow for statistical error analysis of the measured turbine test data. The procedure followed for each test run was as follows:

- Measure and record the atmospheric pressure $P_{atm}$. In addition, record the zero reading of the spring loaded scale $x_0$. The atmospheric pressure measurement was a once-off at this stage and applied to all the three test runs for each rotor.
- Open the main shut-off valve.
- Turn the pressure regulator knob until the maximum air pressure available in the supply line is attained.
- Gradually open flow control valve 1 (see Figures 3.4 and 3.7) and concurrently manipulate it and the pressure regulator knob, in order to adjust the air flow through the turbine. Monitor the volumetric flow rate, voltage output and generator rotation speed and only stop adjusting the flow through the turbine when a terminal voltage of 24 V is indicated on the voltmeter.
- Leave the set-up to stabilise for a duration of 30 minutes.
- After the stabilisation period, monitor the voltage output and adjust the flow accordingly, until the required terminal voltage of 24 V is attained again.

- Measure and record the generator no-load speed. In addition, record the spring loaded scale displacement, terminal voltage indicated by the voltmeter, volumetric flow rate and the pressure and temperature at the turbine inlet and outlet and take these as the no-load conditions of the turbine.

- load the turbine by switching on the first column of lamps on the left of the electric load. Then adjust the flow through the turbine by manipulating flow control valve 1 and the pressure regulator knob and monitor the generator speed until the no load speed is attained.

- On attaining the no-load speed, stop adjusting the flow through the turbine and allow the system to stabilise for 5 minutes. After the stabilisation period, monitor the generator speed and adjust the flow accordingly, until the no-load speed is attained.

- Record the spring loaded scale reading, current drawn from the generator by the load, volumetric flow rate and the air pressure and temperature at the turbine inlet and outlet.

- From the left to the right of the electric load, sequentially add load to the turbine by switching on a column of two lamps at a time, and repeat the last three steps.

- At the end of a test run, turn off the air supply by closing the main shut-off valve, pressure regulator knob and flow control valve 1, in that order.

### 3.2.5 Measurement uncertainty analysis

Measurement uncertainty or error analysis can be used to determine the accuracy and quality of a set of measurements. The error of a measurement is defined as the difference between the measured value of a physical quantity and the actual or true value of the physical quantity. Beckwith *et al.* (1993) define two general classes of errors: bias errors and precision errors. Bias errors, also known as systematic errors, are defined as those errors that occur in a consistent way each time a measurement is made. These errors can not be treated using statistical techniques, given their consistent nature and the fact that they don't show a distribution. Precision errors, on the other hand, can be treated using statistical analysis, if enough measurements are taken, and they will generally cluster about a central value, only extending over a short interval surrounding that central value. They are also known as random errors and their values change with each successive measurement.

Minimal measurement error is a primary requirement in the design and executing of experiments, and according to Beckwith *et al.*, the initial step

in bounding a measurement's error or uncertainty is to identify its possible causes. Potential causes of bias errors include: improper calibration of instrumentation used for the measurements, consistent human errors when taking measurements, use of defective instrumentation, system resolution limitations and the influence of the measuring procedure on the system under test. Calibration procedures seek to identify and eliminate bias errors by comparing the instrumentation scale readings to that of a standard, but they do not eliminate the bias errors entirely, owing to the fact that the standards themselves have uncertainties, even though very small ones. Potential causes of precision errors include: external disturbances to the measuring system, including fluctuating environmental conditions and mechanical vibrations, inconsistent reading of the measurement instruments by the experimenter, poorly controlled processes in the measuring system, insufficient measuring system sensitivity and drift of an instrument's calibration over time. In general, measurement errors are inherent features of the performance of the instrumentation used to take the measurements and the measurement procedures themselves.

The performance rating of the instrumentation used to take measurements during the experimental work, and the potential causes of measurement errors in the measurements taken is discussed in turn, as follows.

***Pressure measurement uncertainty***

The pressure at the turbine inlet and outlet was measured using two Festo SDE3 sensors of rated full scale (FS) accuracy and reproducibility of $\pm 3\%$ and $\pm 0.3\%$ (Festo, 2012*a*), while the atmospheric pressure was measured using a Thies Clima mercury station barometer of rated accuracy of $\pm$ 0.3 hPa, and stationed on a floor lower than that on which the test bench was set up. The Festo pressure sensors were calibrated against a Wika pressure gauge, in order to identify and eliminate their bias error (see Appendix A).

The stationing of the mercury barometer on a different floor to that on which the test bench was set up, and the use of a once-off measured atmospheric pressure value throughout the test runs of each rotor, despite the possibility of changing weather conditions, could have contributed to a bias error in the calculation of the absolute turbine inlet and outlet pressures (Equation (3.1)), as the atmospheric pressure measurement is both dependent on changes in elevation and weather conditions (Cengel and Cimbala, 2010). On the other hand, rounding-off and parallax errors in the reading of the mercury barometer scale could have contributed to a precision error in the atmospheric pressure reading, in turn, contributing to a precision error in the calculated absolute pressure. In addition, the use of only one static pressure measurement tap, rather than the four recommended by the ASME PTC 10 standard, and the use of varying length to diameter ratio of the tubing and static tapping at the turbine inlet pressure tap – it was impractical to keep a constant length to diameter ratio for the different ID Festo flexible plastic tubing used to create

the static pressure tap at the turbine inlet – could have contributed to a precision error in the pressure measurement reading taken at the turbine inlet. According to Brun and Nored (2006), the use of less than four pressure taps, in addition to incorrect installation and location of pressure probes are the main sources of pressure measurement errors.

### *Temperature measurement uncertainty*

The temperature at the turbine inlet and outlet was measured using five T-type thermocouples of a rated probe accuracy of ± 0.5 to 1 °C (Agilent technologies, Inc., 2006). Bias error in the temperature measurements could have been as a result of a manufacturing defect in the thermocouples. In addition, the presence of a thermocouple probe in the very narrow (16 mm OD and 11 mm ID) Festo flexible plastic tubing at the turbine inlet could also have introduced a bias error in the temperature measurement taken at that point, as the probe would be interfering with the flow.

On the other hand, the use of one temperature measurement tap at the turbine inlet, as restricted by the size of the Festo flexible plastic tubing used at the turbine inlet, rather than the four temperature measurement taps recommended by the ASME PTC 10 standard, could have contributed to a precision error in the temperature measurement at the turbine inlet.

The thermocouples were calibrated against an Isotech Platinum resistance thermometer, in order to identify and eliminate the bias error in their measurements, and a measurement uncertainty bound of ± 0.15 °C was estimated from the calibration (see Figure A.6f).

### *Volumetric flow rate measurement uncertainty*

The air volumetric flow rate at the turbine inlet was measured using a Festo SFAM-90 series flow sensor of a rated accuracy and reproducibility of ± (3% o.m.v (on machine verification) + 0.3% FS) and ± (0.8% o.m.v + 0.2% FS) (Festo, 2012*b*). The mass flow rate through the turbine was calculated from the product of the measured volumetric flow rate and the air density calculated at standard conditions ( Equation (3.5)). Any bias and precision errors present in the measured volumetric flow rate were therefore carried over to the calculated value of the mass flow rate. The lack of a standard – with a similar operating range of 100 to 10000 L/min – to calibrate the flow sensor against meant that the flow sensor could not be calibrated in-house. This could have been a potential source of bias error in the flow sensor readings taken. On the other hand, inconsistent estimation of the flow sensor readings, as a result of the unstable nature of the air supply, could have been a potential source of precision error in the flow measurement reading.

***Rotation speed measurement uncertainty***

The turbine rotation speed was measured using an Ono Sokki HT 341 contact-type digital hand tachometer of a rated accuracy of $\pm$ 1 rpm, for the turbine's operating rpm range of 15 to 14999 rpm. The angular rotation speed of the turbine was calculated from this measured rotation speed, using Equation (3.12). Since there was no standard available to calibrate the tachometer against, any bias error present in the measured rotation speed would be as a result of calibration uncertainty, and would be carried over to the calculated angular rotation speed. On the other hand, precision error in the speed measurement could probably be as a result of inconsistent estimation of the tachometer reading.

***Displacement measurement uncertainty***

The scale of the spring loaded scale was calibrated against brass metric weights of known weight. These weights were weighed using a Precisa 40SM-200A [serial number 73464] electronic precision balance, with two weighing ranges: $41 \times 0.01$ mg and $201 \times 0.1$ mg. The bias uncertainty in the weight measurement would therefore be as a result of the calibration uncertainty of the precision balance. On the other hand, precision errors in the displacement measurement could be as a result of reading error in the spring loaded scale measurement, and probably, hysteresis, friction or backlash in the spring mechanism of the scale. The torque exerted by the turbine shaft onto the coupled generator shaft was determined from the spring loaded scale displacement measurement, using Equations (A.3) and (3.13), and therefore any bias and precision errors present in the displacement measurement were carried over to the calculated torque value.

## 3.3 Turbine rotor design

Following the testing and analysis of the acquired ITmini waste heat turbine, it was decided that a new radial inflow turbine rotor be designed and manufactured, with an emphasis on providing a clear passage for the fluid flow through the rotor. According to Whitfield and Baines (1990), a smooth flow passage for the working fluid flowing through a rotor and low exit kinetic energy improve turbine efficiency. Figure 3.9 shows the acquired ITmini waste heat turbine rotor with fin-like blades, while Figure 3.10 shows the ITmini waste heat turbine rotor fitted inside its turbine casing. The lack of a smooth blade surface and the lack of a hub surface on this rotor was seen to be detrimental to the smooth flow through the rotor and the new rotor design was to address this. In addition, the flow geometry obtained from the new rotor design would be used in the analysis of the operation of a radial inflow turbine (see Subsection 2.4.1).

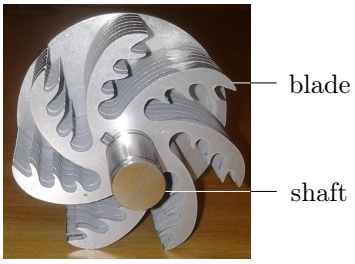


**Figure 3.9:** ITmini turbine rotor

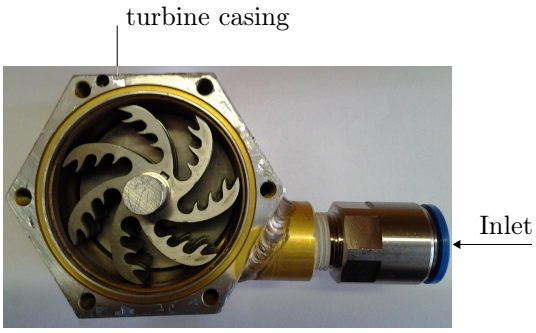


**Figure 3.10:** ITmini turbine rotor fitted inside the turbine casing

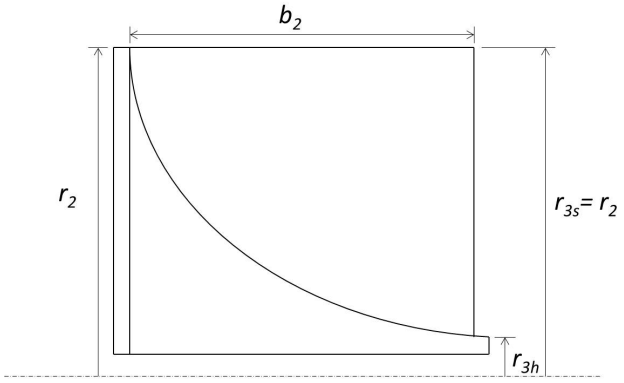


**Figure 3.11:** Typical radial inflow turbine rotor dimensions (adapted from Whitfield and Baines, 1990)

The design procedure for the rotor followed that outlined by Whitfield and Baines, for the design of radial inflow turbines. A design code was then written in MATLAB R2010a, based on this design procedure and following a radial inflow turbine rotor design code outlined by Whitfield and Baines, and the output of the code was provided as input to the CAD 3-dimensional model. The produced CAD model was then exported as a *.stl* file to PowerSHAPE CAD software, post processed and thereafter machined on a HERMLE C40 U 5-axes CNC milling machine at the Rapid Product Development Laboratory, Department of Industrial Engineering, Stellenbosch University.

### 3.3.1 Design procedure

Figure 3.11 shows typical radial inflow turbine rotor dimensions in the meridional plane, where $r_2$ and $b_2$ are the rotor inlet radius and blade tip height and $r_{3h}$ and $r_{3s}$ are the rotor exit hub and shroud radii.

The rotor design follows a non-dimensional design procedure outlined by Whitfield and Baines (1990). In this procedure, the rotor dimensions and the

rotor and fluid velocities are non-dimensionalised by the rotor inlet radius $r_2$ and the inlet stagnation speed of sound $C_{01}$, respectively.

### *Design constraints and preassigned parameters*

The existing turbine casing (shroud) and shaft were maintained (not changed) for the designed rotor. This meant that the rotor geometry had to be constrained by the turbine casing and shaft dimensions.

The back plate thickness was set to 2 mm, rotor blade tip height $b_2$ to 20.5 mm and the axial length $L$ to 21.5 mm, all constrained by the positions of the retaining rings on the shaft (see Figure 3.3).

A blade tip clearance gap value of 0.92 mm was obtained from the following correlation proposed by Zemp *et al.* (2010), and cited by van der Merwe (2012)

$$\frac{t}{b_2} = 4.5\% \tag{3.17}$$

Blade tip clearance gap is the gap between the blades and the turbine casing and allows clearance between the blade tip and the turbine casing when the rotor is rotating.

The rotor inlet radius $r_2$ was set to 24.43 mm, a value obtained from the difference between the turbine casing inner radius and the obtained clearance gap $t$. The rotor inlet radius therefore fixed the values of the rotor inlet blade height to radius ratio $b_2/r_2$ and the axial length to radius ratio $L/r_2$ to 0.84 and 0.88, respectively.

For the rotor exit shroud to inlet blade radius ratio $r_{3s}/r_2$, Balje (1981) and Rohlik (1968) recommend maximum values of 0.78 and 0.7, respectively, while Rodgers and Geiser (1987) employed radius ratios exceeding 0.7 for their gas turbine applications. Since the shroud is cylindrical on the inside, this constrained the rotor exit shroud to inlet blade radius ratio to a value of unity, in order to maintain the blade tip clearance gap. A rotor exit shroud radius of 24.43 mm was also obtained from this radius ratio. A radius ratio of unity gives rise to 'tall' blades, which give an advantage of reduced clearance gap losses but can also lead to significant blockage of flow at the rotor exducer throat.

Whitfield and Baines (1990) also propose an exit hub to shroud radius ratio $r_{3h}/r_{3s}$ of 0.4. An exit hub radius of 9.77 mm was obtained from this ratio.

The relative velocity ratio $W_{3s}/W_2$ was set to a value of 2, as proposed by Rohlik (1968) and cited by Whitfield and Baines (1990). The relative velocity ratio is a measure of the extent of the expansion in the turbine and a value in excess of unity is required, only constrained by the desire to maintain minimum permissible exit relative Mach number.

Finally, the turbine power ratio $S_w$ was set to a value of 0.005, calculated using Equation (2.9), for a turbine shaft power output of 130 W – a value obtained from the initial air tests involving the ITmini turbine, a mass flow

rate of 0.083 kg/s – the maximum expected mass flow rate of a proposed in house organic Rankine cycle waste heat recovery and utilisation system – and an average turbine inlet stagnation temperature of 299.54 K – obtained from the initial air tests involving the ITmini turbine.

### *Optimum number of rotor blades*

According to Whitfield and Baines (1990), there is no definitive method for the determination of the optimum number of rotor blades; Jamieson (1955) and Balje (1981) obtained criteria based on the need to avoid zero blade surface velocity at the rotor inlet, and the subsequent separation of flow that comes with it, while Hiett and Johnson (1963) preferred a criterion based on a compromise between total pressure losses that occur as a result of avoiding flow separation and friction losses that increase with increase in rotor and blade wetted surface areas. For small rotors, the need to avoid blockage at the exducer throat and the need to control friction losses, requires a small number of blades. Whitfield and Baines further note that in practice, a small number of blades is acceptable for small turbines, as this allows a small amount of flow reversal, without adversely affecting the efficiency. Therefore, for this rotor design, the rotor blade number was optimised for a range of 7 to 10 blades, with the blade number offering the best theoretical total to static efficiency at design point selected.

Once the number of blades was determined, the optimum rotor incidence and hence blade inlet angle $\beta_2$ and the absolute inlet flow angle $\alpha_2$ could also be determined. Whitfield and Baines (1990) define an incidence factor $\lambda$, analogous to the compressor slip factor. Equation 3.18, obtained from an analysis done by Stanitz (1952) shows that the optimum rotor incidence depends on the number of rotor blades $Z_B$.

$$\lambda = 1 - \frac{0.63\pi}{Z_B} \tag{3.18}$$

In practice, the highest efficiency is attained, not when the flow at the inlet is exactly matched to the blade (zero incidence), but at some negative incidence, with values ranging from $-20°$ (Rodgers, 1987) to $-40°$ (Rohlik, 1975) quoted in available literature. For the minimum Mach number condition, the inlet absolute flow and blade angle are then obtained from the following correlations given by Whitfield and Baines (1990)

$$\cos^2 \alpha_2 = \frac{0.63\pi}{2Z_B} \tag{3.19}$$

$$\cos \beta_2 = 1 - \frac{0.63\pi}{Z_B} \tag{3.20}$$

***Optimum exit blade angle***

The exit blade angle $\beta_3$ is optimised for minimum relative exit Mach number condition, so as to minimise blade passage losses. Whitfield and Baines (1990) apply a procedure similar to that described for the design of an inducer of a compressor impeller. This procedure seeks an inlet relative flow angle, that achieves the required non-dimensional mass flow rate, for minimum inlet relative Mach number condition. Applying the same procedure, to the design of an exducer of a turbine rotor, for minimum relative exit Mach number condition, obtains an optimum exit blade angle of $-55°$. Whitfield and Baines add that, larger (in magnitude) blade angles, for example $-70°$, cannot be ruled out, on the basis that they lead to a reduction in absolute exit Mach number, which in turn leads to a reduction in the exit kinetic energy loss. On the other hand, angles in the range of 0 to $-50°$ are not an option. For this rotor design, the exit blade angle was therefore optimised for a range of -50 to $-70°$, for minimum relative exit Mach number condition.

### 3.3.2 Design code

A turbine rotor design code, based on the design procedure described in Subsection 3.3.1 and following a radial inflow turbine rotor design code outlined by Whitfield and Baines (1990), was written in MATLAB R2010a. The main input to the code were the rotor performance specifications at the design point, including, the power ratio $S_w$, relative velocity ratio ${}^{W_{3s}}/_{W_2}$, initial rotor total to static efficiency $\eta_{0,t-s}$ of 85% and set stator total to static efficiency $\eta_N$ of 90% – values suggested by Whitfield and Baines (1990). The rest of the code input included the other preassigned design parameters described in Subsection 3.3.1.

The code optimises the number of rotor blades $Z_B$ and the turbine exit blade angle $\beta_3$ and computes the turbine inlet absolute flow angle $\alpha_2$ and blade angle $\beta_2$, the turbine stage pressure, temperature and density ratios and the non-dimensional rotor and fluid velocities. The code also implements empirical loss correlations given by Rodgers (1987) and cited by Whitfield and Baines (1990), in order to calculate the turbine total to static efficiency.

For the termination of the code, two convergence criteria had to be satisfied: the first criterion being that, the difference between the calculated turbine total to static efficiency $\eta_{calc,t-s}$ and that actually used in each iteration $\eta_{i,t-s}$ could not exceed 1% , while the second criterion was that, the blade tip speed to spouting velocity ratio ${}^{U_2}/_{V_0}$ could not exceed the optimum efficiency value of 0.707, a value obtained from an analysis done by Rodgers and Geiser (1987).

The rotor design code flow chart is shown in Figure 3.12 while the MATLAB compiled rotor design code is added in Appendix C. The main output from the design code is shown in Table 3.1.

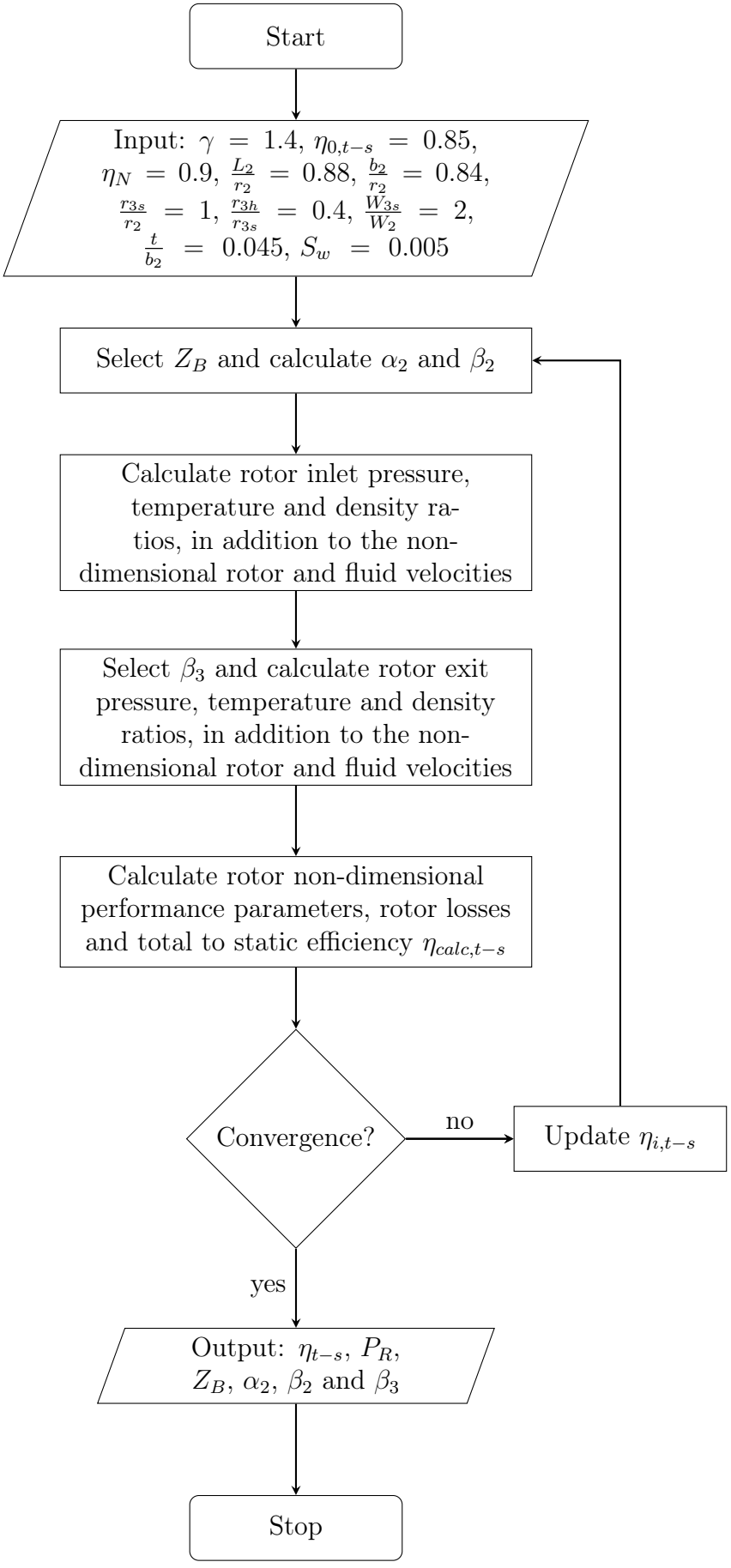


**Figure 3.12:** Rotor design code flow chart

**Table 3.1:** Design point performance and rotor geometry parameters

| Parameter | Value |
|---|---|
| $\eta_{t-s}$ | 17.7% |
| $P_R$ | 1.1 |
| $Z_B$ | 10 |
| $\alpha_2$ | 72° |
| $\beta_2$ | −37° |
| $\beta_3$ | −55° |

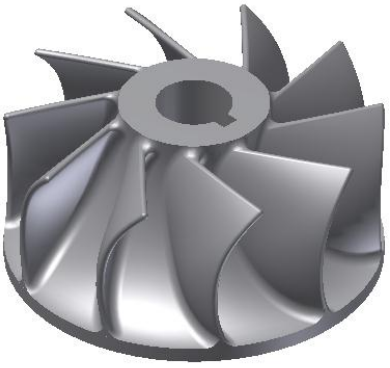

**Figure 3.13:** Rotor CAD model (Autodesk Inventor Professional 2011)

### 3.3.3 CAD model

To be able to manufacture the rotor, a 3-dimensional CAD model of the rotor had to first be created (see Figure 3.13). This was done in Autodesk Inventor Professional 2011-STUDENT VERSION software, with the rotor geometry parameters output from the design code provided as input to the CAD model.

The main features of the CAD model were the hub surface, shroud and blades. The shroud was restricted by the cylindrical shape of the turbine casing and the need to maintain the blade tip clearance gap.

The two remaining features of the CAD model were obtained as follows:

#### *Hub*

Formation of the the hub surface required that a hub contour in the meridional plane first be created. This was achieved using an approach taken by van der Merwe (2012).

The hub contour was defined by a third-order Bezier polynomial curve, with four control points, $h_2$, $h_{B2}$, $h_3$ and $h_{B3}$, where $h_2$ and $h_3$ were the endpoints of the hub contour (see Figure 3.14). Each of the control points was defined by $r$ and $z$-coordinates in the meridional plane. Point $h_2$ at the leading edge had its $r$-coordinate set to the rotor inlet radius $r_2$ while its $z$-coordinate was

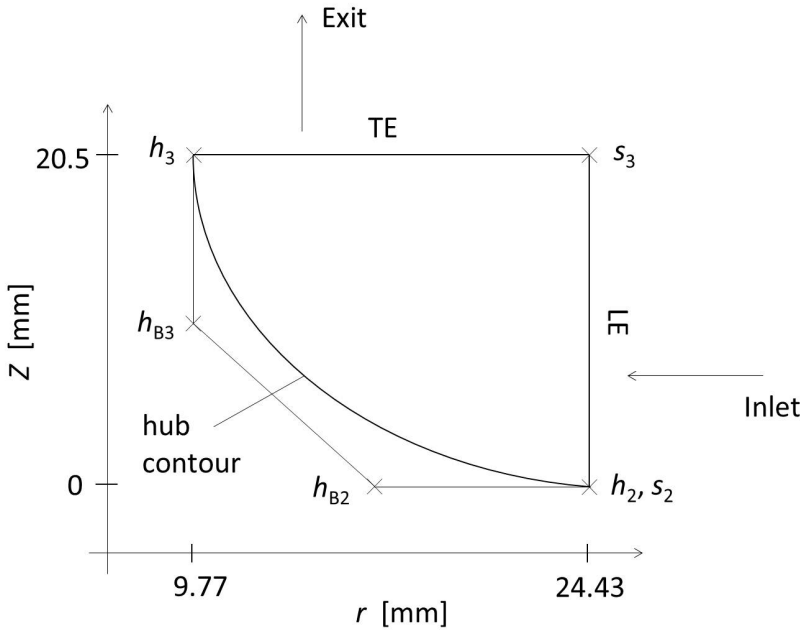


**Figure 3.14:** Meridional view of hub and shroud contour, with Bezier curve control points (adapted from van der Merwe, 2012)

set to zero. The corresponding point on the shroud contour $s_2$ was constrained with the same $r$ and $z$-coordinates. Point $h_3$ at the trailing edge had its $r$-coordinate set to the rotor exit hub radius $r_{3h}$ while its $z$-coordinate was set to the inlet blade height. The corresponding point on the shroud contour $s_3$ had the same $z$-coordinate while its $r$-coordinate was set to the rotor inlet radius, owing to the need to maintain the clearance gap. The $z$-coordinate of point $h_{B2}$ was set to zero while its $r$-coordinate was given by

$$r = \frac{r_2 - r_{3h}}{2} + r_{3h} \tag{3.21}$$

The $r$-coordinate of point $h_{B3}$ was set to the rotor exit hub radius while its $z$-coordinate was given by

$$z = \frac{b_2}{2} \tag{3.22}$$

Forrest (1972) gives the expression for a third-order Bezier polynomial curve as

$$\begin{aligned} p\left(u_m\right) = {} & \left(1 - u_m\right)^3 P_0 + 3u_m \left(1 - u_m\right)^2 P_1 \\ & + 3{u_m}^2 \left(1 - u_m\right) P_2 + {u_m}^3 P_3 \end{aligned} \tag{3.23}$$

where $P_0$, $P_1$, $P_2$ and $P_3$ are the four control points in the order $h_2$, $h_{B2}$, $h_{B3}$ and $h_3$ and $p(u_m)$ is the vector location of any point on the curve. $u_m$ is the non-dimensionalised meridional length, and varies from 0 at the leading edge to 1 at the trailing edge, along the length of the curve.

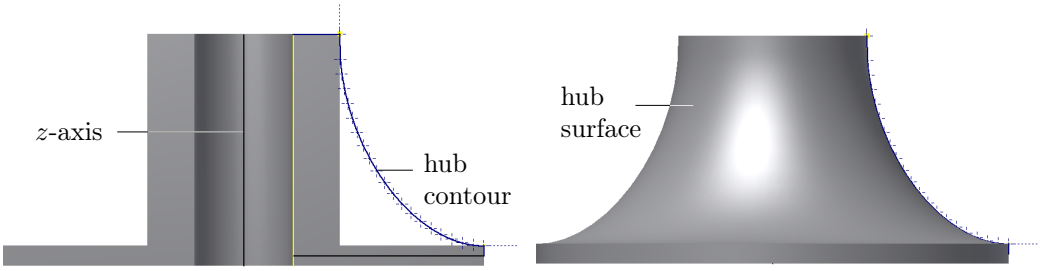


**(a)** Hub contour **(b)** Hub surface

**Figure 3.15:** Formation of rotor hub (Autodesk Inventor Professional 2011)

A MATLAB code was compiled to solve the Bezier polynomial and it wrote a *.xls* file of the Bezier polynomial curve point coordinates. These point coordinates were exported to the CAD model, where the hub contour was plotted by fitting a curve through the points, as shown in Figure 3.15a. The hub contour was then revolved about the $z$-axis to form the rotor hub surface (see Figure 3.15b).

### *Blades*

Radial inflow turbine blades are defined by the hub, shroud and camberlines (Whitfield and Baines, 1990). For this project, each blade was defined by its hub and shroud camberlines in the meridional plane. The hub and shroud camberlines were defined by two 5-point splines, created on planes parallel to the $z$-axis and tangent to the corresponding hub or shroud surface. In addition, the splines were constrained by the inlet blade angle at the leading edge and the exit blade angle at the trailing edge (see Figure 3.16), thus giving a blade angle distribution along each camberline. The blade surface was then created by lofting from the hub to the shroud camberlines, while following the blade camberline profile.

After creating the blade surface, the blade thickness distribution from hub to tip was defined. Whitfield and Baines (1990), Dixon (1998) and Aungier (2006) suggest that, in a section normal to the axis, the blade should be tapered from hub to tip, in order to improve its weight distribution and ensure the blade is thickest at its root – its greatest stress point. Whitfield and Baines note that the choice of blade thickness would normally be influenced by the choice of material for the manufacture of the rotor, stress intensity and the rotor manufacturing method, while Aungier notes that the choice of blade thickness is influenced by both aerodynamic and mechanical considerations, and suitable default values depend on the rotor application. Aungier gives blade thickness distribution correlations (Equations (3.24) and (3.25)), defining the blade thickness at the rotor inlet and the rotor exit as fractions of the rotor

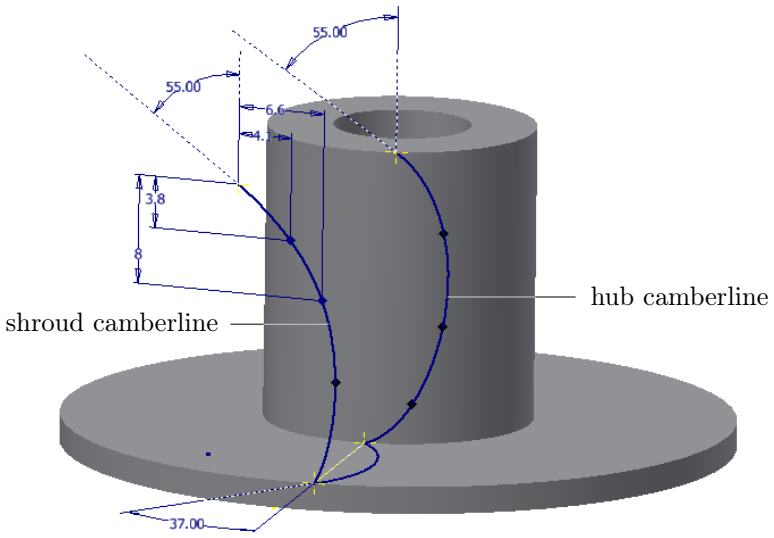


**Figure 3.16:** Blade shroud and hub camberlines (Autodesk Inventor Professional 2011)

inlet radius.

$$t_2 = 0.04r_2 \tag{3.24}$$

$$t_3 = 0.02r_2 \tag{3.25}$$

Where $t_2$ and $t_3$ is the blade thickness at the rotor inlet and outlet, respectively. The rotor outlet blade thickness value of 0.49 mm obtained from Equation (3.25) was not feasible for this rotor design, owing to strength concerns over the tapered portion of the very wide rotor blades ($r_2 = r_{3s}$). This was further compounded by the choice of material selected for the rotor manufacture. A rounded-off rotor inlet blade thickness of 1 mm was obtained from Equation (3.24), and this was therefore kept constant from the hub to the tip. After thickening the created blade, a circular pattern of nine other similar blades was created around the $z$-axis.

Finally, the leading and trailing edges of the created blades were rounded (rounding radius = 0.5 mm) and fillets of radii 1.5 mm were added at the bade/hub intersection. Whitfield and Baines (1990) propose rounding of both the leading and trailing edges; to minimise incidence sensitivity for the former and minimise the size of wake and subsequently the blade profile loss for the latter. On the other hand, adding of blade fillets leads to a reduction in stress concentration at the blade root and also aids the milling process of the rotor. The choice of rounding radius was constrained by the blade thickness while that of the fillet radii was constrained by the milling process, as the only available milling tool was of diameter 3 mm.

**Figure 3.17:** CNC milled rotor

**Figure 3.18:** CNC milled rotor fitted inside the turbine casing

### 3.3.4 Material selection and solid rotor model

Before manufacturing the turbine rotor, a choice of material from which the rotor was to be manufactured had to be made. This choice depended on three factors: 1. availability *vis-á-vis* price 2. ease of machining and 3. compatibility with both working fluids (air and refrigerant-123), with emphasis placed on good resistance to refrigerant-123 corrosion.

Verstraete *et al.* (2010) designed and manufactured a centrifugal compressor from TI-6AL-4V, a titanium alloy with very high mechanical and fatigue strength. Verstraete *et al.*'s choice of material was influenced by the need to counter the expected high centrifugal stresses on the impeller, as a result of its high tip speed. van der Merwe (2012), because of concern about the price and availability of TI-6AL-4V, rather chose to manufacture his compressor impeller from AL 7075, an aluminium alloy with mechanical strength to density ratio comparable to that of many steels and good fatigue strength. Pei *et al.* (2011), Kang (2012) and Yamamoto *et al.* (2001) all manufactured their radial inflow turbine rotors from aluminium alloy, though they all do not specify the particular alloy used.

For this project, price and availability concerns about TI-6AL-4V and the presence of copper (1.2 to 2.0%) in the composition of AL 7075 – copper containing alloys are vulnerable to stress and exfoliation corrosion (Dennis, 2013) – meant that neither TI-6AL-4V nor AL 7075 could be chosen. Rather AL 6082, an aluminium alloy whose major alloying elements are magnesium, silicon and manganese and whose fatigue strength and mechanical strength to density ratio are comparable to that of AL 7075 was chosen. AL 6082 is readily available – the ease of machining it makes it the commonest aluminium alloy for machining – and has excellent resistance to corrosion. The solid model of the designed rotor was manufactured for a price of South African rands 5600 (about US dollars 545, at the then going dollar exchange rate), and Figure 3.17 shows the manufactured rotor while Figure 3.18 shows the manufactured rotor fitted inside the turbine casing, with the clearance gap between the blade tip and the inside of the casing maintained for the whole blade height.

# Chapter 4

# Results and Analysis

During the air tests, measurements of the turbine performance parameters were taken for both the ITmini turbine rotor and the designed rotor, and turbine test data was obtained and recorded, as shown in Tables B.1 and B.2. The turbine performance characteristics defined in Subsection 2.4.2 were then calculated from the measured turbine test data, as discussed in Subsection 3.2.2, and summarised in Tables B.3 and B.4. Turbine performance maps were then plotted from the calculated performance characteristics, for both turbine rotors. The uncertainty bounds for the calculated turbine performance characteristics were also estimated by examining the effects of errors in the measured test data on the calculated turbine performance characteristics, using multiple regression analysis. The determined performance characteristics for the designed turbine rotor working with air were thereafter used to predict the performance of the turbine when working with refrigerant-123.

## 4.1 Turbine performance maps

Figure 4.1 shows the calculated non-dimensional mass flow rate plotted as a function of the turbine pressure ratio, for both tested turbine rotors. The plotted data follows the general trend shown by the typical radial inflow turbine performance map of Figure 2.11b, with the non-dimensional mass flow rate increasing with increasing turbine pressure ratio, for both tested turbine rotors. It is also seen that the non-dimensional mass flow rate of the designed rotor is higher than that of the ITmini rotor, for the same test pressure ratio range. This implies a smoother flow passage for the air flowing through the designed rotor, as compared to that of the ITmini rotor.

The turbine total to static efficiency is plotted as a function of the turbine pressure ratio in Figure 4.2, for both tested turbine rotors. The plotted data follows the general trend shown by the typical radial inflow turbine performance map of Figure 2.11a, for high turbine pressure ratios, with the total to static efficiencies achieved by both rotors decreasing with increasing turbine

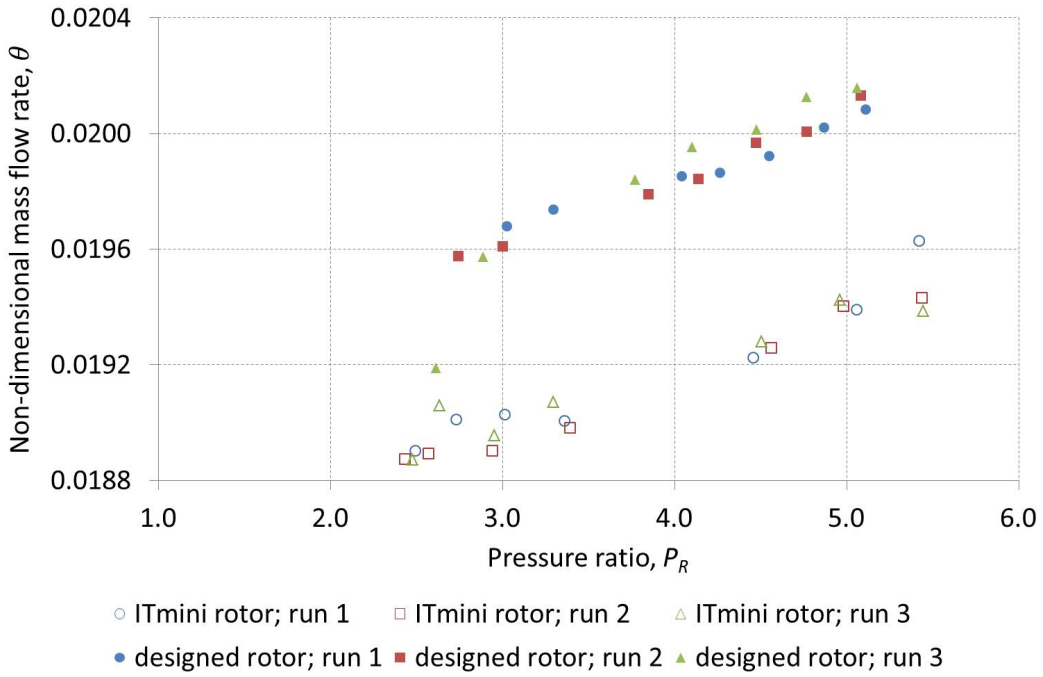


**Figure 4.1:** Non-dimensional mass flow rate vs pressure ratio for both the ITmini rotor and the designed turbine rotor

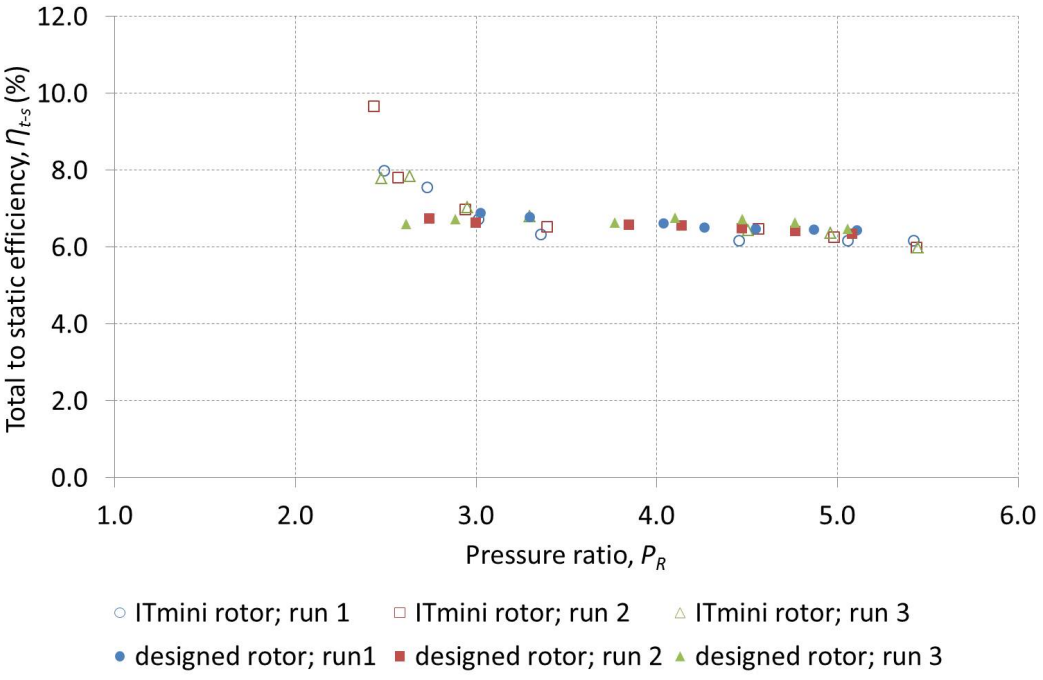


**Figure 4.2:** Total to static efficiency vs pressure ratio for both the ITmini rotor and the designed turbine rotor

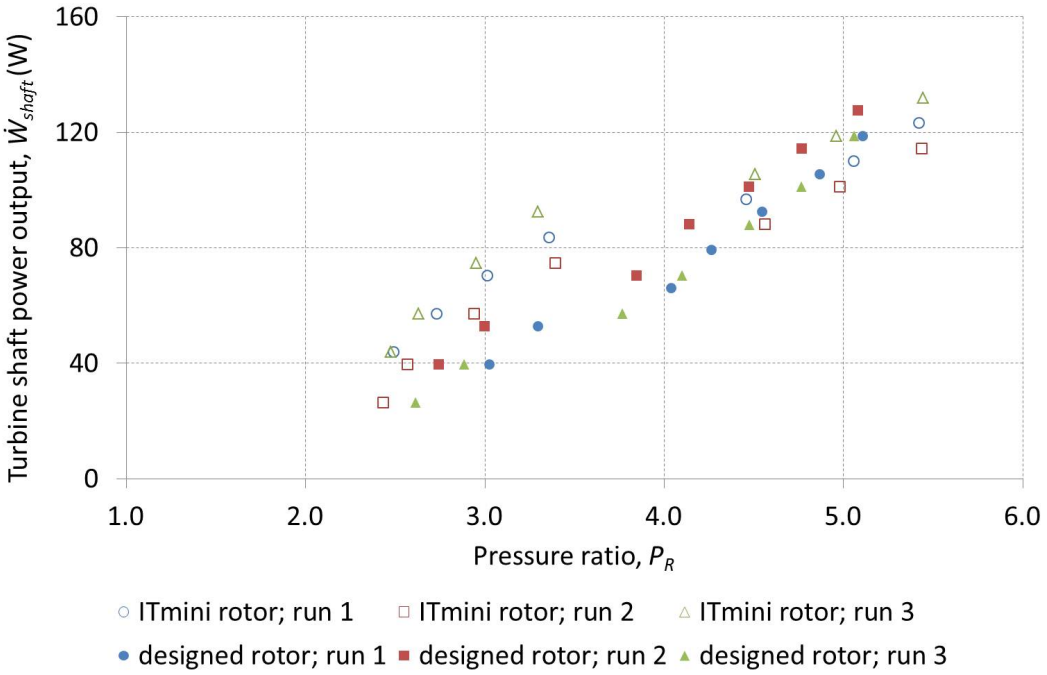


**Figure 4.3:** Turbine shaft power output vs pressure ratio for both the ITmini rotor and the designed turbine rotor

pressure ratios. It is also seen in Figure 4.2 that the total to static efficiencies achieved by the designed rotor were more consistent than those achieved by the ITmini rotor, for the same test pressure ratio range.

Figure 4.3 shows the shaft power developed by the two turbine rotors, for a constant turbine rotation speed of 5600 rpm, plotted as a function of the turbine pressure ratio. It is seen that for both tested turbine rotors, the turbine shaft power output increases with increase in turbine pressure ratio. But, for uniform loading of the turbine – with the load added sequentially for each turbine rotor test run – and for a constant turbine rotation speed, the calculated turbine shaft power output for both rotors should be closely matched, at each test point. This is not the case in Figure 4.3, and the disparity in the calculated turbine shaft power output for both tested rotors could be as a result of error in the measured turbine rotation speed and spring loaded scale displacement.

## 4.2 Uncertainties in calculated performance characteristics

Subsection 3.2.5 discussed the potential causes of errors in each measured turbine performance variable. Since the obtained turbine test data was used to

calculate the turbine performance characteristics, any error in the turbine test data was carried over to the calculated turbine performance characteristics.

In order to eliminate the bias error in the pressure, temperature and displacement measurements, the pressure sensors, thermocouples and the spring loaded scale were calibrated, as seen in Appendix A. In addition, three tests were performed for each rotor, so as to be able to estimate the precision uncertainty bounds or size of the precision error in the calculated turbine performance characteristics, through statistical analysis of the obtained turbine test data. The three tests for each rotor were performed in succession and on the same day, to minimise the variation in the turbine test conditions, especially the air properties at the turbine inlet. As can be seen in Tables B.1 and B.2, the air pressures and temperatures at the turbine inlet and the displacement did vary somewhat for each turbine test point, throughout the three tests performed for each turbine rotor. The turbine shaft power output was primarily calculated from the measured displacement and turbine rotation speed. Therefore, any variation in the measured displacement and turbine rotation speed led to variation in the calculated turbine shaft power output, for each turbine test point. Also, any variation in the air properties at the turbine inlet led to a variation in the air properties at the turbine outlet. Variation in the air properties meant that, for the turbine performance characteristics primarily calculated from these measured air properties, that is, the turbine pressure ratio, non-dimensional mass flow rate and total to static efficiency, their measurement uncertainty couldn't be determined using classical uncertainty analysis, such as that given by Beckwith *et al.* (1993), since the mean values of the varying air properties could not be obtained. Similarly, since the turbine was loaded in increments, classical uncertainty analysis could not be used to estimate the uncertainty in the calculated turbine shaft power output, as each turbine test point would have its own mean shaft power output. Instead, the measurement uncertainty bounds for the calculated turbine performance characteristics were estimated using multiple regression analysis.

Assuming the pressure ratio $P_R$ was a function of independent measured turbine performance variables, from which it is primarily calculated, as given by its definition, Equation (2.5),

$$P_R = f\left(P_1, P_3, T_1, T_3, \dot{V}\right)$$

and that this function could be represented as a power series of the form

$$P_R = a{P_1}^b {P_3}^c {T_1}^d {T_3}^e \dot{V}^f$$

then, taking natural logs on both sides yielded

$$\ln P_R = \ln a + b \ln P_1 + c \ln P_3 + d \ln T_1 + e \ln T_3 + f \ln \dot{V}$$

Using multiple regression analysis, the constants $a$, $b$, $c$, $d$, $e$ and $f$ were then determined, thus obtaining a power series that described the turbine pressure

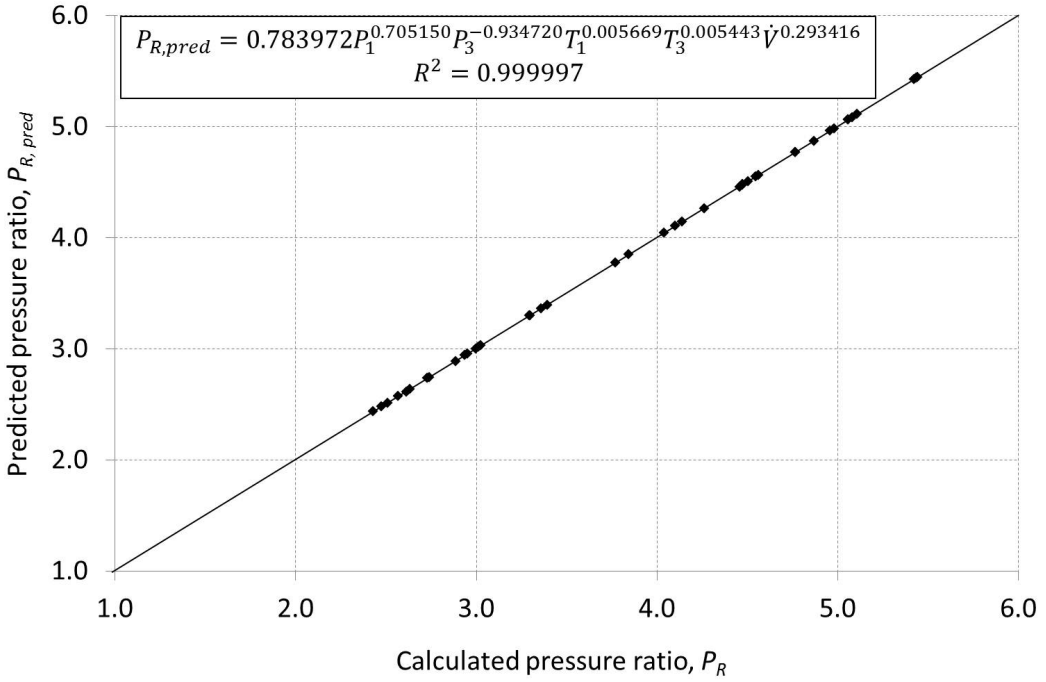


**Figure 4.4:** Predicted pressure ratio as a function of the calculated turbine pressure ratio

ratio as a function of independent measured turbine performance variables from which it is primarily calculated.

$$P_{R,pred} = 0.783972{P_1}^{0.705150}{P_3}^{-0.934720}{T_1}^{0.005669}{T_3}^{0.005443}\dot{V}^{0.293416} \tag{4.1}$$

The uncertainty in the calculated turbine pressure ratio was then estimated by plotting the predicted pressure ratio $P_{R,pred}$, calculated using Equation (4.1), against the calculated turbine pressure ratio, defined by Equation (2.5), thus obtaining Figure 4.4. Assuming the diagonal represents the mean turbine pressure ratio, it is seen that the predicted pressure ratio, plotted as a function of the calculated pressure ratio, closely matches the assumed mean pressure ratio.

Similarly, the turbine's non-dimensional mass flow rate was assumed to be defined by a function of independent measured turbine performance variables from which it is primarily calculated, that is

$$\theta = f\left(P_1, T_1, \dot{V}\right)$$

and that this function could be represented as a power series of the form

$$\theta = a{P_1}^b{T_1}^c\dot{V}^d$$

then, taking natural logs on both sides yielded

$$\ln\theta = \ln a + b\ln P_1 + c\ln T_1 + d\ln\dot{V}$$

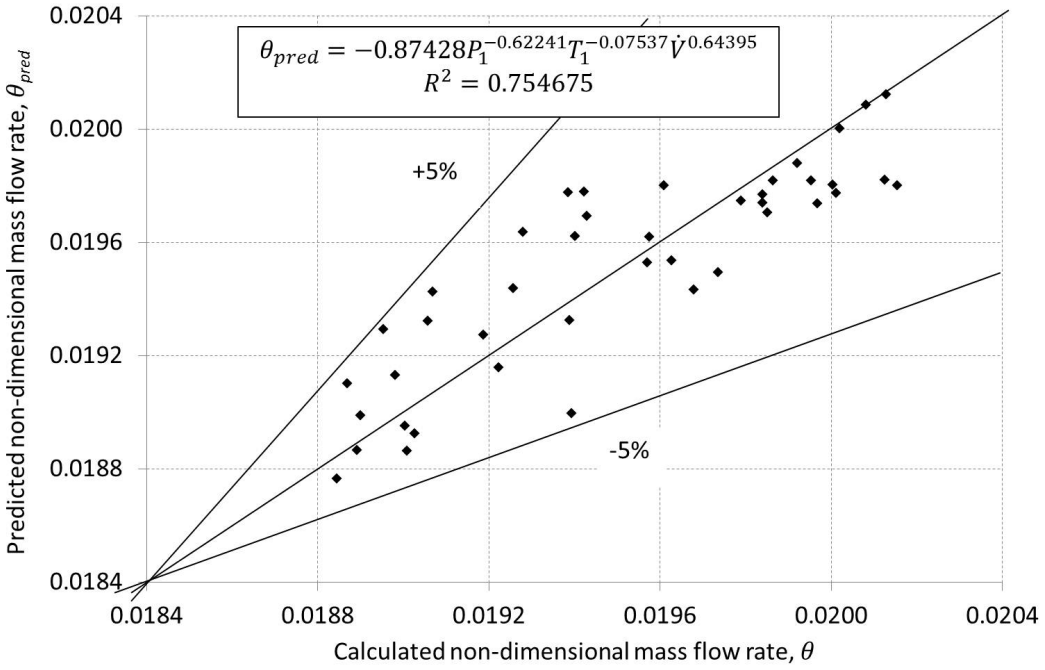


**Figure 4.5:** Predicted uncertainty bounds for the calculated turbine non-dimensional mass flow rate

Using multiple regression analysis, the constants $a$, $b$, $c$ and $d$ were then determined, thus obtaining a power series

$$\theta_{pred} = -0.87428 P_1{}^{-0.62241} T_1{}^{-0.07537} \dot{V}^{0.64395} \tag{4.2}$$

In order to estimate the bounds of the uncertainty in the calculated turbine non-dimensional mass flow rate, the predicted turbine non-dimensional mass flow rate $\theta_{pred}$, calculated using Equation (4.2), was plotted against the turbine non-dimensional mass flow rate defined by Equation (2.7), thus obtaining Figure 4.5. Similarly, assuming the diagonal represents the mean non-dimensional mass flow rate, it is seen that the predicted non-dimensional mass flow rate, plotted as a function of the calculated non-dimensional mass flow rate, lies within $\pm$ 5% of the assumed mean non-dimensional mass flow rate.

To estimate the bounds of the uncertainty in the calculated turbine total to static efficiency, as a result of uncertainty in the measured turbine performance variables from which it is primarily calculated, the turbine total to static efficiency was treated in a similar way to the pressure ratio and the non-dimensional mass flow rate; it was assumed that the total to static efficiency was defined by a function of independent measured turbine performance variables from which it is primarily calculated, that is

$$\eta = f\left(P_1, P_3, T_1, T_3, \dot{V}\right)$$

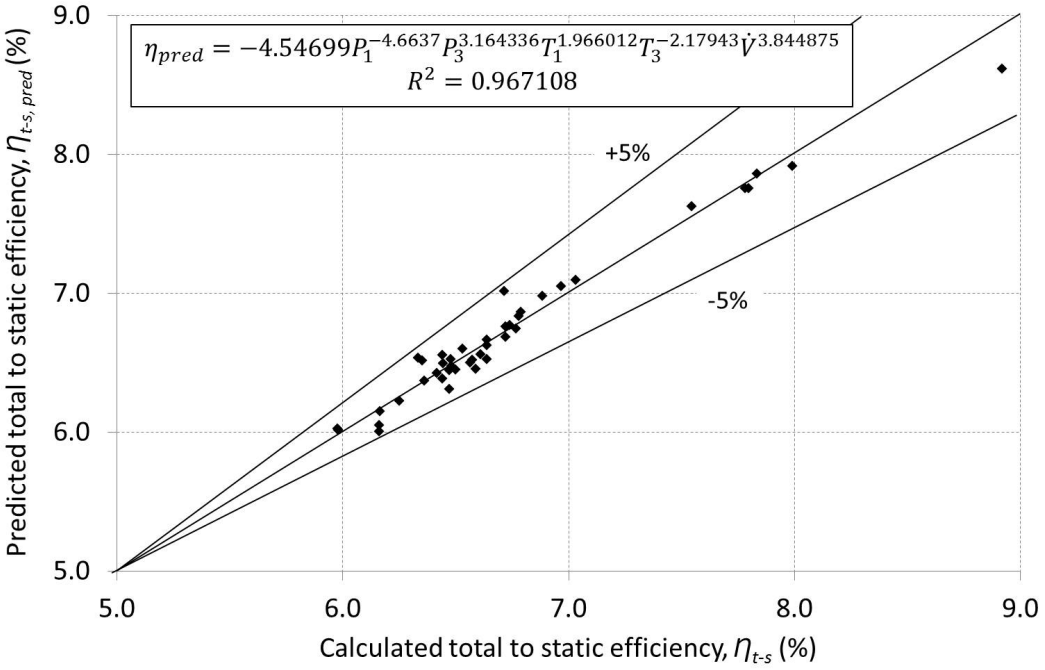


**Figure 4.6:** Predicted uncertainty bounds for the calculated turbine total to static efficiency

and that this function could be represented as a power series of the form

$$\eta = a P_1{}^b P_3{}^c T_1{}^d T_3{}^e \dot{V}^f$$

then, taking natural logs on both sides yielded

$$\ln \eta = \ln a + b \ln P_1 + c \ln P_3 + d \ln T_1 + e \ln T_3 + f \ln \dot{V}$$

Using multiple regression analysis, the constants $a$, $b$, $c$, $d$, $e$ and $f$ were then determined, thus obtaining a power series that described the turbine total to static efficiency as a function of the independent measured turbine performance variables from which it is primarily calculated (Equation (2.6)).

$$\eta_{pred} = -4.54699 P_1{}^{-4.6637} P_3{}^{3.164336} T_1{}^{1.966012} T_3{}^{-2.17943} \dot{V}^{3.844875} \tag{4.3}$$

The uncertainty bounds for the calculated turbine total to static efficiency were then estimated by plotting the predicted total to static efficiency $\eta_{pred}$, calculated from the obtained power series (Equation (4.3)) against the turbine total to static efficiency defined by Equation (2.6), thus obtaining Figure 4.6. Assuming the diagonal represents the mean total to static efficiency, it is seen that the the predicted turbine total to static efficiency, plotted as a function of the calculated turbine total to static efficiency, lies within $\pm$ 5% of the assumed mean total to static efficiency.

To estimate the uncertainty bounds for the calculated turbine shaft power output, it was assumed that the turbine rotation speed was kept constant at the no load speed, and that the turbine shaft power output was a function of only the measured displacement, that is

$$\dot{W}_{shaft} = f(x)$$

and that this function could be represented as a power series of the form

$$\dot{W}_{shaft} = ax^b$$

then, taking natural logs on both sides would yield

$$\ln \dot{W}_{shaft} = \ln a + b \ln x$$

Using multiple regression, the constants $a$ and $b$ were then determined, thus obtaining a power series that described the turbine shaft power output as a function of the measured displacement.

$$\dot{W}_{shaft,pred} = 6.125546x^{1.060075} \tag{4.4}$$

The uncertainty bounds for the calculated turbine shaft power output were then estimated by plotting the predicted turbine shaft power output $\dot{W}_{shaft,pred}$, calculated from the obtained power series (Equation (4.4)) against the turbine shaft power output defined by Equation (3.11), thus obtaining Figure 4.7. Assuming the diagonal represents the mean turbine shaft power output, it is seen that the predicted turbine shaft power output, plotted as a function of the calculated turbine shaft power output, lies well off the assumed mean turbine shaft power output, but within the + 40% bound. The large uncertainty bound explains the large disparities in the calculated turbine shaft power output for the two rotors, seen in Figure 4.3.

## 4.3 Turbine scaling for refrigerant-123 application

Using the experimentally determined turbine performance characteristics, for air as the working fluid, the turbine was then scaled for application in an organic Rankine cycle using refrigerant-123 as the working fluid. Only the designed turbine rotor was considered, due to its higher non-dimensional mass flow rate and consistent total to static efficiency, for the turbine test pressure ratio range. The scaling of the turbine followed a procedure proposed by Roberts (2001), who considered the specific heat ratio $\gamma$ an important criterion of similarity, owing to its effect on a turbomachine's non-dimensional mass flow rate, pressure ratio and efficiency. To predict the change in non-dimensional

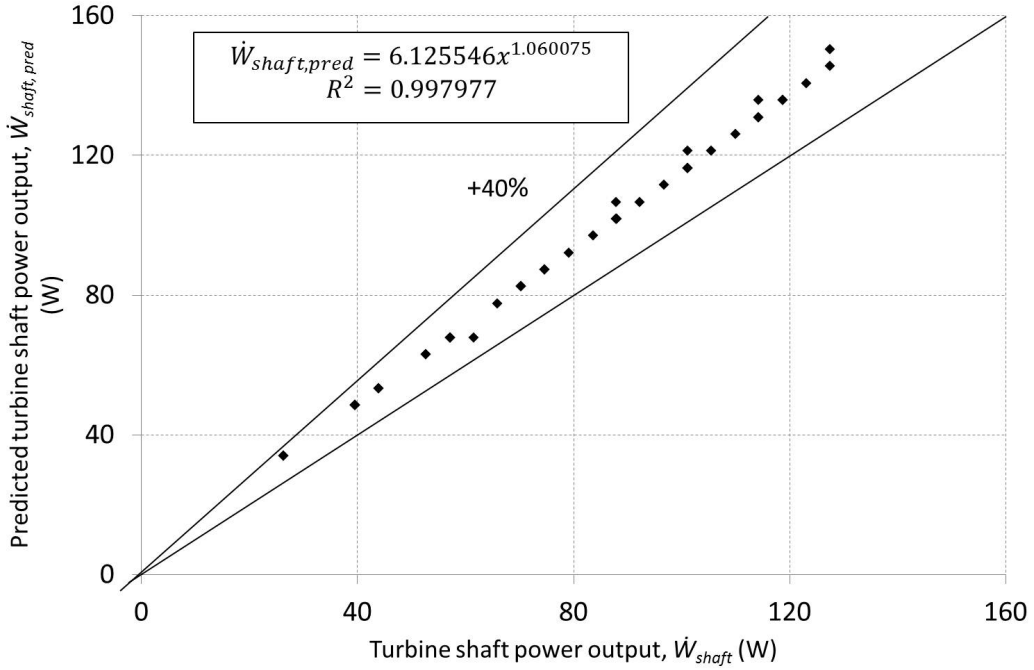


**Figure 4.7:** Predicted uncertainty bounds for the calculated turbine shaft power output

mass flow rate, efficiency and pressure ratio for a working fluid $B$, based on the test data obtained for working fluid $A$, Roberts (2001) proposed the following set of scaling equations for compressor applications, but equally applicable to turbines, with a change in the definition of the pressure ratio and the efficiency.

$$\theta_B = \theta_A \frac{\left(\frac{2}{\gamma_B+1}\right)^{\frac{1+\gamma_B}{2(\gamma_B-1)}}}{\left(\frac{2}{\gamma_A+1}\right)^{\frac{1+\gamma_A}{2(\gamma_A-1)}}} \tag{4.5}$$

$$\frac{\eta_B}{\eta_A} = \frac{1}{\eta_A} + \left(\frac{\gamma_B}{\gamma_A}\right)^{0.8}\left(1 - \frac{1}{\eta_A}\right) \tag{4.6}$$

$$P_{RB} = \left[1 + \frac{\eta_B}{\eta_A}\left(\frac{\gamma_B - 1}{\gamma_A - 1}\right)\left(P_{RA}^{\frac{\gamma_A-1}{\gamma_A}} - 1\right)\right]^{\frac{\gamma_B}{\gamma_B-1}} \tag{4.7}$$

To suit single stage turbine applications, the efficiencies and pressure ratios in Equations (4.6) and (4.7) were redefined as total to static efficiency and inlet total to exit static pressure ratio, as given in Subsection 2.4.2.

Figures 4.8 and 4.9 show the predicted turbine performance maps for the turbine using refrigerant-123 as the working fluid, obtained by applying Equations (4.5) to (4.7) and using the performance characteristics obtained for the turbine working with air. The predicted non-dimensional mass flow rate,

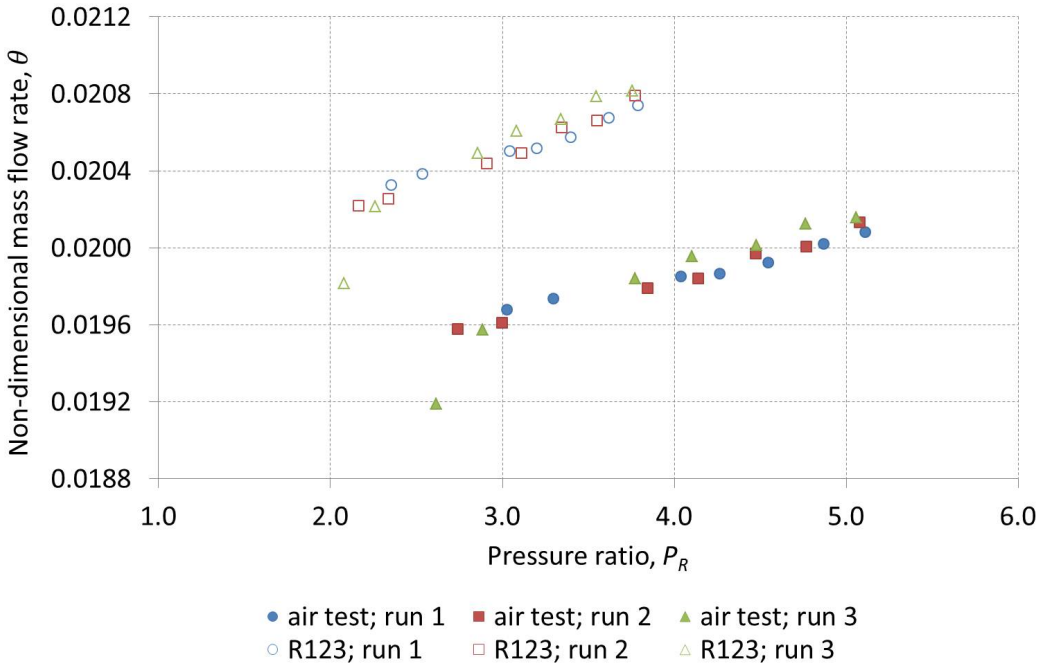


**Figure 4.8:** Non-dimensional mass flow rate vs pressure ratio for both air and refrigerant-123 working fluids

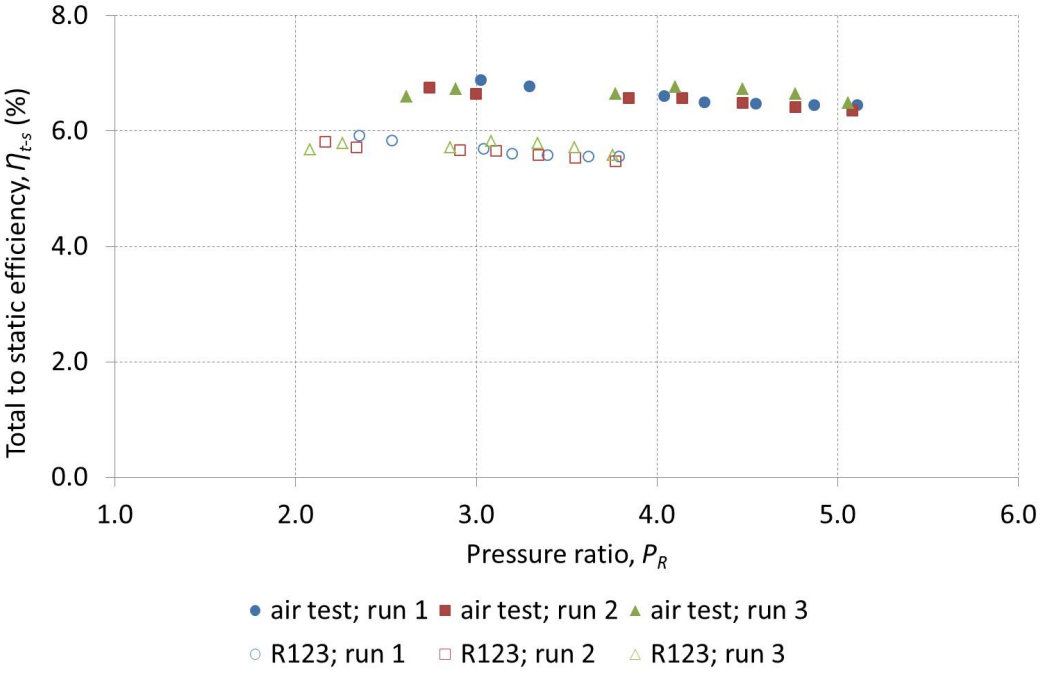


**Figure 4.9:** Total to static efficiency vs pressure ratio for both air and refrigerant-123 working fluids

plotted as a function of the predicted turbine pressure ratio, for the turbine working with refrigerant-123 ($\gamma = 1.12$) is higher than that determined from test data obtained for the turbine working with air ($\gamma = 1.4$). This is as predicted by Roberts (2001), who expects an increase in the non-dimensional mass flow rate of a turbine, for decreasing values of the specific heat ratio. The predicted turbine total to static efficiency, for the turbine working with refrigerant-123 as the working fluid is lower than that determined from the test data for the turbine working with air, and similarly, the predicted operating pressure ratio range is lower than that determined for the turbine working with air. According to Roberts, an increase in specific heat ratio should result in a decrease in expansion and turbine discharge velocity, for the same pressure ratio, in turn leading to an increase in turbine efficiency, as illustrated by the higher efficiency for the turbine working with air. It is also predicted that the turbine working with refrigerant-123 will require a lower pressure ratio to drive the turbine at a given value of the non-dimensional rotor blade tip speed $M_u$ (Equation 2.8).

# Chapter 5

# Discussion, Conclusion and Recommendations

The aim of this project was to validate the use of a turbine for application in a low grade waste heat recovery and utilisation system. This entailed characterising the turbine for low temperature and low pressure conditions, using air as the working fluid, and then using the determined performance characteristics to scale it for refrigerant-123 application, in order to predict its performance for integration into an organic Rankine cycle waste heat recovery and utilisation system.

An experimental turbine kit was sourced and assembled. Then, an air test bench was designed and built, and the assembled turbine tested, using air as the working fluid. The turbine was thereafter characterised using the obtained test data, and the turbine performance maps plotted from the determined turbine performance characteristics. As seen in Figures 4.1 to 4.3 and Table B.3, for the turbine test pressure ratio range of 2.4 to 5.4, non-dimensional mass flow rates ranging from 0.0189 to 0.0196, turbine shaft power output ranging from 26.5 to 132 W and total to static efficiencies ranging from 6.0 to 9.7% were achieved. The acquired ITmini turbine achieved its highest efficiencies at the lower end of the turbine test pressure ratio range, and the efficiency gradually decreased as the turbine pressure ratio increased. On the other hand, the non-dimensional mass flow rate and shaft power output achieved for the turbine test pressure ratio range increased with subsequent increase in the pressure ratio. It should be noted that increase in pressure ratio subsequently implied increase in the turbine inlet gauge pressure, as the turbine outlet gauge pressure was kept as close as possible to zero, by discharging to the atmosphere.

A radial inflow turbine rotor was thereafter designed and manufactured, and it was tested with air as well, and the new turbine performance characteristics determined and performance maps plotted. As seen in Figures 4.1 to 4.3 and Table B.4, for the turbine test pressure ratio range of 2.6 to 5.1, non-dimensional mass flow rates ranging from 0.0192 to 0.0202, turbine shaft power output ranging from 26.5 to 127.6 W and total to static efficiencies rang-

ing from 6.4 to 6.9% were achieved. For the turbine test pressure ratio range, the total to static efficiencies achieved for the designed rotor were marginally higher and more consistent for the higher test pressure ratio range, as compared to those achieved for the ITmini rotor. Similar to the ITmini rotor, the non-dimensional mass flow rate and shaft power output achieved for the designed rotor increased with subsequent increase in the pressure ratio, but with higher non-dimensional mass flow rates achieved for the designed rotor. Overall, very similar performance was exhibited by both turbine rotors, with very low isentropic efficiency observed in the turbine, for both rotors (6 to 10%), as compared to that of other turbines from literature (60 to 80%). The similar performance is attributed to maintaining of the existing turbine casing for both rotors, thus maintaining the inlet and outlet flow conditions of the turbine for both rotors. The low isentropic efficiency is attributed to the low test temperatures and pressures, as a result of using air at room temperature for the tests. The design point theoretical efficiency obtained from the design code for the designed rotor was also low (17.7%).

From the determined performance characteristics for the designed turbine rotor working with air, the turbine was scaled for refrigerant-123 application, and its performance for integration into an organic Rankine cycle waste heat recovery and utilisation system predicted (see Subsection 4.3). For a predicted turbine operating pressure ratio range of 2.1 to 3.8, the turbine scaling predicted total to static efficiencies ranging from 5.5 to 5.9% and non-dimensional mass flow rates ranging from 0.0198 to 0.0208.

Through the project work, the turbine performance characteristics for low temperature (less than 120 °C) and low pressure (less than 10 bar) conditions were determined for both turbine rotors working with air, and those determined for the better performing designed rotor used to predict the turbine performance characteristics for integration into an organic Rankine cycle low grade waste heat recovery and utilisation system. From the determined turbine performance characteristics, turbine performance maps were plotted, and these performance maps followed the general trend for the typical turbine performance maps given by Whitfield and Baines (1990) (see Figure 2.11), as shown and discussed in Subsections 4.1 and 4.3. The calculation of the turbine performance characteristics was also verified using a sample calculation of the turbine performance characteristics for the turbine working with both air and refrigerant-123, for the second test run of the designed turbine rotor, at test point 6, with the obtained results closely matching those calculated and tabulated in Table B.4. Thus, through the project work, the use of a turbine for application in a low grade waste heat recovery and utilisation system was validated.

For future work, the turbine should be integrated into an organic Rankine cycle low grade waste heat recovery and utilisation system using refrigerant-123 as the working fluid, and the predicted turbine performance characteristics for the turbine working with refrigerant-123 verified experimentally. It is predicted

though, that the turbine shaft power output for the turbine working with refrigerant-123 will be highly dependent on the volumetric flow rate – and the resulting fluid flow velocity – of the organic Rankine cycle system, owing to the turbine being of the dynamic (velocity) type. Due care should therefore be taken to select appropriate volumetric flow rates for the desired turbine shaft power output. Any future work should also entail testing the turbine at constant test conditions, so as to allow for the use of classical uncertainty analysis in the determination of the uncertainty bounds for the calculated turbine performance characteristics.

# Appendices

# Appendix A

# Instrumentation Calibration

## A.1 Calibration of the pressure sensors

The two Festo SDE3 presure sensors [serial numbers P8XMV8 and P8XXTF] were statically calibrated against a 2500 kPa Wika pressure gauge [serial number 720223 and calibrated on 06/06/2011], for the expected air test operating pressure range of 1 to 10 bar. The calibration set up included a Festo LFR-1 series pressure regulator, with an operating range of 0.5 to 12 bar, as shown in Figure A.1. The gauge pressure was set using the pressure regulator, and the corresponding sensor pressure was then visually read off and recorded, as shown in Table A.1 and A.2. Linear trendlines were obtained on plotting the sensor pressure readings against the corresponding set gauge pressures, as shown in Figures A.2 and A.3. The linear trendline Equations (A.1) and (A.2) that were obtained from the plotted data, were in turn used to correct the

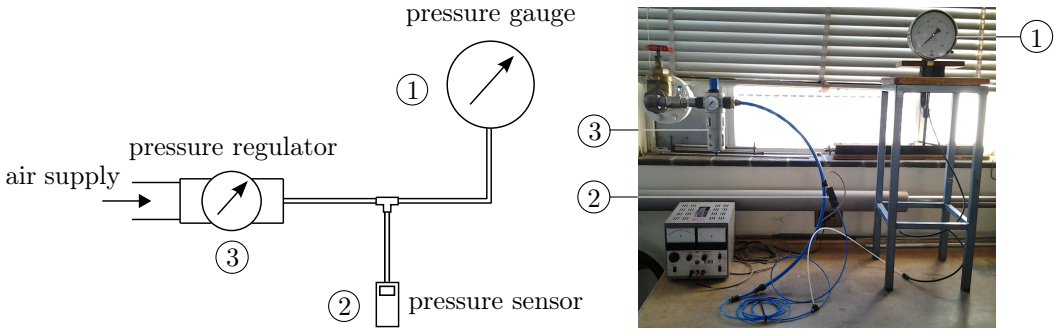


**(a)** Schematic layout **(b)** Physical set up

**Figure A.1:** Pressure sensor static calibration set up; 1. Pressure gauge, 2. Pressure sensor, 3. Pressure regulator

**Table A.1:** Data obtained from the calibration of pressure sensor P8XMV8

| Corrected pressure $P_{corr}$ [bar] | Measured pressure $P_{meas}$ [bar] |
|---|---|
| 1.0 | 0.97 |
| 2.0 | 1.97 |
| 3.0 | 2.98 |
| 4.0 | 3.97 |
| 5.0 | 4.99 |
| 6.0 | 5.98 |
| 7.0 | 6.97 |
| 8.0 | 7.99 |
| 9.0 | 9.00 |
| 9.6 | 9.54 |

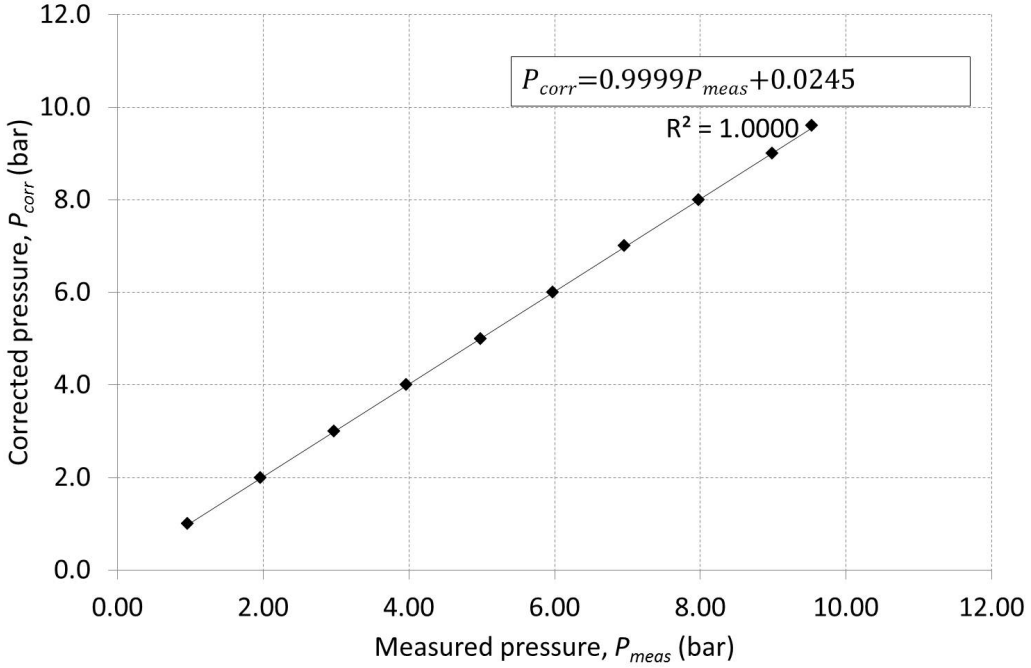


**Figure A.2:** Linear correlation between corrected and actual measured pressure (sensor P8XMV8)

measured turbine inlet and exit pressure.

$$P_{in,corr} = 0.9999 P_{in,meas} + 0.0245 \tag{A.1}$$

$$P_{out,corr} = 1.0000 P_{out,meas} + 0.0170 \tag{A.2}$$

**Table A.2:** Data obtained from the calibration of pressure sensor P8XXTF

| Corrected pressure $P_{corr}$ [bar] | Measured pressure $P_{meas}$ [bar] |
|---|---|
| 1.0 | 0.99 |
| 2.0 | 1.98 |
| 3.0 | 2.97 |
| 4.0 | 3.98 |
| 5.0 | 4.97 |
| 6.0 | 6.00 |
| 7.0 | 7.00 |
| 8.0 | 7.99 |
| 9.0 | 9.00 |
| 9.6 | 9.55 |

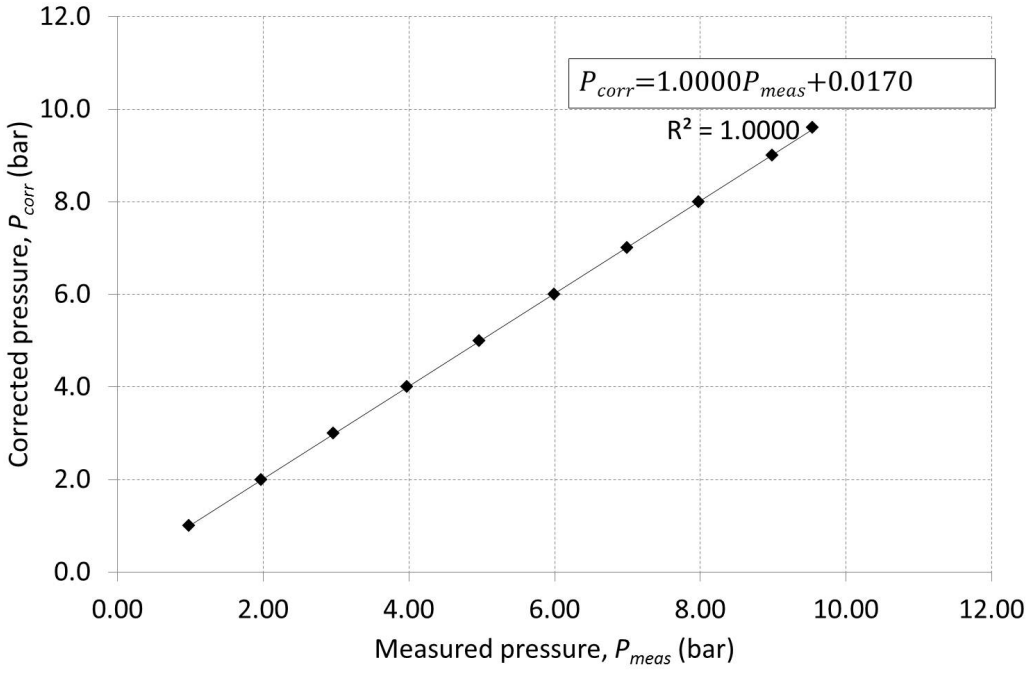


**Figure A.3:** Linear correlation between corrected and measured pressure ( sensor P8XXTF)

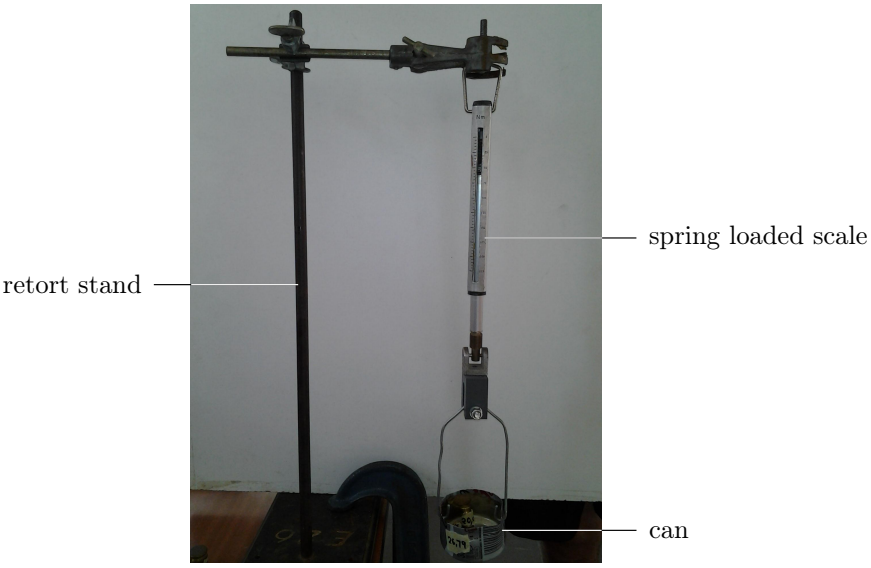


**Figure A.4:** Calibration set up for the spring loaded scale

## A.2 Calibration of the spring loaded scale

The scale of the spring loaded scale was calibrated against brass metric weights of known weight, as shown in Figure A.4. The brass weights and the can were first weighed using a Precisa 40SM-200A [serial number 73464] electronic precision balance, with two weighing ranges: $41 \times 0.01$ mg and $201 \times 0.1$ mg. The zero loading reading of the spring loaded scale was then noted, and starting with the known weight of the empty can, and gradually adding weights, the corresponding vertical displacement $x$ on the spring loaded scale was visually read off and recorded, as shown in Table A.3. A linear trendline (see Figure

**Table A.3:** Data obtained from the calibration of the spring loaded scale

| Weight [N] | Vertical displacement, $x$ |
|---|---|
| 0.26 | 0.07 |
| 0.36 | 0.09 |
| 0.46 | 0.12 |
| 0.56 | 0.14 |
| 0.66 | 0.16 |
| 0.75 | 0.18 |
| 0.85 | 0.20 |
| 0.95 | 0.23 |
| 1.15 | 0.27 |
| 1.34 | 0.32 |

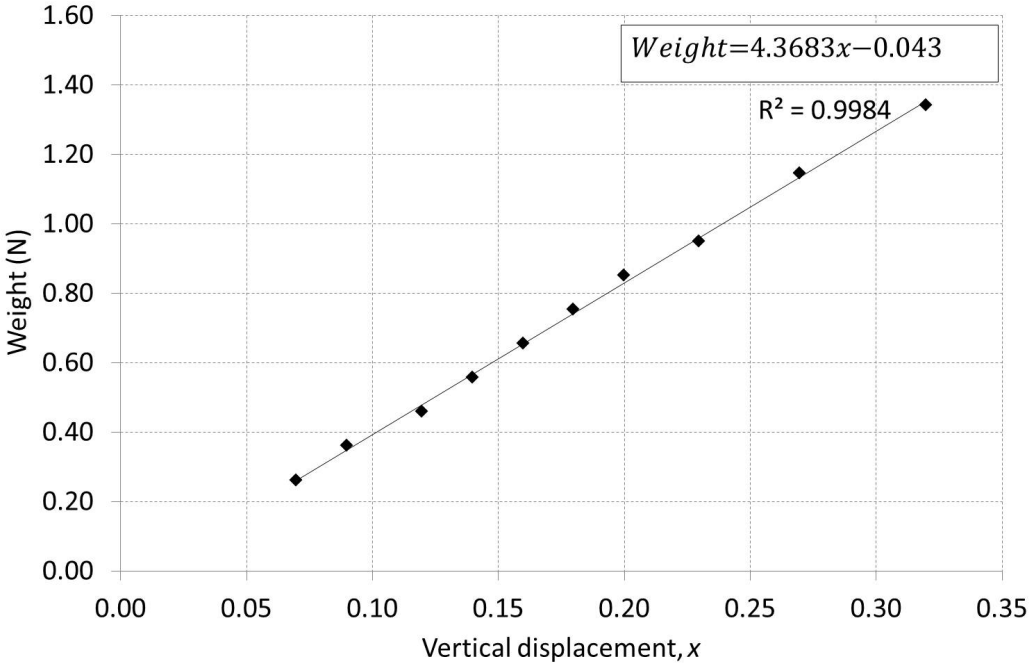


**Figure A.5:** Correlation between weight and vertical displacement

A.5) and trendline equation (Equation (A.3)) were obtained on plotting the the weight exerted onto the scale by the added weights against the resulting vertical displacement of the spring.

$$Weight = 4.3683x - 0.043 \tag{A.3}$$

Equation (A.3) was then used to calculate the weight exerted by the torque arm onto the scale during the loading of the turbine, and this calculated weight was in turn used to calculate the torque exerted by the turbine shaft onto the coupled generator shaft, using Equation (3.13).

## A.3 Calibration of the thermocouples

The five T-type thermocouples used for temperature measurement during the air test were calibrated against an Isotech platinum resistance thermometer [model number 935-14-72, serial number 191069 and calibrated on 4/02/2013], using a Fluke 9142 Field Metrology Well thermocouple calibrator [serial number B29291]. For the expected air test temperature operating range of 0 to 35 °C, a known temperature $T_0$ was set on the thermocouple calibrator, and after allowing a period of stabilisation, the data logger was used to log the reference thermometer temperature $T_{ref}$ and the thermocouples' temperatures $T_1$, $T_2$, $T_3$, $T_4$ and $T_5$. These temperatures were then recorded, as shown in Table A.4. The measured thermocouple temperatures were then plotted against the

**Table A.4:** Data obtained from the calibration of the thermocouples

| $T_0$ [°C ] | $T_1$ [°C ] | $T_2$ [°C ] | $T_3$ [°C ] | $T_4$ [°C ] | $T_5$ [°C ] | $T_{ref}$ [°C ] |
|---|---|---|---|---|---|---|
| 0 | 1.2 | 0.9 | 1.0 | 1.0 | 0.9 | 0.3 |
| 5 | 5.9 | 5.7 | 5.8 | 5.8 | 5.7 | 5.2 |
| 10 | 10.7 | 10.6 | 10.6 | 10.7 | 10.6 | 10.1 |
| 15 | 15.6 | 15.5 | 15.5 | 15.5 | 15.4 | 15.0 |
| 20 | 20.4 | 20.4 | 20.3 | 20.3 | 20.3 | 20.0 |
| 25 | 25.3 | 25.3 | 25.3 | 25.3 | 25.2 | 24.9 |
| 30 | 30.2 | 30.3 | 30.2 | 30.2 | 30.2 | 29.9 |
| 35 | 35.1 | 35.2 | 35.1 | 35.1 | 35.1 | 34.9 |

calibration (reference) temperatures, as shown in Figures A.6a – e, and linear trendline Equations (A.4), (A.6), (A.7), (A.8) and (A.9) were obtained from the plotted data. The data logger was then configured to correct the measured thermocouple temperatures using the obtained linear trendline equations, with the corrected turbine inlet and outlet temperatures given by Equations (A.5) and (A.10).

$$T_{1,corr} = 1.0181T_{1,meas} - 0.8218 \tag{A.4}$$

$$T_{in,corr} = T_{1,corr} \tag{A.5}$$

$$T_{2,corr} = 1.0075T_{2,meas} - 0.5807 \tag{A.6}$$

$$T_{3,corr} = 1.0110T_{3,meas} - 0.6155 \tag{A.7}$$

$$T_{4,corr} = 1.0135T_{4,meas} - 0.6797 \tag{A.8}$$

$$T_{5,corr} = 1.0087T_{5,meas} - 0.5327 \tag{A.9}$$

$$T_{out,corr} = \frac{T_{2,corr} + T_{3,corr} + T_{4,corr} + T_{5,corr}}{4} \tag{A.10}$$

For the temperature measurement uncertainty, selected temperatures in the interval of 5 °C, for the expected temperature operating range of 0 to 35 °C, were set on the thermocouple calibrator and the corresponding reference and thermocouple temperatures measured and recorded. The recorded thermocouple temperatures were then corrected using their relevant correcting equations, and the temperature measurement uncertainty determined from the difference between the corrected thermocouple temperature and the corresponding reference temperature, $T_{n,corr} - T_{ref}$, where $n$ refers to a given thermocouple. The measurement uncertainty was then plotted against the set temperatures, so as to obtain the uncertainty bounds, as shown in Figure A.6f. It can be seen that the temperature measurement uncertainty, after calibration, does not exceed $\pm$ 0.15 °C, as suggested by Brun and Nored (2006).

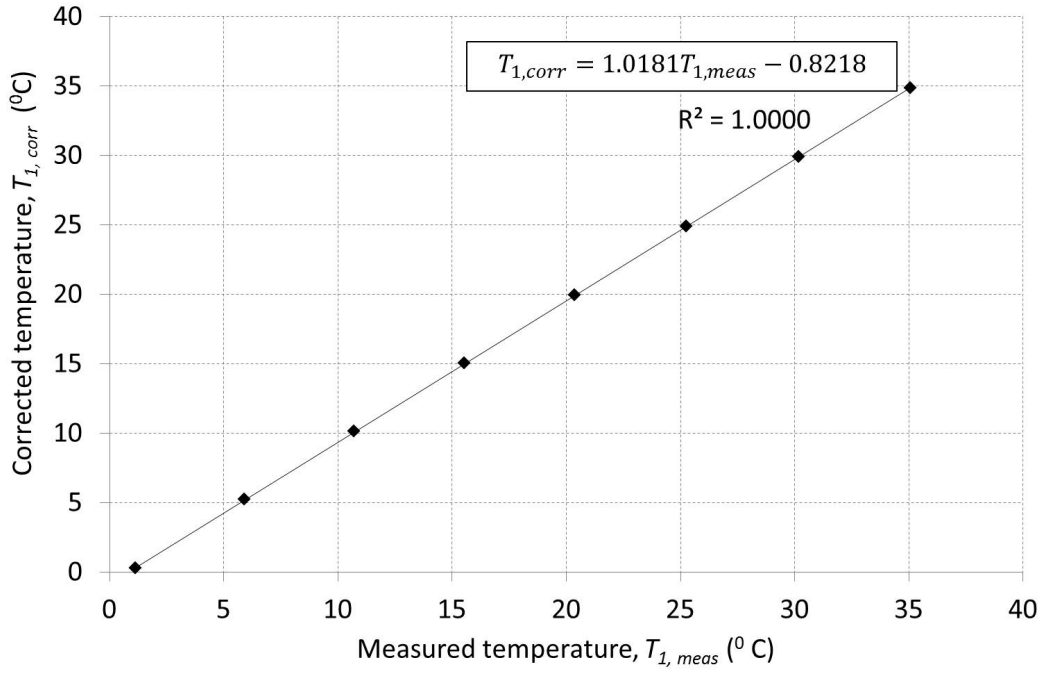


**(a)** Thermocouple 1

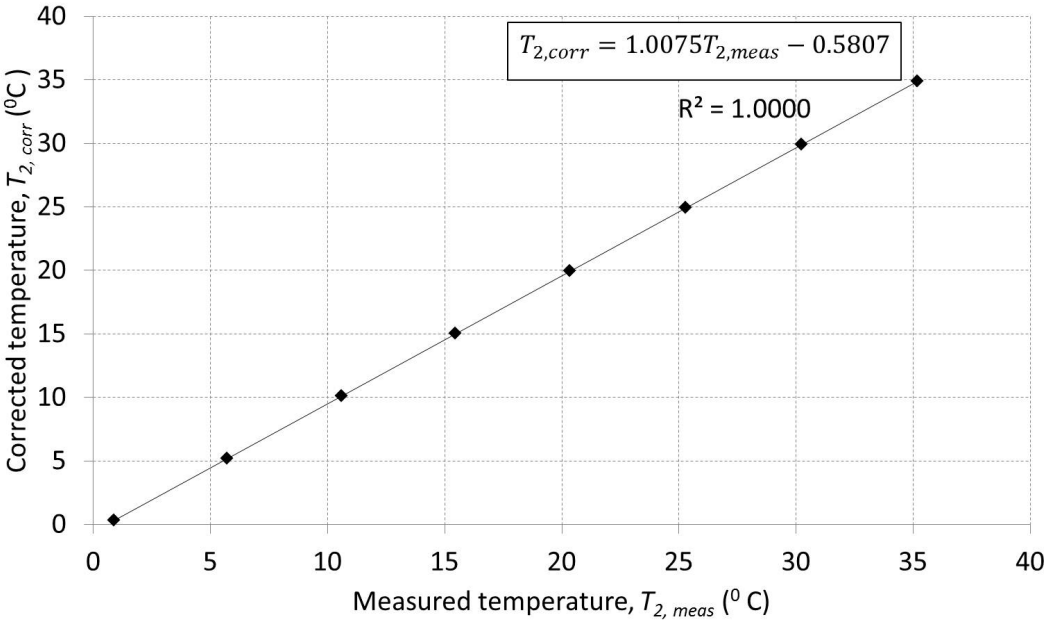


**(b)** Thermocouple 2

**Figure A.6:** Plotted thermocouple calibration data

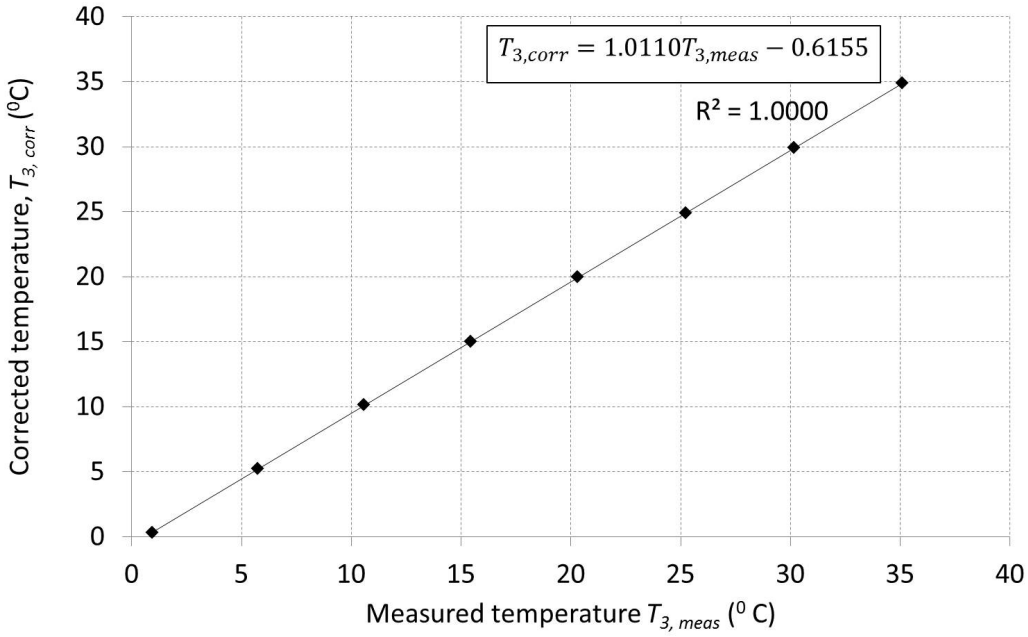


**(c)** Thermocouple 3

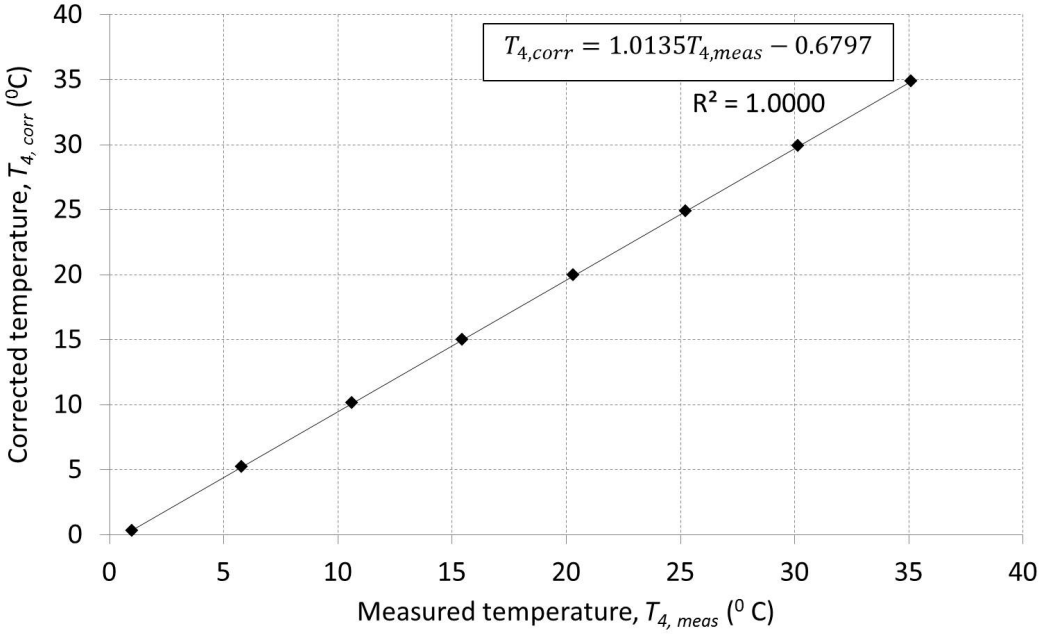


**(d)** Thermocouple 4

**Figure A.6:** Plotted thermocouple calibration data (cont'd)

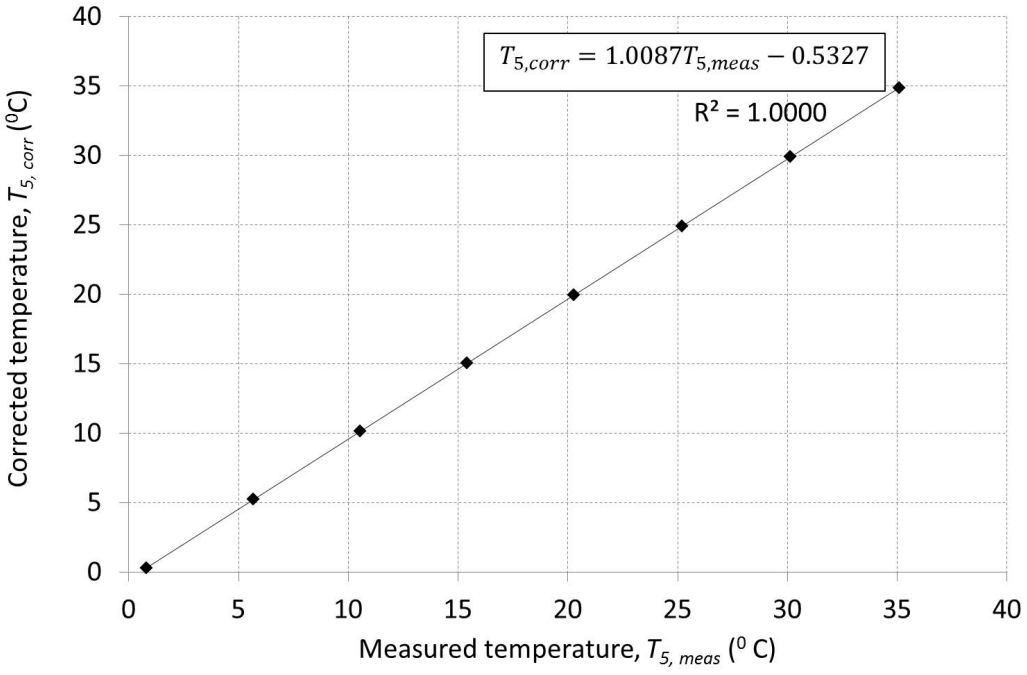


**(e)** Thermocouple 5

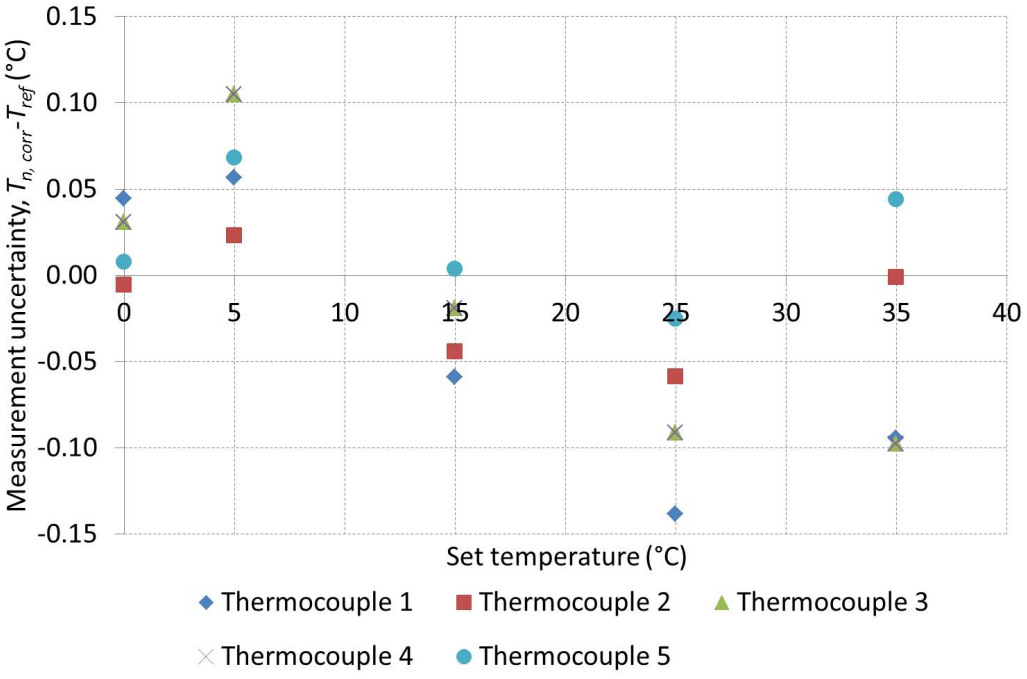


**(f)** Temperature measurement uncertainty

**Figure A.6:** Plotted thermocouple calibration data (cont'd)

# Appendix B

# Test Data, Sample Calculation and Calculated Turbine Performance Characteristics

## B.1 Test data

Tables B.1 and B.2 show the test data obtained from the measurements taken during the air tests, for both the ITmini rotor and the designed rotor.

## B.2 Sample calculation

In this sample calculation, the non-dimensional mass flow rate, pressure ratio total to static efficiency and shaft power output, for the turbine working with air, and then scaled for refrigerant-123 application, are determined, using the test data obtained for the second test run of the designed turbine rotor, at test point 6 (see Table B.2)

**Assumptions**: Steady, one-dimensional, compressible flow through the turbine, with both air and refrigerant-123 behaving as ideal gases with constant specific heat ratios.

**Physical constants**:

$g = 9.81$ m/s$^2$

**Fluid properties**:

$\gamma_{air} = 1.4$
$\gamma_{R123} = 1.12$
$R_{air} = 287$ J/kgK
$c_p = 1007$ J/kgK
$P_{atm} = 100410$ Pa
$P_{stand.conds} = 101325$ Pa

**Table B.1:** Test data obtained from the air test for the ITmini rotor

| Test run | Test point | $P_1$ [bar] | $T_1$ [°C] | $P_3$ [bar] | $T_3$ [°C] | | | | $\dot{V}$ [L/min] | $x$ | $I$ [A] |
|---|---|---|---|---|---|---|---|---|---|---|---|
| 1 | no-load | 1.20 | 23.9 | 0.00 | 29.0 | 28.9 | 28.8 | 28.9 | 1722 | 0.11 | 0.00 |
| | 1 | 1.41 | 23.8 | 0.00 | 28.8 | 28.6 | 28.6 | 28.8 | 1899 | 0.14 | 0.82 |
| | 2 | 1.66 | 23.7 | 0.00 | 28.8 | 28.6 | 28.6 | 28.8 | 2097 | 0.17 | 1.63 |
| | 3 | 1.97 | 23.7 | 0.00 | 28.4 | 28.3 | 28.3 | 28.5 | 2336 | 0.20 | 2.30 |
| | 4 | 2.93 | 24.8 | 0.00 | 28.4 | 28.3 | 28.1 | 28.1 | 3126 | 0.23 | 2.97 |
| | 5 | 3.45 | 25.1 | 0.00 | 28.1 | 27.9 | 27.8 | 27.6 | 3575 | 0.26 | 3.69 |
| | 6 | 3.75 | 25.3 | 0.00 | 28.1 | 27.8 | 27.8 | 27.6 | 3875 | 0.29 | 4.40 |
| 2 | no-load | 1.15 | 22.8 | 0.00 | 28.0 | 27.8 | 27.7 | 27.9 | 1680 | 0.07 | 0.00 |
| | 1 | 1.27 | 22.3 | 0.00 | 27.3 | 27.2 | 27.1 | 27.2 | 1780 | 0.10 | 0.80 |
| | 2 | 1.60 | 21.6 | 0.00 | 26.4 | 26.3 | 26.2 | 26.4 | 2040 | 0.14 | 1.60 |
| | 3 | 2.00 | 21.4 | 0.00 | 25.8 | 25.7 | 25.7 | 25.9 | 2365 | 0.18 | 2.37 |
| | 4 | 3.02 | 21.9 | 0.00 | 25.1 | 24.9 | 24.7 | 24.7 | 3220 | 0.21 | 3.10 |
| | 5 | 3.38 | 21.6 | 0.00 | 24.6 | 24.4 | 24.2 | 24.2 | 3543 | 0.24 | 3.69 |
| | 6 | 3.78 | 21.5 | 0.00 | 24.2 | 23.9 | 23.9 | 23.7 | 3873 | 0.27 | 4.34 |
| 3 | no-load | 1.19 | 19.3 | 0.00 | 24.5 | 24.3 | 24.2 | 24.4 | 1724 | 0.11 | 0.00 |
| | 1 | 1.32 | 18.9 | 0.00 | 23.9 | 23.7 | 23.7 | 23.9 | 1850 | 0.14 | 0.81 |
| | 2 | 1.61 | 18.8 | 0.00 | 23.5 | 23.4 | 23.4 | 23.6 | 2065 | 0.18 | 1.58 |
| | 3 | 1.91 | 18.9 | 0.00 | 23.3 | 23.2 | 23.3 | 23.4 | 2318 | 0.22 | 2.28 |
| | 4 | 2.97 | 19.9 | 0.00 | 23.2 | 23.0 | 22.8 | 22.9 | 3196 | 0.25 | 3.05 |
| | 5 | 3.36 | 20.1 | 0.00 | 23.0 | 22.8 | 22.7 | 22.6 | 3541 | 0.28 | 3.69 |
| | 6 | 3.79 | 20.2 | 0.00 | 22.8 | 22.5 | 22.6 | 22.3 | 3878 | 0.31 | 4.41 |

$P_1 = 3.50$ bar
$P_3 = 0.00$ bar
$T_1 = 16.2$ °C
$T_3 = (18.9 + 18.4 + 18.2 + 18.7)/4$ °C
$T_{stand.conds} = 0$ °C

**Dimensions**:

$l = 171.7$ mm
$d_1 = 11$ mm
$d_2 = 48.86$ mm
$d_3 = 35.8$ mm
$\dot{V} = 3662$ L/min
$N = 5600$ rpm

**Others**:

$x = 0.30$
$I = 4.45$ A
$E_g = 24$ V

In order to calculate the non-dimensional mass flow rate, for the turbine tested with air $\theta_{air}$, it is first necessary to calculate the mass flow rate through the turbine and the turbine inlet stagnation temperature and pressure. The mass

**Table B.2:** Test data obtained from the air test for the designed rotor

| Test run | Test point | $P_1$ [bar] | $T_1$ [°C ] | $P_3$ [bar] | $T_3$ [°C ] | | | | $\dot{V}$ [L/min] | $x$ | $I$ [A] |
|---|---|---|---|---|---|---|---|---|---|---|---|
| 1 | no-load | 1.69 | 17.1 | 0.00 | 21.6 | 21.6 | 21.8 | 21.6 | 2132 | 0.10 | 0.00 |
| | 1 | 1.93 | 17.3 | 0.00 | 21.4 | 21.5 | 21.7 | 21.5 | 2328 | 0.13 | 0.81 |
| | 2 | 2.59 | 17.0 | 0.00 | 20.6 | 20.0 | 20.0 | 20.6 | 2870 | 0.16 | 1.60 |
| | 3 | 2.79 | 16.3 | 0.00 | 19.6 | 19.1 | 19.1 | 19.7 | 3035 | 0.19 | 2.30 |
| | 4 | 3.04 | 16.4 | 0.00 | 19.4 | 18.9 | 18.9 | 19.4 | 3245 | 0.22 | 3.01 |
| | 5 | 3.32 | 16.3 | 0.00 | 19.0 | 18.5 | 18.4 | 19.0 | 3491 | 0.25 | 3.70 |
| | 6 | 3.53 | 16.2 | 0.00 | 18.7 | 18.2 | 18.0 | 18.5 | 3675 | 0.28 | 4.37 |
| 2 | no-load | 1.44 | 14.4 | 0.00 | 19.4 | 19.4 | 19.5 | 19.4 | 1932 | 0.10 | 0.00 |
| | 1 | 1.67 | 13.5 | 0.00 | 18.1 | 18.1 | 18.3 | 18.1 | 2120 | 0.13 | 0.81 |
| | 2 | 2.42 | 16.0 | 0.00 | 19.8 | 19.2 | 19.3 | 19.9 | 2729 | 0.17 | 1.60 |
| | 3 | 2.68 | 16.7 | 0.00 | 20.1 | 19.6 | 19.6 | 20.2 | 2941 | 0.21 | 2.34 |
| | 4 | 2.97 | 18.0 | 0.00 | 21.2 | 20.7 | 20.6 | 21.2 | 3190 | 0.24 | 3.01 |
| | 5 | 3.23 | 17.9 | 0.00 | 20.8 | 20.3 | 20.1 | 20.8 | 3406 | 0.27 | 3.70 |
| | 6 | 3.50 | 16.2 | 0.00 | 18.9 | 18.4 | 18.2 | 18.7 | 3662 | 0.30 | 4.45 |
| 3 | no-load | 1.34 | 14.5 | 0.00 | 19.4 | 19.3 | 19.5 | 19.4 | 1807 | 0.07 | 0.00 |
| | 1 | 1.57 | 15.3 | 0.00 | 20.0 | 20.0 | 20.3 | 20.0 | 2030 | 0.10 | 0.82 |
| | 2 | 2.35 | 16.1 | 0.00 | 20.0 | 19.5 | 19.5 | 20.1 | 2682 | 0.14 | 1.64 |
| | 3 | 2.64 | 16.8 | 0.00 | 20.2 | 19.7 | 19.7 | 20.3 | 2930 | 0.17 | 2.39 |
| | 4 | 2.97 | 18.0 | 0.00 | 21.0 | 20.4 | 20.4 | 21.1 | 3199 | 0.21 | 3.18 |
| | 5 | 3.22 | 18.7 | 0.00 | 21.5 | 21.0 | 20.9 | 21.5 | 3420 | 0.24 | 3.88 |
| | 6 | 3.48 | 19.4 | 0.00 | 22.0 | 21.6 | 21.4 | 21.8 | 3632 | 0.28 | 4.55 |

flow rate is calculated from the measured volumetric flow rate and the air density at standard conditions.

Using Equation (3.6), the air density at standard conditions is given by

$$\begin{aligned}\rho_{stand.conds} &= \frac{P_{stand.conds}}{RT_{stand.conds}} \\ &= \frac{101325}{287 \times (0 + 273.15)} \\ &= 1.293 \text{ kg/m}^3\end{aligned}$$

Then using Equation (3.5), the mass flow rate through the turbine is given by

$$\begin{aligned}\dot{m} &= \dot{V}\rho_{stand.conds} \\ &= \frac{3662}{60000} \times 1.293 \\ &= 0.079 \text{ kg/s}\end{aligned}$$

The stagnation temperature at the turbine inlet is calculated from the measured and corrected turbine inlet temperature – corrected using the configured

data logger – and the air velocity at the turbine inlet. In order to determine the air velocity at the turbine inlet, the air density at the corrected turbine inlet temperature and absolute pressure conditions is first determined. The absolute pressure at the turbine inlet is calculated from the measured atmospheric pressure and the measured and corrected turbine inlet pressure – the latter corrected using Equation (A.1)

$$\begin{aligned} P_{1,corr} &= 0.9999P_1 + 0.0245 \\ &= 0.9999 \times 3.50 + 0.0245 \\ &= 352415 \text{ Pa} \end{aligned}$$

The absolute turbine inlet pressure is then calculated using Equation (3.1)

$$\begin{aligned} P_{1,abs} &= P_{1,corr} + P_{atm} \\ &= 352415 + 100410 \\ &= 452825 \text{ Pa} \end{aligned}$$

Then using Equation (3.7), the air density at the turbine inlet is then given by

$$\begin{aligned} \rho_1 &= \frac{P_{1,abs}}{RT_1} \\ &= \frac{452825}{287 \times (16.2 + 273.15)} \\ &= 5.453 \text{ kg/m}^3 \end{aligned}$$

The air velocity at the turbine inlet is then calculated using Equation (3.4)

$$\begin{aligned} V_1 &= \frac{\dot{m}}{\rho_1 \pi {d_1}^2/4} \\ &= \frac{0.079 \times 4}{5.453 \times \frac{22}{7} \times \left(\frac{11}{1000}\right)^2} \\ &= 152 \text{ m/s} \end{aligned}$$

The stagnation temperature at the turbine inlet is then calculated using Equation (3.3)

$$\begin{aligned} T_{01} &= T_1 + \frac{{V_1}^2}{2c_p} \\ &= (16.2 + 273.15) + \frac{152^2}{2 \times 1007} \\ &= 300.82 \text{ K} \end{aligned}$$

From the determined turbine inlet stagnation temperature, the stagnation pressure at the turbine inlet can then be calculated using Equation (3.2)

$$\begin{aligned} P_{01} &= P_{1,abs}\left(\frac{T_{01}}{T_1}\right)^{\gamma_{air}/(\gamma_{air}-1)} \\ &= 452825 \times \left(\frac{300.82}{16.2+273.15}\right)^{1.4/(1.4-1)} \\ &= 518826 \text{ Pa} \end{aligned}$$

The non-dimensional mass flow rate, for the turbine working with air $\theta_{air}$, can now be calculated using Equation (2.7)

$$\begin{aligned} \theta_{air} &= \frac{\dot{m}\sqrt{(RT_{01}/\gamma_{air})}}{P_{01}\pi d_2^2/4} \\ &= \frac{0.079 \times 4\sqrt{287 \times 300.82/1.4}}{518826 \times \frac{22}{7} \times \left(\frac{48.86}{1000}\right)^2} \\ &= 0.0202 \end{aligned}$$

The pressure ratio, for the turbine working with air $P_{R,air}$, is calculated from the turbine inlet stagnation pressure and the absolute turbine exit pressure. In order to determine the absolute turbine exit pressure, the measured turbine exit pressure is first corrected, using Equation (A.2)

$$\begin{aligned} P_{3,corr} &= 1.0000P_3 + 0.0170 \\ &= 1.0000 \times 0.00 + 0.0170 \\ &= 1700 \text{ Pa} \end{aligned}$$

and similar to the absolute turbine inlet pressure, the absolute turbine exit pressure is then calculated using Equation (3.1)

$$\begin{aligned} P_{3,abs} &= P_{3,corr} + P_{atm} \\ &= 1700 + 100410 \\ &= 102110 \text{ Pa} \end{aligned}$$

Using Equation (2.5), the pressure ratio for the turbine working with air can now be determined

$$\begin{aligned} P_{R,air} &= \frac{P_{01}}{P_{3,abs}} \\ &= \frac{518826}{102110} \\ &= 5.1 \end{aligned}$$

The total to static efficiency, for the turbine working with air is calculated from the stage stagnation temperature ratio and the determined turbine pressure ratio. For the stage stagnation temperature ratio, the turbine exit stagnation temperature is calculated from the measured and corrected turbine exit temperature and the air velocity at the turbine exit. In order to determine the air velocity at the turbine exit, the air density at the corrected turbine exit temperature and absolute pressure is first calculated, using Equation (3.10)

$$\begin{aligned}\rho_3 &= \frac{P_{3,abs}}{RT_3} \\ &= \frac{102110}{287 \times (18.6 + 273.15)} \\ &= 1.219 \text{ kg/m}^3\end{aligned}$$

The air velocity at the turbine exit is the calculated from the determined air density at the turbine exit, using Equation (3.9)

$$\begin{aligned}V_3 &= \frac{\dot{m}}{\rho_3 \pi {d_3}^2/4} \\ &= \frac{0.079 \times 4}{1.219 \times \frac{22}{7} \times \left(\frac{35.8}{1000}\right)^2} \\ &= 64 \text{ m/s}\end{aligned}$$

The turbine exit stagnation temperature is then calculated using Equation (3.8)

$$\begin{aligned}T_{03} &= T_3 + \frac{{V_3}^2}{2c_p} \\ &= (18.6 + 273.15) + \frac{64^2}{2 \times 1007} \\ &= 293.78 \text{ K}\end{aligned}$$

The total to static efficiency for the turbine working with air can now be determined using Equation (2.6)

$$\begin{aligned}\eta_{t-s,air} &= \frac{1 - (T_{03}/T_{01})}{1 - (1/P_{R,air})^{(\gamma_{air}-1)/\gamma_{air}}} \\ &= \frac{1 - (293.78/300.82)}{1 - (1/5.1)^{(1.4-1)/1.4}} \\ &= 0.063 \\ &= 6.3\%\end{aligned}$$

The shaft power developed by the turbine $\dot{W}_{shaft}$ is calculated from the turbine shaft angular rotation speed and the torque exerted by the turbine shaft onto the coupled generator shaft. The turbine shaft angular rotation speed is calculated from the measured turbine shaft rotation speed using Equation (3.12)

$$\begin{aligned}\omega &= \frac{2\pi(N)}{60} \\ &= \frac{2 \times \frac{22}{7} \times 5600}{60} \\ &= 586 \text{ rad/s}\end{aligned}$$

On the other hand, the torque exerted by the turbine shaft onto the coupled generator shaft is calculated from the weight exerted by the torque arm onto the spring loaded scale and the torque arm length. The exerted weight is calculated from the measured spring loaded scale displacement using Equation (A.3)

$$\begin{aligned}Weight &= 4.3683x - 0.043 \\ &= 4.3683 \times 0.30 - 0.043 \\ &= 1.27 \text{ N}\end{aligned}$$

From the determined weight exerted by the torque arm, the torque exerted by the turbine shaft is then calculated using Equation (3.13)

$$\begin{aligned}T &= Weight \times l \\ &= 1.27 \times \frac{171.7}{1000} \\ &= 0.22 \text{ N·m}\end{aligned}$$

From the determined torque and angular rotation speed, the turbine shaft power output can now be determined using Equation (3.11)

$$\begin{aligned}\dot{W}_{shaft} &= \omega T \\ &= 586 \times 0.22 \\ &= 128.9 \text{ W}\end{aligned}$$

For indicative purposes, the power dissipated in the electric load is also calculated, using Equation (3.16)

$$\begin{aligned}P_{elec} &= IE_g \\ &= 4.45 \times 24 \\ &= 106.8 \text{ W}\end{aligned}$$

As expected, the power dissipated in the electric load is less than the mechanical work developed by the turbine, owing to the efficiency/inefficiency level of the coupled generator.

For the turbine scaling for refrigerant-123 application, the predicted non-dimensional mass flow rate, for the turbine working with refrigerant-123 is calculated from the determined non-dimensional mass flow rate, for the turbine working with air, using Equation (4.5)

$$\begin{aligned}\theta_{R123} &= \theta_{air}\frac{\left(\frac{2}{\gamma_{R123}+1}\right)^{\frac{1+\gamma_{R123}}{2(\gamma_{R123}-1)}}}{\left(\frac{2}{\gamma_{air}+1}\right)^{\frac{1+\gamma_{air}}{2(\gamma_{air}-1)}}}\\ &= 0.0202 \times \frac{\left(\frac{2}{1.12+1}\right)^{\frac{1+1.12}{2(1.12-1)}}}{\left(\frac{2}{1.4+1}\right)^{\frac{1+1.4}{2(1.4-1)}}}\\ &= 0.0209\end{aligned}$$

while the predicted total to static efficiency, for the turbine working with refrigerant-123 is calculated from the determined total to static efficiency for the turbine working with air, using Equation (4.6)

$$\begin{aligned}\eta_{t-s,R123} &= \eta_{t-s,air}\left[\frac{1}{\eta_{t-s,air}} + \left(\frac{\gamma_{R123}}{\gamma_{air}}\right)^{0.8}\left(1-\frac{1}{\eta_{t-s,air}}\right)\right]\\ &= 6.3\left[\frac{1}{6.3} + \left(\frac{1.12}{1.4}\right)^{0.8}\left(1-\frac{1}{6.3}\right)\right]\\ &= 5.4\%\end{aligned}$$

The predicted pressure ratio, for the turbine working with refrigerant-123, is calculated from the determined pressure ratio for the turbine working with air, using Equation (4.7)

$$\begin{aligned}P_{R,R123} &= \left[1+\frac{\eta_{t-s,R123}}{\eta_{t-s,air}}\left(\frac{\gamma_{R123}-1}{\gamma_{air}-1}\right)\left(P_{R,air}^{\frac{\gamma_{air}-1}{\gamma_{air}}}-1\right)\right]^{\frac{\gamma_{R123}}{\gamma_{R123}-1}}\\ &= \left[1+\frac{5.4}{6.3}\left(\frac{1.12}{1.4}\right)\left(5.1^{\frac{1.4-1}{1.4}}-1\right)\right]^{\frac{1.12}{1.12-1}}\\ &= 3.8\end{aligned}$$

**Analysis**:

The turbine performance characteristics determined from the sample calculation, for the turbine working with both air and refrigerant-123, can be seen to closely match those calculated and tabulated for the second test run of the designed turbine rotor, at test point 6 (see Table B.4).

## B.3 Calculated turbine performance characteristics

The calculated turbine performance characteristics, for both the ITmini rotor and the designed rotor, are shown in Tables B.3 and B.4, with the latter as well showing the predicted turbine performance characteristics for the turbine working with refrigerant-123.

**Table B.3:** Calculated turbine performance characteristics for the ITmini rotor

| Test run | Test point | $P_{R,air}$ | $\theta_{air}$ | $\eta_{t-s,air}$ [%] | $\dot{W}_{shaft}$ [W] |
|---|---|---|---|---|---|
| 1 | no-load | 2.5 | 0.0189 | 8.0 | 44.1 |
| | 1 | 2.7 | 0.0190 | 7.5 | 57.3 |
| | 2 | 3.0 | 0.0190 | 6.7 | 70.5 |
| | 3 | 3.4 | 0.0190 | 6.3 | 83.7 |
| | 4 | 4.5 | 0.0192 | 6.2 | 96.8 |
| | 5 | 5.1 | 0.0194 | 6.2 | 110.1 |
| | 6 | 5.4 | 0.0196 | 6.2 | 123.2 |
| 2 | no-load | 2.4 | 0.0189 | 9.7 | 26.5 |
| | 1 | 2.6 | 0.0189 | 7.8 | 39.7 |
| | 2 | 2.9 | 0.0189 | 7.0 | 57.2 |
| | 3 | 3.4 | 0.0190 | 6.5 | 74.8 |
| | 4 | 4.6 | 0.0193 | 6.5 | 88.1 |
| | 5 | 5.0 | 0.0194 | 6.3 | 101.2 |
| | 6 | 5.4 | 0.0194 | 6.0 | 114.4 |
| 3 | no-load | 2.5 | 0.0189 | 7.8 | 44.1 |
| | 1 | 2.6 | 0.0191 | 7.8 | 57.2 |
| | 2 | 3.0 | 0.0190 | 7.0 | 74.8 |
| | 3 | 3.3 | 0.0191 | 6.8 | 92.5 |
| | 4 | 4.5 | 0.0193 | 6.4 | 105.6 |
| | 5 | 5.0 | 0.0194 | 6.4 | 118.8 |
| | 6 | 5.4 | 0.0194 | 6.0 | 132.0 |

**Table B.4:** Calculated turbine performance characteristics for the designed rotor

| Test run | Test point | $P_{R,air}$ | $P_{R,R123}$ | $\theta_{air}$ | $\theta_{R123}$ | $\eta_{t-s,air}$ [%] | $\eta_{t-s,R123}$ [%] | $\dot{W}_{shaft}$ [W] |
|---|---|---|---|---|---|---|---|---|
| 1 | no-load | 3.0 | 2.4 | 0.0197 | 0.0203 | 6.9 | 5.9 | 39.7 |
| | 1 | 3.3 | 2.5 | 0.0197 | 0.0204 | 6.8 | 5.8 | 52.8 |
| | 2 | 4.0 | 3.0 | 0.0199 | 0.0205 | 6.6 | 5.7 | 66.1 |
| | 3 | 4.3 | 3.2 | 0.0199 | 0.0205 | 6.5 | 5.6 | 79.2 |
| | 4 | 4.6 | 3.4 | 0.0199 | 0.0206 | 6.5 | 5.6 | 92.4 |
| | 5 | 4.9 | 3.6 | 0.0200 | 0.0207 | 6.4 | 5.6 | 105.6 |
| | 6 | 5.1 | 3.8 | 0.0201 | 0.0207 | 6.4 | 5.6 | 118.8 |
| 2 | no-load | 2.7 | 2.2 | 0.0196 | 0.0202 | 6.7 | 5.8 | 39.7 |
| | 1 | 3.0 | 2.3 | 0.0196 | 0.0203 | 6.6 | 5.7 | 52.8 |
| | 2 | 3.8 | 2.9 | 0.0198 | 0.0204 | 6.6 | 5.7 | 70.4 |
| | 3 | 4.1 | 3.1 | 0.0198 | 0.0205 | 6.6 | 5.7 | 88.1 |
| | 4 | 4.5 | 3.3 | 0.0200 | 0.0206 | 6.5 | 5.6 | 101.2 |
| | 5 | 4.8 | 3.6 | 0.0200 | 0.0207 | 6.4 | 5.5 | 114.4 |
| | 6 | 5.1 | 3.8 | 0.0201 | 0.0208 | 6.4 | 5.5 | 127.6 |
| 3 | no-load | 2.6 | 2.1 | 0.0192 | 0.0198 | 6.6 | 5.7 | 26.5 |
| | 1 | 2.9 | 2.3 | 0.0196 | 0.0202 | 6.7 | 5.8 | 39.7 |
| | 2 | 3.8 | 2.9 | 0.0198 | 0.0205 | 6.6 | 5.7 | 57.2 |
| | 3 | 4.1 | 3.1 | 0.0200 | 0.0206 | 6.8 | 5.8 | 70.4 |
| | 4 | 4.5 | 3.3 | 0.0200 | 0.0207 | 6.7 | 5.8 | 88.0 |
| | 5 | 4.8 | 3.5 | 0.0201 | 0.0208 | 6.6 | 5.7 | 101.2 |
| | 6 | 5.1 | 3.8 | 0.0202 | 0.0208 | 6.5 | 5.6 | 118.8 |

# Appendix C

# Rotor Design Code

A rotor design code, as described in Subsection 3.3.2, and based on the rotor design procedure described in Subsection 3.3.1 and following a radial inflow turbine rotor design code outlined by Whitfield and Baines (1990), was written in MATLAB R2010a. The MATLAB compiled design code follows, with its main output being the design point performance and rotor geometry parameters given in Table 3.1.

```
1  function Turbinegeom
2  %This code optimizes the turbine rotor geometry, based on
       maximum attainable turbine total to static efficiency.
3  clear all
4  clc
5  %initialise and set preassigned design parameters
6  GAMMA=1.4;       %specific heat ratio
7  EFFN=0.9;        %stator efficiency
8  EFFS=0.85;       %initial stage total to static efficiency
9  L2R2=0.88;       %axial length to inlet radius ratio
10 R3HR3S=0.4;      %rotor exit hub to shroud radius ratio
11 W3SW2=2;         %relative velocity ratio across rotor
12 B2R2=0.84;       %non dimensionalized blade height at inlet
13 R3SR2=1;         %rotor exit shroud to inlet blade radius
       ratio
14 TB2=0.045;       %rotor shroud clearance to blade height
       ratio
15 Sw=0.005;        %stage power ratio
16 epsilon=0.01;    %convergence criterion
17
18 for ZB=7:1:10;  %number of blades
19          ALPHA2=acosd((0.63*pi/(2*ZB))^0.5); %inlet
               absolute flow angle
20          BETA2=-acosd(1-0.63*pi/ZB);   %inlet relative flow
                angle. NB negative angle.
```

```
21          P01P3=(1/(1-Sw/EFFS))^(GAMMA/(GAMMA-1));    %Stage
                total to static pressure ratio
22          T03T01=1-Sw;    %Stage total to total temperature
               ratio
23 %Determine minimum Mach number
24          M2=((Sw/(GAMMA-1))*(2*cosd(BETA2))/(1+cosd(BETA2))
               )^0.5;    %minimum possible rotor inlet Mach
               number
25          M02=((M2^2)/(1-(((GAMMA-1)/2)*M2^2)))^0.5;  %rotor
                inlet Mach number at inlet stagnation
               conditions
26 %Calculate inlet conditions
27          V2C01=M02;  %non-dimensionalized inlet absolute
               flow velocity
28          T02T2=1+(((GAMMA-1)/2)*(M2^2)); % inlet total to
               static temperature ratio
29          P02P2=(T02T2)^(GAMMA/(GAMMA-1));    %inlet total
               to static pressure ratio
30          T2T01=1/(T02T2);    % static blade inlet to total
               stator temperature ratio. NB T02=T01
31          R2R02=(T2T01)^(1/(GAMMA-1)); %density ratio at
               blade inlet
32          P2P01=(1-(1-T2T01)/EFFN)^(GAMMA/(GAMMA-1)); %
               static blade inlet to total stator pressure
               ratio
33          P02P3=P02P2*P2P01*P01P3; %total to static pressure
                ratio across blade row
34          P02P01=P02P3*1/P01P3;   %total to static pressure
               ratio across stator and blade inlet
35          R02R01=P02P01;  %total to total density ratio
               across stator and blade inlet
36          R2R01=R2R02*R02R01; %static to total density ratio
                across blade inlet and stator
37          U2VT2=Sw/(GAMMA-1); %incidence factor
38          VT2C01=V2C01*sind(ALPHA2);  %non dimensionalized
               inlet absolute tangetial flow velocity
39          VM2C01=V2C01*cosd(ALPHA2);  %non dimensionalized
               inlet absolute meriodional flow velocity
40          W2C01=VM2C01/cosd(BETA2);   % non dimensionalized
               inlet relative flow velocity
41          M2D=W2C01*T02T2^0.5;    %inlet relative flow Mach
               number
42          U2C01=U2VT2/VT2C01; %non dimensionalized rotor tip
                speed
43 % determine optimum exit relative flow angle and exit
      conditions
```

```
44          for BETA3=-55:-0.1:-75;    %exit relative flow
               angle. NB negative angle
45                W3C03=W3SW2*W2C01/T03T01^0.5;  %non
                     dimensionlized exit relative flow
                     velocity
46                V3C03=W3C03*cosd(BETA3);    %non
                     dimensionalized exit absolute flow
                     velocity
47                T3T03=1-(((GAMMA-1)/2)*V3C03^2);    %
                     static to total blade exit temperature
                     ratio
48                T03T3=1/T3T03;  %total to static blade
                     exit temperature ratio
49                M3=V3C03*T03T3^0.5; %absolute flow exit
                     Mach number
50                V3C01=V3C03*T03T01; %modified non
                     dimensionalized exit absolute flow
                     velocity
51                V3U2=V3C01*U2C01;   %dicharge velocity
                     ratio
52                W3C01=W3C03*T03T01^0.5; %modified non
                     dimensionalized exit relative flow
                     velocity
53                M3D=W3C03*(1/T3T03)^0.5;    %exit relative
                      flow Mach number
54                DRT=(T2T01-T3T03*(1-Sw))/Sw;    %degree of
                      reaction
55                U3C03=-V3C03*tand(BETA3);    %non
                     dimensionalized rotor exit speed
56                U3C01=U3C03*T03T01^0.5; %modified non
                     dimensionalised rotor exit speed
57                R3RMSR2=R3SR2*((1+R3HR3S^2)/2)^0.5; %RMS
                     radius ratio
58                WT3C03=U3C03;   %non dimensionalized exit
                     relative tangetial flow velocity
59                W3W2=W3C01/W2C01;% relative velocity ratio
                      across blade row
60                R3R03=T3T03^(1/(GAMMA-1));  %exit static
                     to total density ratio
61                P03P3=(1/T3T03)^(GAMMA/(GAMMA-1));  %exit
                     pressure ratio
62                P03P01=P03P3/P01P3; %stage total to total
                     pressure ratio
63                R03R01=P03P01/T03T01;   %stage total to
                     total density ratio
```

```
64                  R02R03=R02R01/R03R01;   %rotor row total
                       to total density ratio
65                  R3R01=R3R03*R03R01; %stage static to total
                        density ratio
66                  THETA2=cosd(ALPHA2)*M2*(1+((GAMMA-1)/2)*M2
                       ^2)^-((GAMMA+1)/(2*(GAMMA-1)));   %non
                       dimensionalized inlet mass flow rate
67                  THETA3=M3*(1+((GAMMA-1)/2)*M3^2)^-((GAMMA
                       +1)/(2*(GAMMA-1)));    %non
                       dimensionalized exit mass flow rate
68                  A3A2=(THETA2/THETA3)*R02R03*T03T01^0.5; %
                       area ratio across the rotor
69                  THETA=THETA2*P02P01*B2R2;   %non
                       dimensional mass flow parameter
70  %non dimensional performance parameters
71                  NDTOR=THETA*VT2C01; %non dimensional
                       torque
72                  U2V0=(((GAMMA-1)/2)*(U2C01^2)/(1-P03P01^((
                       GAMMA-1)/GAMMA)))^0.5;    %isentropic
                       velocity ratio on total to total basis
73                  U2V0R=(((GAMMA-1)/2)*(U2C01^2)/(1-(1/P01P3
                       )^((GAMMA-1)/GAMMA)))^0.5;    %
                       isentropic velocity ratio on total to
                       static basis
74                  EFFR=(1-T03T01)/(1-(1/P02P3)^((GAMMA-1)/
                       GAMMA));    %rotor total to static
                       efficiency
75                  NSS=((2^1.5)*(U2V0R^3)*V3C01*(R3SR2^2)*pi
                       *(1-R3HR3S^2)/U2C01)^0.5;  %specific
                       speed on total to static basis
76                  NST=((2^1.5)*(U2V0^3)*V3C01*(R3SR2^2)*pi
                       *(1-R3HR3S^2)/U2C01)^0.5;   %specific
                       speed on total to total basis
77  %Calculate rotor losses
78                  HDHL=8*(B2R2/((ZB*B2R2+2*pi)*(1-R3RMSR2+
                       L2R2-0.5*B2R2)))+4*R3SR2*(1-R3HR3S^2)
                       /((ZB*(1-R3HR3S)+pi*(1+R3HR3S))*(1-
                       R3RMSR2+L2R2-0.5*B2R2));  % hydraulic
                       diameter to length ratio
79                  DQF=0.03*(W2C01^2+W3C01^2)/(4*HDHL*U2C01
                       ^2); %friction loss with friction
                       factor 4Cf set at 0.03
80                  KR=(B2R2+R3RMSR2*(1-R3HR3S))/(1-R3RMSR2);
81                  DQFK=KR*(W2C01^2+W3C01^2)/U2C01^2; %
                       Rodgers passage curvature loss
```

```
82                  DQBL=2*(VT2C01/U2C01)^2/(ZB*L2R2); %blade
                        loading loss
83                  DQCL=0.4*TB2*(VT2C01/U2C01)^2;  %clearance
                         loss
84                  DQEX=0.5*(V3C01/U2C01)^2;   %exit loss
85                  DQ=DQF+DQFK+DQBL+DQCL+DQEX; %total loss
86                  DQTH=VT2C01/U2C01;  %actual non
                        dimensional enthalpy change
87                  EFFRC=DQTH/(DQTH+DQ);   %calculated rotor
                        efficiency
88              if abs((EFFS-EFFRC))<=epsilon && U2V0<=0.707
                      %convergence criteria
89
90                  disp('INLET CONDITIONS')
91
92  fprintf('relative inlet flow angle:\t%.0f deg\n',BETA2)
93  fprintf('absolute inlet flow angle:\t%.0f deg\n',ALPHA2)
94  fprintf('absolute inlet Mach number:\t%.1f\n',M2)
95  fprintf('relative inlet Mach number:\t%.1f\n',M2D)
96  fprintf('non dimensional inlet absolute flow velocity:\t
      %.1f\n',V2C01)
97  fprintf('non dimensional inlet relative flow velocity:\t
      %.1f\n',W2C01)
98  fprintf('non dimensional rotor tip speed:\t%.1f\n',U2C01)
99  fprintf('non dimensional inlet absolute flow tangetial
      velocity:\t%.1f\n',VT2C01)
100 fprintf('non dimensional inlet absolute flow meridional
      velocity:\t%.1f\n',VM2C01)
101
102                 disp('OUTLET CONDITIONS')
103
104 fprintf('relative exit flow angle:\t%.0f deg\n',BETA3)
105 fprintf('absolute exit Mach number:\t%.1f\n',M3)
106 fprintf('relative exit Mach number:\t%.1f\n',M3D)
107 fprintf('non dimensional exit absolute flow velocity:\t%.1
      f\n',V3C01)
108 fprintf('non dimensional exit relative flow velocity:\t%.1
      f\n',W3C01)
109 fprintf('non dimensional rotor exit speed:\t%.1f\n',U3C01)
110 fprintf('calculated rotor efficiency:\t%.3f\n',EFFRC)
111 fprintf('total to static rotor efficiency:\t%.3f\n',EFFS)
112 fprintf('radius ratio across blade:\t%.1f\n',R3SR2)
113 fprintf('area ratio across blade:\t%.1f\n',A3A2)
114 fprintf('inlet blade height radius ratio:\t%.2f\n',B2R2)
115 fprintf('stage total to static pressure ratio:\t%.1f\n',
      P01P3)
```

```
116 fprintf('blade speed velocity ratio:\t%.3f\n',U2V0)
117 fprintf('ZB:\t%.0f\n',ZB)
118 fprintf('EFFR:\t%.3f\n',EFFR)
119
120             break
121             else
122                 EFFS=Sw/(1-(1-Sw/EFFRC)*P02P01^((GAMMA-1)/
                        GAMMA));  %update stage total to static
                         efficiency
123             end
124
125         end
126
127
128 end
129
130 end
```

# Appendix D

# CAD Drawings

Figure D.1 shows the designed turbine rotor manufacturing CAD drawing, while Figure D.2 shows the ITmini waste heat turbine experimental kit assembly CAD drawing.

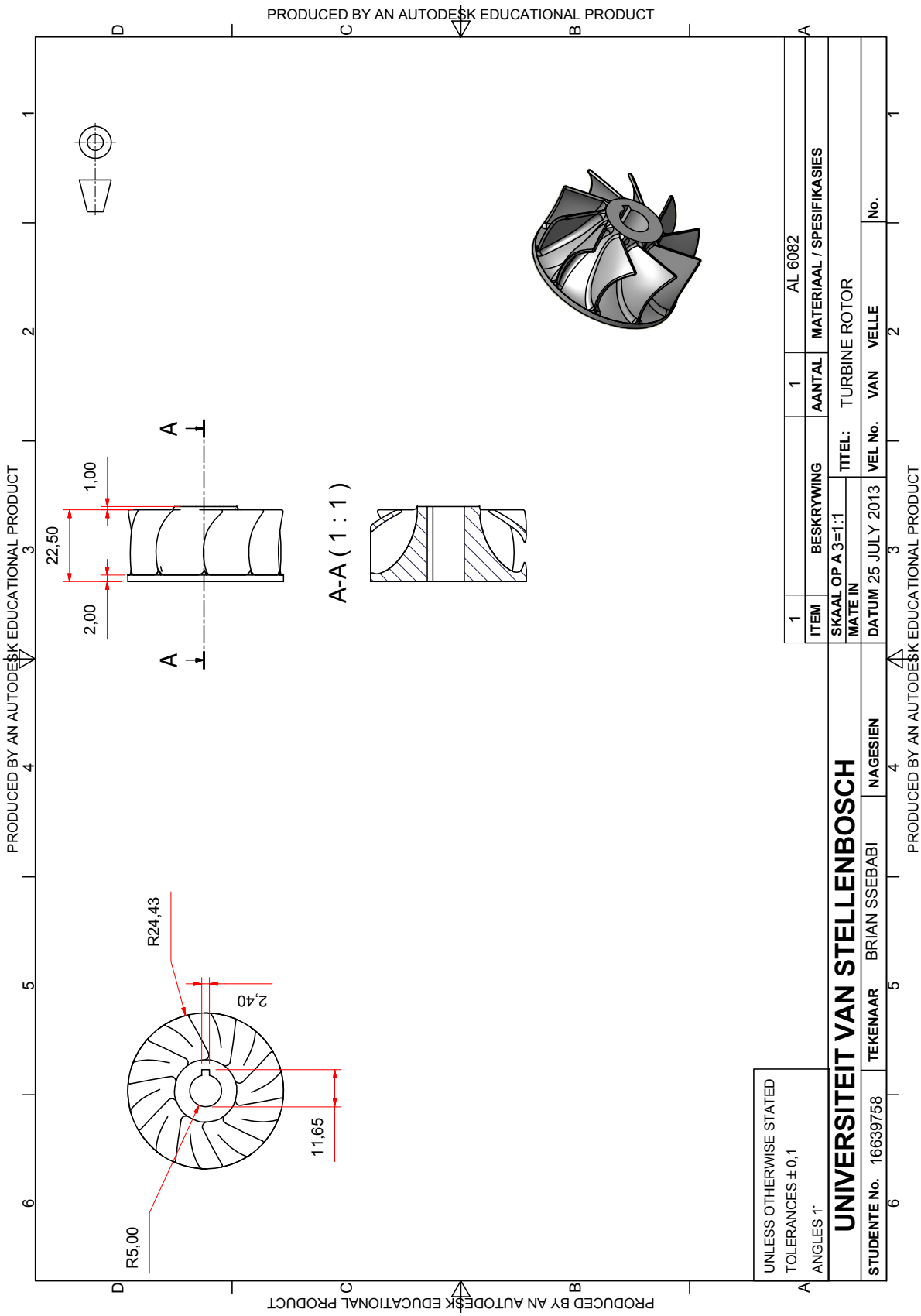


**Figure D.1:** Designed turbine rotor manufacturing CAD drawing

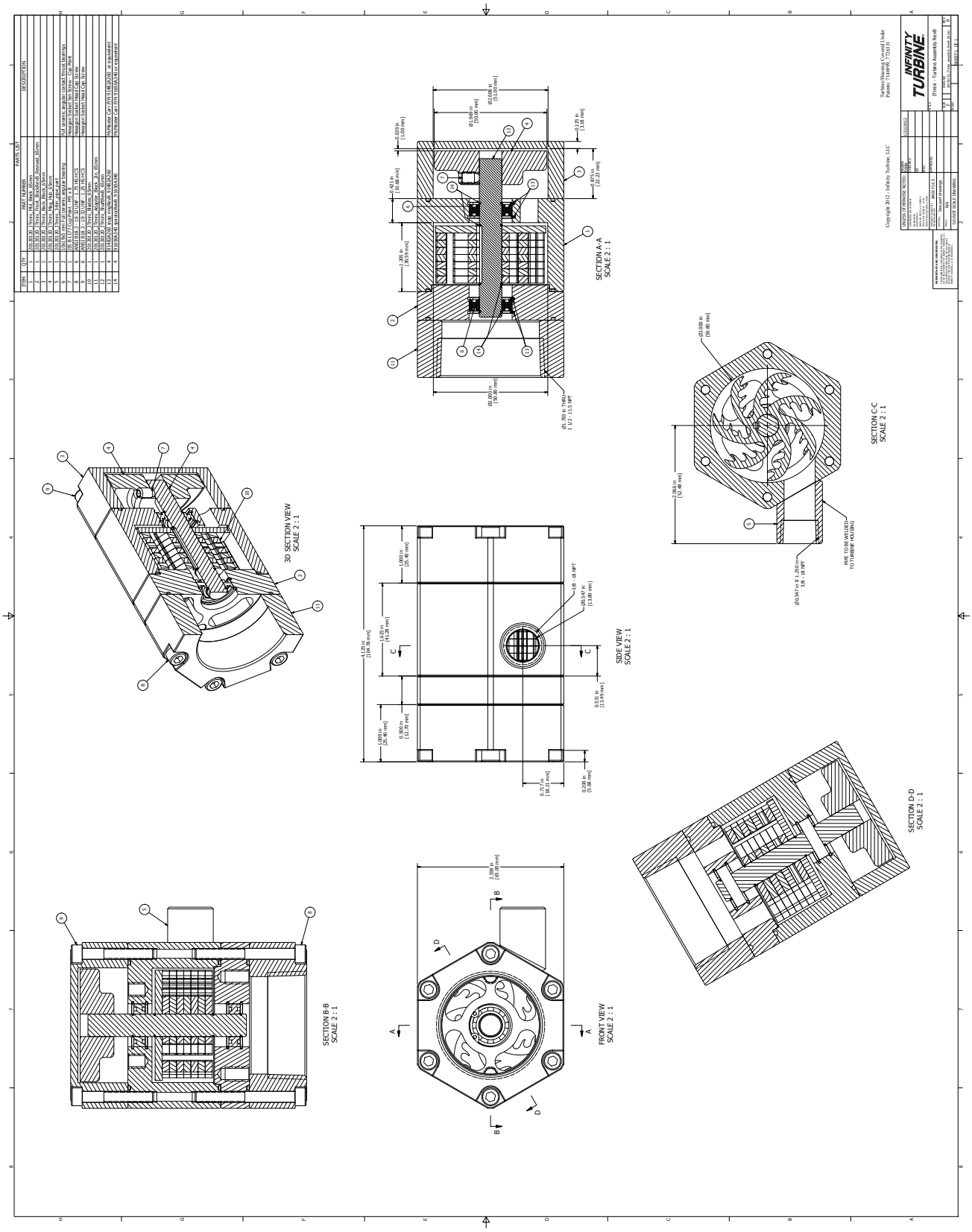


**Figure D.2:** ITmini experimental turbine kit assembly plans (Infinity Turbine LLC, 2012)

# List of References

Agilent technologies, Inc. (2006). *Agilent 34970A Data Acquisition/Switch unit*. Agilent technologies, Inc., 815 14th Street S.W., Loveland, Colorado 80537, U.S.A., 4th edn.

American Society of Heating, Refrigeration and Air-conditioning Engineers, Inc. (2009). *2009 ASHRAE Handbook – Fundamentals (SI Edition)*, chap. Thermodynamics and Refrigeration Cycles, pp. 2.1–2.20.

ASME PTC 10 (1997). Compressors and exhausters.

Aungier, R.H. (2006). *Turbine Aerodynamics. Axial-Flow and Radial-Inflow Turbine Design and Analysis*. 1st edn. ASME, New York, NY 10016, USA. ISBN 0-7918-0241-8.

b. Mohd. Tahir, M., Yamada, N. and Hoshino, T. (2010). Efficiency of compact organic rankine cycle system with rotary-vane-type expander for low-temperature waste heat recovery. *International Journal of Civil and Environmental Engineering*, vol. 2, pp. 11–16.

Balje, O.E. (1981). *Turbomachines: A Guide to Design, Selection and Theory*. John Wiley & Sons Inc., New York.

Beckwith, T.G., Marangoni, R.D. and Lienhard V, J.H. (1993). *Mechanical Measurements*. 5th edn. Addison-Wesley. ISBN 0-201-56947-7.

Brun, K. and Nored, G.M. (2006). Guideline for Field Testing of Gas Turbine and Centrifugal Compressor Performance. Tech. Rep., Gas Machinery Research Council.

Cengel, Y.A. and Cimbala, J.M. (2010). *Fluid Mechanics. Fundamentals and applications*. 2nd edn. McGraw-Hill, New York, NY 10020, USA. ISBN 978-007-128421-9.

Daugherty, R.L., Franzini, J.B. and Finnemore, E.J. (1985). *Fluid Mechanics with Engineering Applications*. Eighth edn. McGraw-Hill, Singapore. ISBN 0-07-Y66267-3.

Dennis, B. (2013). Aluminium turbine blades for freon (refrigerant-123). Letter. Technical consultant to the Aluminium Federation of South Africa.

Department of Mechanical and Mechatronic Engineering, Stellenbosch University (2012). Safety procedures for laboratory set ups.

Dixon, S.L. (1998). *Fluid Mechanics and Thermodynamics of Turbomachinery*. 4th edn. Butterworth-Heinemann, Oxford OX2 8DP, England. ISBN 0 7506 7059 2.

Electricity Pricing Policy (EPP) of the South African Electricity Supply Industry (2008). Government Notice 31741, Department of Minerals and Energy, Republic of South Africa.

Energy Efficiency and Demand Side Management Program Evaluation (2011). Tech. Rep., Eskom.

Erickson, D., Anand, G. and Kyung, I. (2004). Heat activated dual-function absorption cycle. *ASHRAE Transactions*, vol. 110, pp. 515–524.

Erickson, D., Papar, R., Anand, G. and Tang, J. (1998). Refinery waste heat powered absorption refrigeration – cycle specification and design. *Proceedings of ASME*, vol. 38, pp. 391–402.

Festo (2012*a*). *Festo SDE3 Pressure/vacuum sensor*. Festo AG & Co. KG, Postfach, D-73726 Esslingen, Germany.

Festo (2012*b*). *Festo SFAM Flow sensor*. Festo AG & Co. KG, Postfach, D-73726 Esslingen, Germany.

Forrest, A.R. (1972). Interactive interpolation and approximation by Bezier polynomials. *Computer Journal*, vol. 15, pp. 71–79.

Giese, G. (2012). Infinity Turbine LLC Price list. email. greg@infinityturbine.com.

Goswami, D.Y. and Xu, F. (1999). Analysis of a new thermodynamic cycle for combined power and cooling using low and mid temperature solar collectors. *Solar Energy Engineering, ASME*, vol. 121, pp. 91–97.

Hettiarachchi, H., Golubovic, M. and Worek, W.M. (2007). Optimum design criteria for an organic rankine cycle using low-temperature geothermal heat sources. *Energy*, vol. 32, pp. 1698–1706.

Hiett, G.F. and Johnson, I.H. (1963). Experiments concerning the aerodynamic performance of inward radial flow turbines. In: *Proceedings of the Institution of Mechanical Engineers*, pp. 28–42.

Infinity Turbine LLC (2012). ITmini – Turbine Assembly RevB. Available at: `ftp://24.207.25.40/`, [2012, August 24].

IRP 2010 (2011). Integrated resource plan for electricity 2010 – 2030. Final report, Department of Energy, Republic of South Africa.

Iso-tech (2012). *Instruction Manual IDM 103N/105N/106N Digital Multimeter*. Isotech, Corby, Northamptonshire NN17 9RS, United Kingdom.

Jamieson, A.W.H. (1955). The radial turbine. In: Sir Roxbee-Cox, H. (ed.), *Gas turbine principles and practice*, chap. 9. Newnes, London.

Jeggels, D.H. and Dobson, R. (2011). Theoretical and experimental evaluation of a low temperature lithium-bromide/water absoption system. Second Annual CRSES Student Conference.

Kang, S.H. (2012). Design and experimental study of ORC (organic Rankine cycle) and radial turbine using R245fa working fluid. *Energy*, vol. 41, no. 1, pp. 514–524. ISSN 03605442.

Lemort, V., Guillaume, L., Legros, A., Declaye, S. and Quoilin, S. (2013). A comparison of piston, screw and scroll expanders for small scale rankine cycle systems. Available at: `http://www.orbi.ulg.ac.be/bitstream/2268/147369/1/p259v2.pdf`, [2013, November 13].

Lemort, V., Quoilin, S., Cuevas, C. and Lebrun, J. (2009). Testing and modeling a scroll expander integrated into an organic rankine cycle. *Applied Thermal Engineering*, vol. 29, pp. 3094–3102.

Ng, K., Bong, T. and Lim, T. (1990 January). A thermodynamic model for the analysis of screw expander performance. *Heat Recovery Systems and CHP*, vol. 10, no. 2, pp. 119–133. ISSN 08904332.

Pei, G., Li, J., Li, Y., Wang, D. and Ji, J. (2011). Construction and dynamic test of a small-scale organic rankine cycle. *Energy*, vol. 36, no. 5, pp. 3215–3223. ISSN 03605442.

Pei, G., Li, Y., Li, J. and Ji, J. (2010). An experimental study of a micro high-speed turbine that applied in organic rankine cycle. In: *Power and Energy Engineering Conference (APPEEC)*. Asia-Pacific.

Qiu, G., Liu, H. and Riffat, S. (2011). Expanders for micro-CHP systems with organic Rankine cycle. *Applied Thermal Engineering*, vol. 31, pp. 3301–3307. ISSN 13594311.

Qiu, G., Shao, Y., Li, J., Liu, H. and Riffat, S.B. (2012 June). Experimental investigation of a biomass-fired ORC-based micro-CHP for domestic applications. *Fuel*, vol. 96, pp. 374–382. ISSN 00162361.

Roberts, S.K. (2001). *Effects of fluid properties on the aerodynamic performance of turbomachinery for semi-closed cycle gas turbine engines using* $O_2/CO_2$ *Combustion*. Master's thesis, Carleton University.

Rodgers, C. (1987). Meanline performance prediction for radial inflow turbines. In small high pressure ratio turbines. Tech. Rep., VKI lecture series.

Rodgers, C. and Geiser, R. (1987). Performance of a high efficiency radial/axial turbine. *Trans ASME Journal of Turbomachinery*, vol. 109, pp. 151–154.

Rohlik, H.E. (1968). *Analytical determination of radial inflow turbine design geometry for maximum efficiency*. NASA TN D-4384, Washington D. C.

Rohlik, H.E. (1975). Radial inflow turbines. In: Glassmann, A.J. (ed.), *Turbine design and application*, vol. 3. NASA SP 290.

Saitoh, T., Yamada, N. and Wakashima, S. (2007). Solar rankine cycle system using scroll expander. *Environment and Engineering*, vol. 2, pp. 708–718.

Senda, F.M. (2012). *Aspects of Waste Heat Recovery and Utilisation (WHR&U) in Pebble Bed Modular Reactor (PBMR) Technology*. Master's thesis, Stellenbosch University.

Smith, I.K., Stosic, N. and Kovacevic, A. (2005). Screw expanders increase output and decrease the cost of geothermal binary power plant systems. Available at: `http://www.staff.city.ac.uk/~ra601/grc2005.pdf`, [2013, November 11].

Srikhirin, P., Aphornratana, S. and Chungpaibulpatana, S. (2001). A review of absorption refrigeration technologies. *Renewable & Sustainable Energy Reviews*, vol. 5, pp. 343–372.

Stanitz, J.D. (1952). Some theoretical aerodynamic investigations of impellers in radial and mixed flow centrifugal compressors. *Trans ASME*, vol. 74, pp. 473–497.

van der Merwe, B.B. (2012). *Design of a centrifugal compressor impeller for micro gas turbine application*. Master's thesis, Stellenbosch.

Verstraete, T., Alsalihi, Z. and Van den Braemussche, R.A. (2010). Multidisciplinary Optimization of a Radial Compressor for Microgas Turbine Applications. *Journal of Turbomachinery*, vol. 132, pp. 1–7.

Wang, H., Peterson, R.B. and Herron, T. (2009). Experimental performance of a compliant scroll expander for an organic Rankine cycle. *Proceedings of the Institution of Mechanical Engineers, Part A: Journal of Power and Energy*, vol. 223, pp. 863–872. ISSN 0957-6509.

Waring, R., Hall, J., Pullen, K. and Etemad, R. (1996). An Investigation of Face type Magnetic Couplers. *Journal of Power and Energy*, vol. 210, pp. 263–272.

Waste Heat Recovery: Technology and Opportunities in U.S. Industry (2008). Tech. Rep., U.S. Department of Energy, United States of America.

Whitfield, A. and Baines, N.C. (1990). *Design of Radial Turbomachines*. 1st edn. Longman Scientific & Technical, Essex CM20 2JE, England. ISBN 0-582-49501-6.

Yamamoto, T., Furuhata, T., Arai, N. and Mori, K. (2001). Design and testing of the organic rankine cycle. *Energy*, vol. 26, pp. 239–251.

Yang, B., Peng, X., He, Z., Guo, B. and Xing, Z. (2009). Experimental investigation on the internal working process of a $CO_2$ rotary vane expander. *Applied Thermal Engineering*, vol. 29, pp. 2289 – 2296. ISSN 1359-4311.

Zanelli, R. and Favrat, D. (1994). Experimental investigation of a hermetic scroll expander-generator. In: *Proceedings of the International Compressor Engineering Conference at Purdue*, pp. 459–464.

Zemp, A., Kammerer, A. and Abhari, R.S. (2010). Unsteady computational fluid dynamics investigation on inlet distortion in a centrifugal compressor. *Journal of Turbomachinery*, vol. 132, pp. 031015–1–031015–9.